UNLV Retrospective Theses & Dissertations

A spectroscopic analysis of the starburst galaxies Ngc 3395 and Ngc 3396

Kenneth Plaks
University of Nevada, Las Vegas

Follow this and additional works at: https://digitalscholarship.unlv.edu/rtds

A SPECTROSCOPIC ANALYSIS OF THE

STARBURST GALAXIES NGC 3395

AND NGC 3396

by

Kenneth Plaks

Bachelor of Science
United States Air Force Academy
1989

Master of Science
Massachusetts Institute of Technology
1991

A dissertation submitted in partial fulfillment
of the requirements for the

Doctor of Philosophy in Physics
Department of Physics
College of Sciences

Graduate College
University of Nevada, Las Vegas
May 2003

UMI Number: 3091807

UMI®

UMI Microform 3091807

UNLV
UNIVERSITY OF NEVADA LAS VEGAS

Dissertation Approval
The Graduate College
University of Nevada, Las Vegas

_____ April 3 _____, 20 03

The Dissertation prepared by

Kenneth Plaks

Entitled

A Spectroscopic Analysis of the Starburst Galaxies NGC 3395 and NGC 3396

is approved in partial fulfillment of the requirements for the degree of

Doctor of Philosophy in Physics

_____
Examination Committee Chair

_____
Dean of the Graduate College

_____
Examination Committee Member

_____
Examination Committee Member

_____
Graduate College Faculty Representative

ii

ABSTRACT

A Spectroscopic Analysis of the Starburst
Galaxies NGC 3395 and NGC 3396

by

Kenneth Plaks

Dr. Donna E. Weistrop, Examination Committee Chair
Professor of Physics
University of Nevada, Las Vegas

We have obtained ultraviolet and visible wavelength spectra of 31 bright star

forming knots in the interacting galaxies NGC 3395 and NGC 3396 using the Space

Telescope Imaging Spectrograph (STIS) on the Hubble Space Telescope. The knots are

possible super star clusters on the order of $\sim$ 100 pc diameter with measured metallicities

on the order of 0.5-0.6 $Z_\odot$. The spectra are consistent with a massive production of hot

young stars in a starburst.

Ages of the starburst knots were calculated using several diagnostics from the

Leitherer et al. Starburst 99 code (SB99) using an Initial Mass Function (IMF) with a

power law coefficient α=2.35 and an upper mass limit of 100 $M_\odot$. We modeled our star

forming knots as instantaneous starbursts with the measured metallicity and we obtained

consistent and reasonable estimates of the starburst age. The UV-brightest knots are $\sim$ 5

Myr old in both galaxies. We found no age gradient in the galaxies implying the starburst

does not propagate across the galaxy but rather occurs simultaneously everywhere. The

data are also consistent with the interpretation that the starburst is not only happening

more or less simultaneously within each galaxy, it is also occurring simultaneously in both galaxies. If true, the fact that it is occurring simultaneously in both galaxies gives credence to the interaction being the source of the star formation in line with current theory.

While our starforming knots were spatially resolved, at high redshift one cannot resolve individual knots and instead has to rely on spatially unresolved spectra. To assess the representativeness of these spectra of the underlying structure, we simulated the spectra one would observe by defining the entire portion of each galaxy observed as an unresolved knot. We found the metallicities for the unresolved knots were very representative of the resolved knots that made them up. We also found that the ages we derived for the unresolved knots were representative of the underlying resolved knot ages to approximately a factor of 2-3.

We measured the flux in the broad He II $\lambda4686$ emission line characteristic of Wolf-Rayet (WR) stars. Uncorrected for reddening, we estimated ~250 WR and ~1100 O stars in NGC 3395 and ~400 WR and ~2500 O stars in NGC 3396. We were unable to sub-categorize the WR stars, although the spectra do have some characteristics of WN stars.

We discovered a super bubble in NGC 3395 with a radius of approximately 24 pc containing ~80 WR stars uncorrected for reddening. We calculate that it also contains ~25 O stars although we suspect that we have severely underestimated this value and a more representative value may be as many as 420 O stars uncorrected for reddening.

TABLE OF CONTENTS

LIST OF FIGURES

LIST OF TABLES

ACKNOWLEDGEMENTS

This dissertation has been several years in the making. Over the past 5 years, I have been blessed by the support I've received from friends and family. It is no exaggeration to say that I could not have finished this without all your help.

One person in particular has suffered more than anyone else (including me!) during this process—my wife Kara. When I first asked her, so many years ago, if she would be supportive of me starting this odyssey, she said yes without hesitation. While I don't think she knew what she was getting herself into, she never waivered. Through a wedding, the birth of two children, and the first 5 years of our marriage she has put up with much more than she bargained for. Sweetheart, I cannot thank you enough. I don't know why you did it, but I'm glad you did! I love you.

I would also like to thank my son Hunter, who frequently burst into my "dungeon" and demanded a "big hug," usually when I was right in the middle of some deep thought. Just as it looked as if Hunter was going to let me finish the dissertation uninterupted, along came Connor. Although he arrived late to the process, he made up for lost time with intensity. Under Hunter's careful tutelage soon Connor was even better at dragging daddy out of the dungeon than Hunter was. While it may not have seemed like I appreciated it at the time, it always brightened my day. Thanks, boys!

Special thanks to LTC Rod Liu and Steve Cramm. Rod encouraged me to start the program, and gave me high cover at work when I needed to get away to school. Steve

x

also has been remarkably supportive. The first time Steve and I talked about this, I was studying for the qualifiers and Steve started grilling me on what I was doing. I was new to the job and concerned that he wouldn't like a guy getting ready to run half our missions not being 100% focused on work. Of course, Steve already knew all about the Ph. D., (unbeknownst to me!) but was just testing me. I promised not to let it interfere with work too much and I have (mostly) lived up to my end. Thanks for not hammering me when it did interfere. Finally thanks to LTC Dave Bujold, Major Tim Woods, and LTC Steve DiDomenico—all squadron commanders who have had to play a man down at one point or another because their Flight Commander, or Operations Officer was out playing college student. Thanks!

I would like to thank the Hertz Foundation. They took a big risk with me, and I appreciate their faith. In particular I would like to thank Dr. Weaver for his support of my efforts and for helping me financially to minimize the impact on my family. I think that having the fellowship also helped UNLV take me a little more seriously when I walked in the door.

I would also like to thank the faculty and staff of the UNLV physics department. They have been more than willing to meet me half way when work conflicted with school. While wars have a way of ruining your schedule, the department was very reasonable. Again thanks.

Finally, I want to thank Dr. Weistrop for agreeing to take me on. I have learned a lot from you and I have tremendous respect for your knowledge, perseverence, and mentorship. Even though she is a very busy woman, she always had time to help me, answer a question, or listen to my latest wild theory. You have been nothing but reasonable throughout this whole endeavor. Thank you so much!

This work has been supported in part by NASA, under contract NAS5-31231 and the Nevada Space Grant Consortium.

CHAPTER 1

INTRODUCTION

When a galaxy goes through a period of such rapid, intense, star formation that a significant fraction of the total flux from the galaxy is due to the star formation, it is called a "starburst galaxy," or just a "starburst." Starbursts are often associated with gas rich galaxy interactions and mergers. Holmberg (1958) was the first to notice that blue galaxies tend to have blue companions. This was built upon by several researchers including Larson and Tinsley (1978) who first posited that the blue excess was due to star formation. Since then there has been much work particularly by Kennicutt et al. (1996) and Leitherer (1999) to catalog starbursts and synthesize starburst spectra.

The theory behind starburst phenomena is as follows. A gas-rich galaxy interacts with another galaxy (which may or may not also be gas-rich). The interaction causes a tidal perturbation which induces the gas to coalesce into knots of star formation. As the knots become denser they attract more gas, which raises the density more which attracts more gas, etc. This positive feedback continues until the gas is locally exhausted, or the winds and radiation from the massive stars disrupt further star formation. As the gas condenses, it forms stars with a stellar mass distribution described by the initial mass function (IMF). The IMF characterizes the number, $N(M)$, of stars with mass M in the interval dM as a power law with exponent value, α, according to the formula

1

$$N(M)\,dM \propto \left[\frac{M}{M_\odot}\right]^{-\alpha} dM \qquad (1)$$

We study starbursts because recent evidence indicates mergers and interactions may have played a large role in galaxy evolution in the past (Lowenthal et. al. 1997). Indeed, the Milky Way is currently in the process of merging with at least one dwarf galaxy (Ibata et al. 1995) and some ellipticals may have formed from mergers (Zepf 1997). By studying mergers and interactions, we hope to understand galaxy evolution better. Furthermore, mergers have been hypothesized to produce the precursors of globular clusters (Ashman & Zepf 1992). Since instantaneous starbursts form a large number of stars more or less simultaneously (on an astrophysical scale), and globular clusters are large numbers of more or less identically aged stars, this is a somewhat natural connection.

We also study starbursts to gain insight into the IMF, in particular to determine if the IMF is constant for starbursts as well as lower levels of star formation in galaxies, or if stars form with different mass distributions in different star forming environments. Another reason to study starbursts is because so many stars are forming, there is a comparatively large population of massive stars, which tend to be rare relative to their lower mass counterparts. Even though we cannot resolve individual stars, we have an opportunity to observe in aggregate a statistically significant population of short-lived, super-massive stars.

Previous Work

The interacting system NGC 3395/NGC 3396 has been well studied, particularly in surveys of starburst galaxies and star formation. In addition to their listing in the New Galactic Catalog (1888), they are listed as number 270 in the Atlas of Peculiar Galaxies by Arp (1966) and as objects 5931 and 5935 in the Uppsala General Catalog of Galaxies (UGC) by Nilson (1973). NGC 3395 is a SAB(rs)cd pec with m_b=12.4 and NGC 3396 is an IBm pec with m_b=12.6 (Huchra et al., 1995). From ground observations, the galaxies have a strong blue and UV excess which caused them to be observed by the International Ultraviolet Explorer (IUE). The IUE observations were included in the Kinney et. al. (1993) atlas of ultraviolet spectra of star forming galaxies.

Clemens et. al. (1999) used VLA observations and modeling to examine the H I content of the galaxies and determined that their last perigalactic passage was approximately 50 Myr ago. Also, Huang (1994) formed a radio map of the galaxies and found that the center of radio flux was not centered in the nuclei of the galaxies, but rather each galaxy's radio flux was biased on the side toward its companion galaxy.

The galaxies are a strong unresolved far-infrared source (Soifer, 1987), while ROSAT X-Ray data show emission roughly centered in both galaxies, but with the NGC 3396 emission shifted 27" toward NGC 3395 (Read & Ponman, 1998). The galaxies also exhibit Wolf-Rayet Galaxy characteristics and were included in the WR galaxy catalog of Schaerer et al. (1999).

The galaxies have also been studied spectroscopically, including by D'Odorico (1970) and Carpenter (1957). D'Odorico measured the spectra from 4300-6800 Å using a ground based spectroscope and primarily studied the dynamics using optical emission lines. Carpenter examined filaments between the galaxies in [O II] λ3727. Balzano

(1983) obtained ground based spectra of the NGC 3395 nucleus and identified it as having starburst signatures. To date while there have been spectroscopic studies, none has looked in detail at the resolved optical and UV spectra for starburst signatures. Our analysis has been made possible only by the high spatial resolution of the Space Telescope Imaging Spectrograph on board the Hubble Space Telescope.

Hancock et al. (2003) performed an extensive imaging survey of the galaxies using the Space Telescope Imaging Spectrograph on board the Hubble Space Telescope. They found that the FWHM of most of the star forming knots was ≤ 20 pc with E(B-V) of 0.0 to 0.3 and a mass less than 10^6 M$_\odot$. They used the Starburst 99 models of Leitherer et al. (1999) to estimate the age of most of the knots as ≤ 80 Myr.

Overall Objective

The primary objective of this work is to perform a spectroscopic study of the starburst galaxies NGC 3395 and NGC 3396. We will examine several starburst knots and determine metallicity, age, and investigate starburst propagation across the galaxies.

We will examine the metallicity of our knots and look for gradients in the metallicity as a function of position. Metallicity gradients, if they reveal a pattern of enrichment, could serve as a proxy for starburst propagation across the galaxies. We will also examine the unresolved spectra of the galaxies, simulating the spectra one would obtain from galaxies at much higher redshift, and evaluate how representative their metallicities are of the underlying metallicities of the resolved knot structure.

Following the metallicity evaluation, we will seek to characterize the IMF of the star forming knots. We will attempt to characterize the most massive knots, and look for

consistency in the IMF between the galaxies. We will also examine the variation of the ages we derive with the assumed IMF.

Finally, we will evaluate the age of the knots via several modeling techniques. We will examine the resultant ages for consistency with one another and with the spectral features of the knots. We will attempt to derive a best estimate of the age of the starburst population and any older underlying population it is superimposed on. We will also attempt to discern any age gradient which would provide insight into whether the star formation propagates across the galaxies, or if it occurs more or less simultaneously across the galaxies. Finally we will examine the ages we derive for the unresolved spectra and determine how representative they are of the underlying resolved star forming knots. As in the metallicity analysis, this will be of interest at high redshift when one cannot resolve the star forming knots even with the the HST, due to the extreme distance involved.

CHAPTER 2

DATA COLLECTION

Observations were obtained on the interacting galaxy pair NGC 3395/3396 using the

Hubble Space Telescope (HST) Space Telescope Imaging Spectrograph (STIS). This

chapter will briefly review the HST, the primary observing sensor, the observational

technique, and the actual observations.

The Hubble Space Telescope

The HST is a satellite based 2.4m reflecting telescope flying in low earth orbit. It is

a joint European Space Agency and National Aeronautics and Space Administration

program. Operations and technical support are provided by the Space Telescope Science

Institute (STScI). HST has a variety of sensors including the Wide Field/Planetary

Camera 2 (WFPC2), the Space Telescope Imaging Spectrograph (STIS), the Advanced

Camera for Surveys (ACS), and the Near Infrared Camera and Multi-Object

Spectrometer (NICMOS). This paper will present the results of an analysis of STIS data.

Space Telescope Imaging Spectrograph

STIS employs three large (1024x1024) detectors with overlapping wavelength

coverage in order to span all wavelengths from 1150-11,000 Angstroms. The long

wavelength (2000-11,000 Angstrom) detector is a semiconductor charge coupled device

6

(CCD) with a spatial scale of 0.0507 arcseconds per pixel and a 51x51 arcsecond field of view (FOV). The CCD counts photons indirectly by counting electrons liberated by interaction with the incident photons. For ultraviolet observations there are two multi-anode microchannel arrays (MAMAs) available--one for the 1600-3100 Å near ultraviolet (NUV) and one for the 1150-1700 Å far ultraviolet (FUV). Both have a 0.024 arcsecond spatial scale with a 25x25 arcsecond field of view. Like the CCD, the MAMA detectors also count photons indirectly, but in this case the photons are incident on a micro-channel plate which releases electrons. The released electron cloud is amplified and finally the detector counts the burst of electrons.

STIS is capable of imaging as well as slitless, echelle, or long-slit spectroscopy. Incoming photons can be filtered and/or diffracted using a prism, filters, and gratings. The data presented here were collected using the long slit (52x0.5 arcseconds) spectrographic mode. The FUV data were diffracted using the G140L long slit grating and no filter. This grating provided a spectrum from 1118-1716 Å with an average dispersion of 0.584 Å/pixel. An optical data set was collected using the CCD with the G430L grating and no filter. The spectrum extends from 2900-5712 Å with an average dispersion of 2.746 Å /pixel. Lastly, a far red data set was collected by employing the CCD with the G750L grating and no filter. The far red spectrum covers 5271-10265 Å with an average dispersion of 4.882 Å/pixel. The comparatively low resolution is a result of a trade off: to increase spectral range we must decrease spectral resolution. Furthermore, since the targets are very faint, to obtain adequate signal-to-noise ratio only low resolution was feasible.

STIS Observation Methodology

The following is a brief synopsis of typical STIS operations. For further detail, please refer to the HST Data Handbook. A STIS observation consists of three phases: target acquisition, calibration, and observation.

The observational target is acquired as follows. First a gross alignment takes place via the satellite's attitude control system and guide stars. After gross alignment, the target will be within 1-2 arcseconds of the center of the STIS field of view. Then, since the 0.5 arcsec slit was used, a target acquisition exposure was taken with the CCD. Based on the acquisition exposure, a final correction is made to put the target at the center of the aperture and a final acquisition exposure is taken. Since the targets were distributed targets (galaxies) and the slit was greater than 0.1 arcseconds, no peak-up exposures were required or taken.

Next the grating is placed into the optical path via a rotary wheel called the mode select mechanism (MSM). Unfortunately the MSM's positional alignment is non-repeatable and can introduce a shift of up to 10 pixels in the resulting spectrum's location on the detector. Therefore, following target acquisition, a calibration, called a wavecal, must be performed. A wavecal is an image taken when the light from the aperture is shunted away and an onboard tungsten calibration lamp illuminates the grating instead. Using the known emission line wavelengths of the tungsten lamp, a correction matrix can be developed from the wavecal. Then the same correction matrix can then be convolved with the target observational data post mission. By employing the wavecal as a baseline, the scale and alignment of the target observation can be determined.

For far red observations, a contemporaneous flatfield image is also required. Typically two flatfield exposures are collected in order to create a final cosmic ray

rejected flatfield. The final flatfield image is used during post-mission processing to defringe the data (see data reduction).

Finally, the data are collected over a series of orbits. Collected data are read out of the detector arrays into an onboard tape recorder for later telemetry to the STScI ground station for post processing and distribution.

NCG 3395/3396 Data Collection

Observations were taken of the interacting galaxy pair NGC 3395/3396 as part of proposal 8028 on the HST eighth observing cycle   Tables I and II contain a summary of the observations. In the tables, column (1) is the STIS detector and grating employed; columns (2) and (3) are the universal date and time of the observation; column (4) is the exposure time in seconds; and column (5) is the type of data collected, data or flatfield. To enable removal of cosmic ray artifacts, there are two CCD observations per galaxy and per data type. The MAMA detector is insensitive to cosmic rays; however to obtain the requisite signal to noise there are also two FUV observations per galaxy which were then combined.

Slit placement was selected based on imaging data in order to maximize starburst data collection. In NGC 3396 this is basically along the center of the galaxy, but in NGC 3395, the placement is designed to maximize collection along one particular large starburst knot and as such is not through the nucleus of the galaxy. Figure 1 contains a ground based image from the 40-inch telescope at Mt Laguna Observatory (D. Weistrop and C. Nelson) with the HST slits superimposed on it.

Table I. NGC 3395 Space Telescope Imaging Spectrograph Observation Log

Detector[a]	Date (UT)	Time (UT)	Exposure (s)	Type
FUV/G140L	30 January 1999	16:42:04	2100	Data
FUV/G140L	30 January 1999	18:03:06	800	Data
CCD/G430L	30 January 1999	18:23:12	300	Data
CCD/G430L	30 January 1999	18:28:56	300	Data
CCD/G750L	30 January 1999	18:39:37	322	Data
CCD/G750L	30 January 1999	18:45:43	360	Data
CCD/G750L	30 January 1999	18:53:09	5	Flatfield
CCD/G750L	30 January 1999	18:54:40	5	Flatfield

[a]FUV=Far ultraviolet multi-anode microchannel array. CCD=Charge coupled device detector. G140L, G430L, and G750L are STIS gratings

Table II. NGC 3396 Space Telescope Imaging Spectrograph Observation Log

Detector[a]	Date (UT)	Time (UT)	Exposure (s)	Type
FUV/G140L	25 March 1999	08:38:54	2332	Data
FUV/G140L	25 March 1999	10:15:41	300	Data
CCD/G430L	25 March 1999	10:25:49	275	Data
CCD/G430L	25 March 1999	10:31:08	275	Data
CCD/G750L	25 March 1999	10:41:24	600	Data
CCD/G750L	25 March 1999	10:46:44	245	Data
CCD/G750L	25 March 1999	10:52:15	5	Flatfield
CCD/G750L	25 March 1999	10:53:46	5	Flatfield

[a] FUV=Far ultraviolet multi-anode microchannel array. CCD=Charge coupled device detector. G140L, G430L, and G750L are STIS gratings
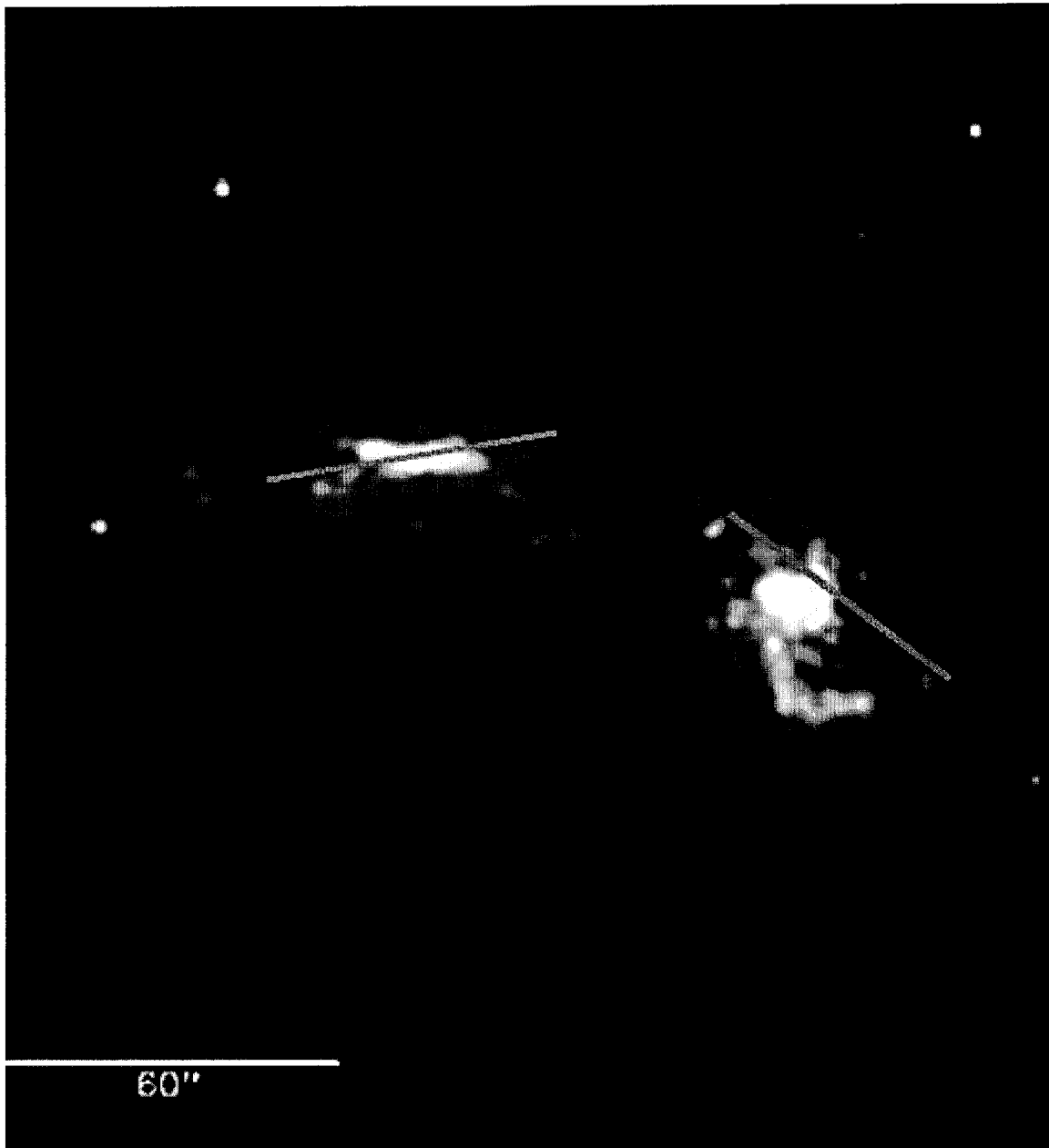
Figure 1. NGC 3395 and NGC 3396 With Slit Superimposed

Ground based image from the 40-inch telescope at Mt. Laguna Observatory by D. Weistrop and C. Nelson. In the figure north is up and east is left. NGC 3395 is the western galaxy, NGC 3396 is the eastern galaxy. The slits are 50" long.

CHAPTER 3

DATA REDUCTION

All data were reduced from detector counts to flux units using two standard software packages: the Image Reduction and Analysis Facility (IRAF) and the Space Telescope Science Data Analysis System (STSDAS). IRAF and STSDAS are powerful command line oriented astronomical data analysis packages. IRAF creates a virtual operating system and in addition to its built-in functionality, it provides an environment for programming and scripting of analysis routines. STSDAS is an extension to IRAF to cover Hubble Space Telescope (HST) specific data reduction and processing. Every effort was made to use standard IRAF and STSDAS utilities, but it was necessary to develop scripts and unique programs in order to perform some of the processing. Where standard IRAF routines are used, we will discuss how they were used to achieve the desired goal, but detailed implementation will not be addressed.

The workhorse of the data reduction was the STSDAS routine CALSTIS. The HST Data Handbook provides an excellent reference on CALSTIS and the interested reader is referred there for details beyond what is presented here. CALSTIS is the standard STIS pipeline calibration routine and performs a variety of functions including basic two-dimensional image reduction, contemporaneous wavelength calibration processing, and spectroscopic calibration.

12

Basic Two-Dimensional Image Reduction

Raw sensor counts need to be corrected for numerous data collection artifacts. Additionally, an error array is associated with each STIS data set. The basic two-dimensional image reduction calculated the error arrays and performed numerous corrections on the data depending on which sensor collected them.

Data collected with the CCD are corrected for bias and systematic detector effects, and have cosmic ray artifacts removed. As a semiconductor device, the CCD has some baseline thermal noise in the detector. It has a thermoelectric cooler to minimize it, but there is still some residual noise. Furthermore, the CCD has a bias applied to achieve a minimum number of electrons in each pixel and to improve the charge transfer efficiency. To account for these effects, the outer edge of the detector (called the overscan region), which has the same bias and temperature as the rest of the detector, is shielded from target illumination. The overscan region for each line in the detector is used to calculate a bias as follows. For each line, the overscan pixels are averaged then the averages from all the lines are fit by a linear regression. Then for each line, the value of the fit at that line is subtracted from each pixel in the line. Finally the overscan regions are clipped off the science image.

Following bias subtraction, artifacts from cosmic rays are removed from CCD data. As mentioned previously, the CCD counts electrons. The detector is designed to produce a number of electrons in direct proportion to the number of photons with wavelengths in the CCD's sensitivity range, the constant of proportionality being the quantum efficiency. Typically, the CCD bias voltages are set in such a way as to prevent saturation; however cosmic rays, very highly energetic elementary particles, can penetrate the shielding around the CCD and liberate many electrons. This causes the detector to generate

erroneously high or low (due to overflow) values for a given pixel. To remove cosmic ray artifacts, two exposures were collected and then an iterative pixel by pixel comparison was performed. Isolated anomalously high or low pixel values which appear in one image, but not the other, are flagged as cosmic ray artifacts in the data quality array and replaced by a local average in the science array. Finally, the exposures are combined into an exposure weighted average data image.

Unfortunately, CALSTIS was not 100% effective in removing cosmic ray artifacts. In an effort to improve the cosmic ray artifact removal, the IRAF routine "COSMICRAYS" was also employed. This routine created a moving 7x7 window and designated the brightest pixel in each window as a candidate cosmic ray artifact. The routine then calculated the local average and standard deviation of the pixels surrounding the candidate excluding the second brightest pixel (which may have been part of the cosmic ray artifact). If the candidate cosmic ray artifact was more than 5 sigma above the local average, then the window was fit with a plane and the average background was subtracted. A flux ratio, defined as the flux of the brightest pixel to the background flux, was calculated as was the background subtracted flux of the candidate pixel. Then the process was repeated on the next 7x7 pixels. After the complete image had been filtered, a plot of flux vs. flux ratio was generated. The user then selected a cutoff flux ratio and all candidates which exceed it were declared artifacts. Each artifact was then replaced by the average of the four pixels surrounding it. Following this removal suspect candidates that didn't trigger the automatic filter were further examined by hand using a local surface plot.

Since data were read out into a 16 bit register, it was possible for a cosmic ray to overflow this register and generate anomalously low values as well as anomalously high

values. We therefore used the IRAF "IMARITH" routine to invert the data (all pixels multiplied by negative one) and reran cosmic rays as described in the previous paragraph.

Following cosmic ray artifact removal another bias subtraction was performed. This subtraction employed a "superbias" image to take out systematic localized features in the zero-point electronic bias of the detector. The superbias was a very high signal to noise image collected over several frames.

After removal of the zero-point bias, a "superdark" file was subtracted from the data. The superdark is updated weekly by STScI and I further updated the appropriate superdark with the daily dark file, which STScI routinely collects. These "dark" files are zero illumination data which account for defective/damaged pixels and accumulated thermal noise above and beyond the thermal bias correction mentioned previously.

The final step was to correct for pixel-to-pixel and large scale sensitivity variations by using a flatfield image. A flatfield image is an image produced by a uniformly illuminated detector. Since the detector is uniformly illuminated, so too should the resultant image be, but of course there are small differences due to defects in the detector and non uniform gain. In an attempt to correct for this, we normalize the flatfield image to one and then divide the science image by it.

For far-red observations, the wavelength of the incident photons can be on the order of the thickness of the CCD. The photons can interfere with each other and the result can be strong fringing longward of 7,000 Angstroms (STIS ISR 97-16). To correct for this effect, the data were corrected or "defringed" by another flatfield, called the "contemporaneous flatfield." Despite its name, the contemporaneous flatfield is collected just after the observation, not simultaneously with the observation. The contemporaneous flatfield was an exposure that used the onboard tungsten lamp applied to the G750L

grating as a source to illuminate the detector. Basically, the data set was normalized and compared to the normalized contemporaneous flatfield image. We identified a region of the data image with no target data which should have been "flat." A computer algorithm compared this "flat" data image region to the same region in the contemporaneous flatfield image. The contemporaneous flatfield was then shifted in the dispersion axis and compared again until the "best" offset for the dispersion axis was found.

Once the offset was determined, a similar procedure was followed to determine the "best" value to scale the contemporaneous flatfield. Finally the science image was "defringed" by flatfield correcting it using the shifted and scaled contemporaneous flatfield image.

MAMA data followed a similar processing path with a few major differences. First, the raw MAMA data were actually subsampled to 2048x2048 pixels and binned into the standard 1024x1024 format prior to any further processing. Then, rather than a bias correction, the MAMA data undergo linearity corrections. At the global level, if the global count rate exceed 300,000 counts per second, both the hardware and software can not keep up. At local level, for high local count rates ($>\sim 200$ counts/second/pixel) the MAMA detectors become nonlinear due to charge depletion. The STSDAS software attempts to flag the non-linear data and correct it if possible.

Since the MAMA actually counts "bursts" of liberated electrons, not integrated electron charge as in the CCD, there is no need to correct MAMA data for cosmic ray artifacts. Following the linearity correction, the MAMA data are corrected for damaged/defective pixels by using a "super dark" and divided by the flatfield images to correct for pixel-to-pixel variation in the same manner described above for the CCD.

Finally since the wavelength of the UV photons is much less than the thickness of the detector, the MAMA data exhibit no fringing and thus require no fringing correction.

Wavelength Calibration

As mentioned in the chapter on data acquisition, the mode select mechanism used to select gratings for spectroscopic work does not put the target spectrum on exactly the same part of the detector every time. In order to correctly calibrate the spectrum dispersion axis, a contemporaneous wavecal exposure was taken. Then using the known emission wavelengths of the tungsten lamp spectrum, the pixel offset was calculated for the science data and thus accurate wavelength measurements could be performed on the science data.

The first step in the calibration was to perform the basic two-dimensional image reduction on the wavecal exposure. The wavecal is a short, single exposure on the detector of interest which was processed just as the science data were with the exception of cosmic ray artifact removal for the CCD.

To remove cosmic ray artifacts from CCD wavecals, since the expected spectrum was known and should have been spatially constant, the software looked for outliers in the spatial direction and tagged probable cosmic rays which were replaced with a local average.

After flat fielding, the resultant wavecal image was compared with a template image of the expected tungsten lamp emission spectrum to develop shifts to apply to the science data.

Spectroscopic Processing

Following image reduction and wavelength calibration the final processing was applied. The spectra were converted to heliocentric wavelengths and fluxes were calculated from the counts using a point source response function. The output of all the above is "a rectified output image with a linear wavelength scale and uniform sampling in the spatial direction." (HST Data Handbook). A final quality check was made to ensure that spectra were parallel to the dispersion axis.

To increase the signal to noise of the FUV MAMA data, following all other processing, both FUV MAMA exposures were weighted by the exposure time and combined into one image using the IRAF routine MSCOMBINE.

CHAPTER 4

POSITIONAL ANALYSIS AND RESULTS

One of the objectives of this research is to compare the spectra of several starburst

knots To ensure an accurate comparison, it is important to spatially align data from all

three of the gratings used: G140L, G430L and G750L. This chapter details the alignment

procedure and presents spectra for the knots defined.

Background

Data were taken with the STIS using the 52x0.5 arcsecond slit. The slit was

positioned on the galaxies in such a way as to measure several bright star-forming knots

simultaneously. The STIS detectors offer high spatial resolution; however for a variety

of reasons, it may be difficult to spatially correlate the spectra from the different gratings

correctly. As detailed in the data reduction chapter, the data go through several detector

and grating specific corrections and rotations which can induce offsets in the physical

pixel location of the spectra on the detector.   Also, placement of the mode selection

mechanism is not 100% repeatable--there are small, unpredictable differences in both

spatial and dispersion alignment every time the wheel moves. Finally, the measurements

occurred over a series of orbits, and the satellite's pointing mechanism allowed for small

differences in the physical placement of the target spectrum on the detector. The wavecal

calibrates the dispersion alignment of each detector to correct for these errors, but there is

19

no such pipeline calibration for the spatial axis. The above mentioned factors result in small differences in the physical location of the spatial features on the detectors i.e. the center pixel of one detector may not point at exactly the same position in the sky as the center pixel of another detector. It is therefore critical to develop a procedure to define the spatial knots across multiple detectors and wavelength regions.

Alignment Procedures

Since wavelength is the horizontal axis of the two-dimensional spectra (the vertical is spatial distance along the length of the slit) the bright continua of the knots appear as horizontal lines. To properly spatially align the spectra the following graphical technique was used. Each detector's data had a particularly bright knot continuum near the spatial center of the array. This feature was much brighter than the neighboring knots. We therefore assumed that the central bright horizontal line in each detector was from the same source knot. We then calculated a spatial offset for each detector to align the bright central continua exactly in the spatial direction in all three detectors.

After adding the offset, we plotted all three detector datasets on the same graph using an arcsecond scale, not a pixel scale. In order to gain an adequate signal to noise ratio for the purpose of knot definition, the data were averaged in the dispersion axis for each detector. We were careful to select a wavelength region where there was no significant emission: pixels 408-468 corresponding to wavelengths of $\lambda\lambda$1305-1340Å, $\lambda\lambda$3751-3913Å, and $\lambda\lambda$6771-7063Å for the G140L, G430L and G750L spectra respectively.

Finally, two additional scales were added, a top scale showing MAMA pixel values, and a bottom scale showing CCD pixel values. It is important to stress that the pixel

values are the parameter of interest. We defined knots in terms of the integer pixels that they subtend in each detector.

The final product is a spatial flux profile along the slit. Figure2 (page 23) shows a sample result. The flux from each detector was scaled to facilitate knot identification. The scale factors are denoted in the legend on the figure. Notice that the central maxima overlay each other exactly and the spatial extent of each knot is defined in all three detectors.

Knot Selection

The graphical technique described above was used to generate spatial flux profiles along the slit. In the interest of brevity, we will use the term "knot" to denote morphological features in the spatial flux profile along the slit.

Knots were selected based on two criteria. The knot had to persist at all wavelengths (except perhaps absorption lines) and had to be at least two pixels wide spatially. Due to random noise and hot pixels, it is possible for features to appear which are not truly knots. For instance, if by chance, there are some hot pixels in a particular wavelength averaging window, it may appear that there is a spatial feature at that location. By examining several different wavelength windows and keeping only those knots that persist in all of them, the potential for this type of error is drastically reduced.

A quality check was performed by visual inspection of the two-dimensional spectra. After suitable adjustment to the intensity scaling, if a horizontal line could not be discerned (i.e. a spatially distinct spectrum) then the knot was discarded. While this procedure introduced the potential to discard valid knots, if they were so weak as to not show up for a visual inspection there would have been inadequate signal to noise ratio to

perform a valid measurement. Fortunately, there were very few candidates that were rejected in this way.

As a final quality check, imaging data from STIS (Hancock et al., 2003) were compared to the spectral data to find the image features. Data are cross referenced between the spectra and the imaging data (where available) for both galaxies. This was done as a sanity check to make sure we had spectra for all the bright knots in the image. Arbitrary names were given to the knots to facilitate discussion.

For analysis purposes, in each galaxy we also defined a knot that consisted of the entire portion of the galaxies observed by the slit. These knots do not represent the entire galaxy, but rather the portion we observed and are named NGC 3395 and NGC 3396 respectively. They will be used to simulate the spectrum that would have been taken by a low spatial resolution spectrograph. We will compare and contrast these "unresolved" spectra to the spectra from the individual knots.

NGC 3395 Measurement Knots

The analysis method described above was applied to NGC 3395. Figure 2 shows the spatial flux profile and the knots that were defined from it. In Table III, column (1) is the name of the knot, which is arbitrary; column (2) is the pixel row coordinates in the STIS FUV MAMA detector with the G140L grating; column (3) is the pixel row coordinates in the STIS CCD detector with the G430L grating; column (4) is the pixel row coordinates in the STIS CCD detector with the G750L grating. Figure 3a-l presents the spectrum for each individual knot.
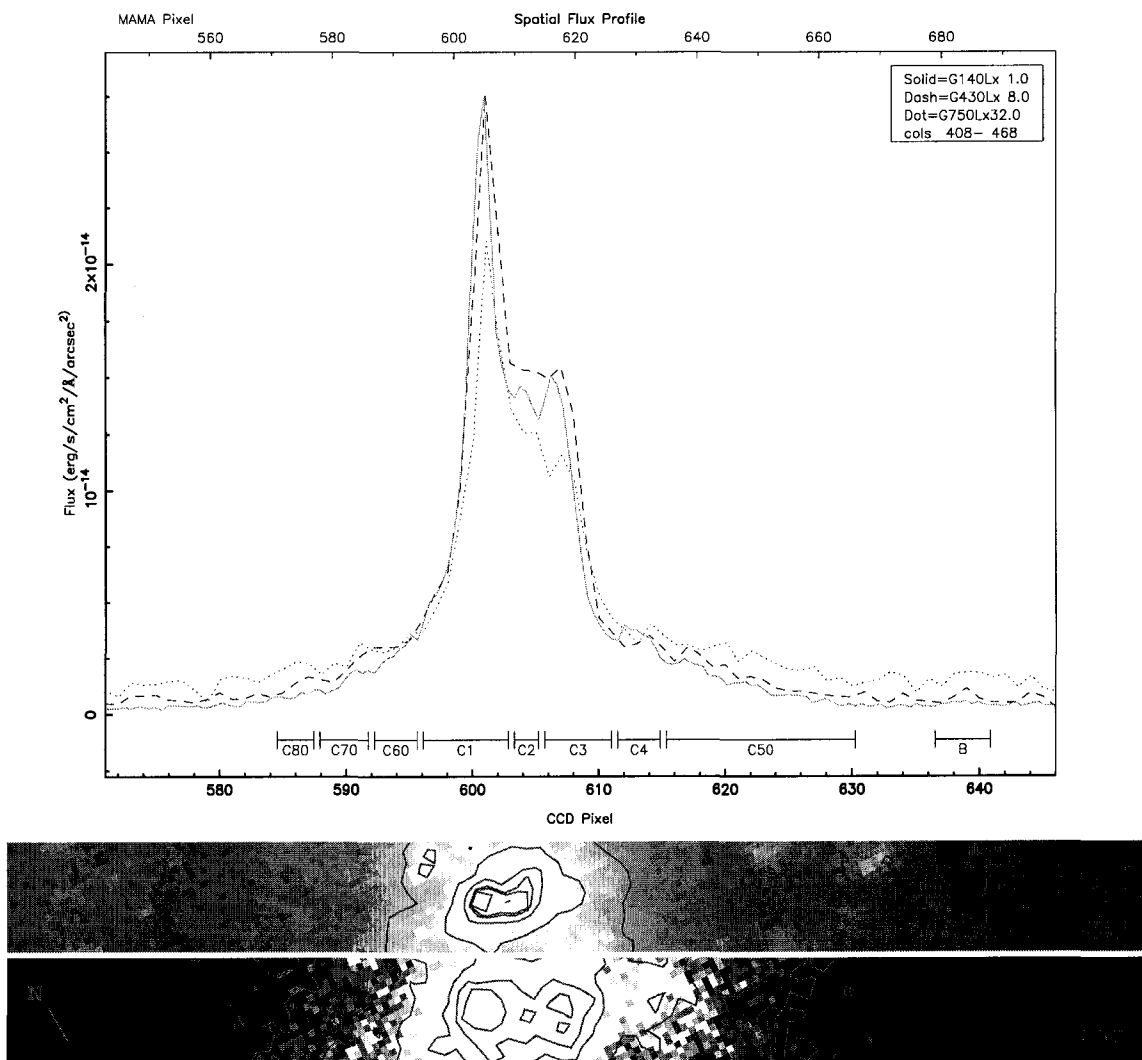
Figure 2. NGC 3395 Spatial Flux Profile.

In the top panel, the solid line is the G140L spectra, the dashed is G430L and the dotted is G750L. The legend box provides dispersion columns averaged and the scale factor applied to each detector. The knot names are depicted above the horizontal axis (note: in the interest of clarity, the image is zoomed in on the most interesting section and not all of the knots are shown). The middle panel shows the STIS visible image for the slit region and the bottom panel shows the FUV image of the slit region from Hancock et al. (2003). Intensity contours have been drawn on the images to enhance clarity. Note these images are for illustration purposes only: there are small errors in the relative alignment and scaling between the three panes.

Table III. NGC 3395 Measurement Knots

Knot[a]	FUV MAMA G140L[b]	CCD G430L[b]	CCD G750L[b]
D	161-181	388-397	387-396
C80	571-577	585-588	584-587
C70	578-586	589-593	588-592
C60	587-594	594-596	593-595
C1	595-609	597-603	596-602
C2	610-614	604-606	603-605
C3	615-626	607-611	606-610
C4	627-634	612-615	611-614
C50	635-666	616-631	615-630
B	679-688	637-641	636-640
A	783-796	687-693	686-692
NGC3395	100-900	357-742	358-743

[a] Knot names are arbitrary.

[b] Locations are the STIS rows of interest in detector pixel coordinates
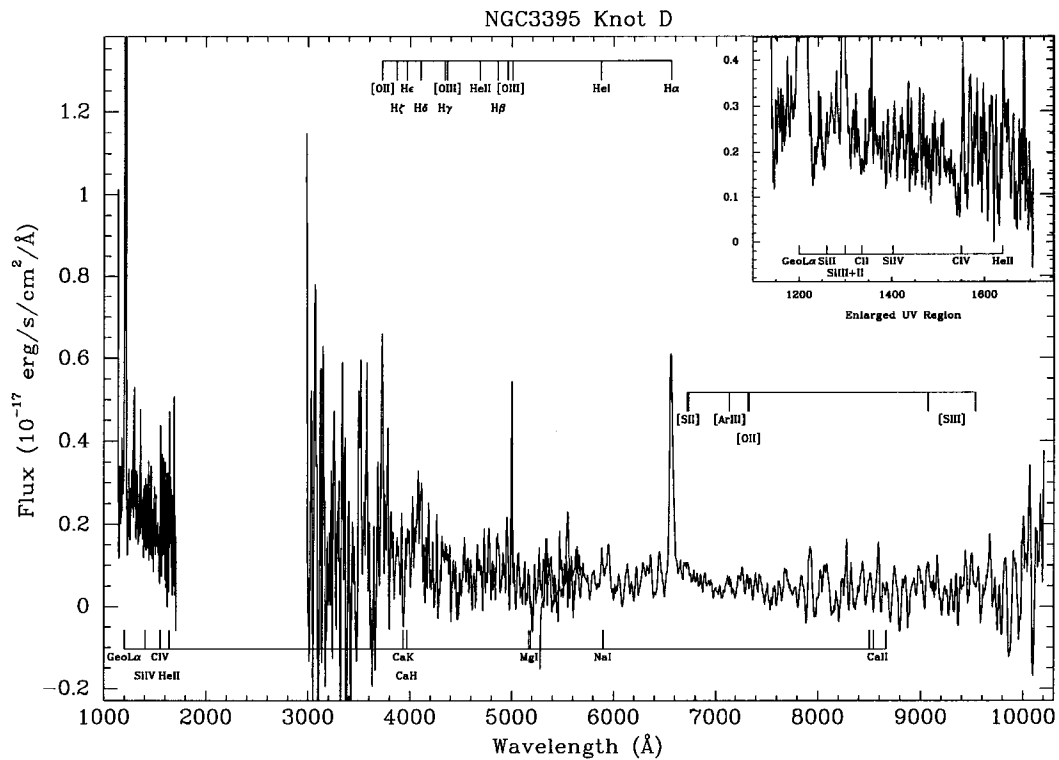
Figure 3a. NGC 3395 Knot D

Figure 3a-1. NGC 3395 measurement knots. Each figure has been blueshifted by a velocity of 1625 km/s (NASA/IPAC Extragalactic Database) to the rest frame and boxcar smoothed by 5 pixels. Across the top/bottom of the figure, the rest wavelength of several emission/absorption lines is denoted. Geo Lyα stands for geocoronal Lyman α. There is a break between approximately 1700-2800 Å where no data were taken. The names of the knots were assigned somewhat arbitrarily, so the figures are not presented alphabetically, but rather based on spatial slit position, from the top of the detector to the bottom except for the unresolved knot which is presented last.

NGC3395 Knot C80

Figure 3b. NGC 3395 Knot C80

NGC3395 Knot C70

Figure 3c. NGC 3395 Knot C70

Figure 3d. NGC 3395 Knot C60

Figure 3e. NGC 3395 Knot C1
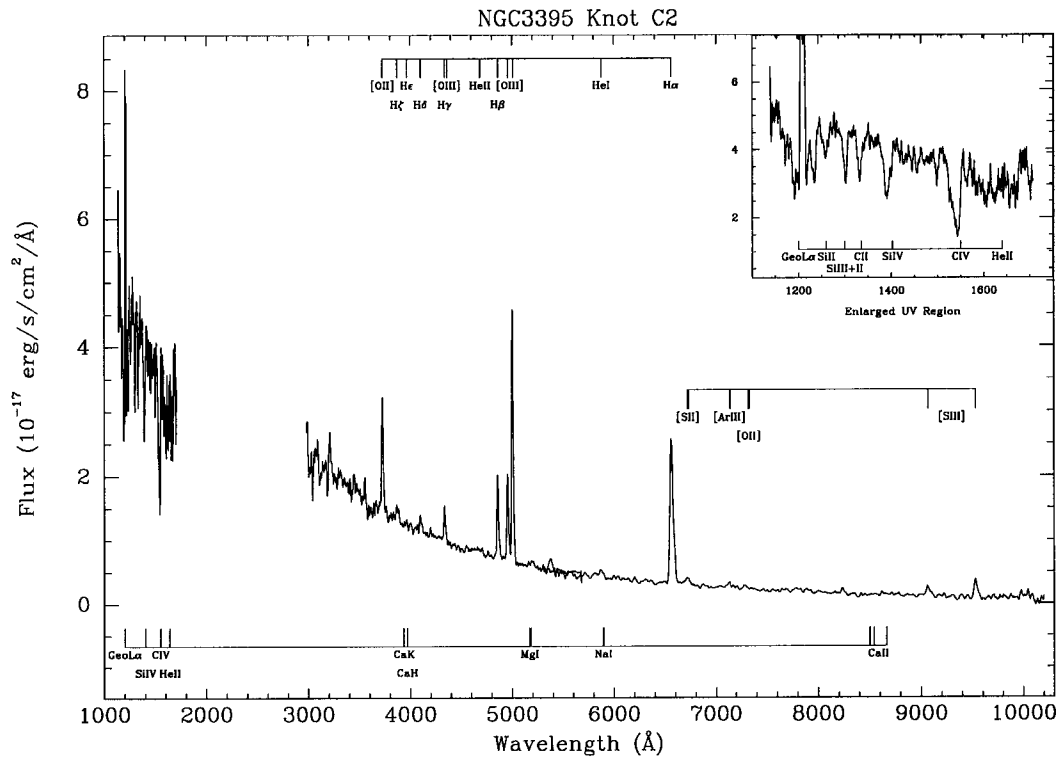
Figure 3f. NGC 3395 Knot C2

Figure 3g. NGC 3395 Knot C3
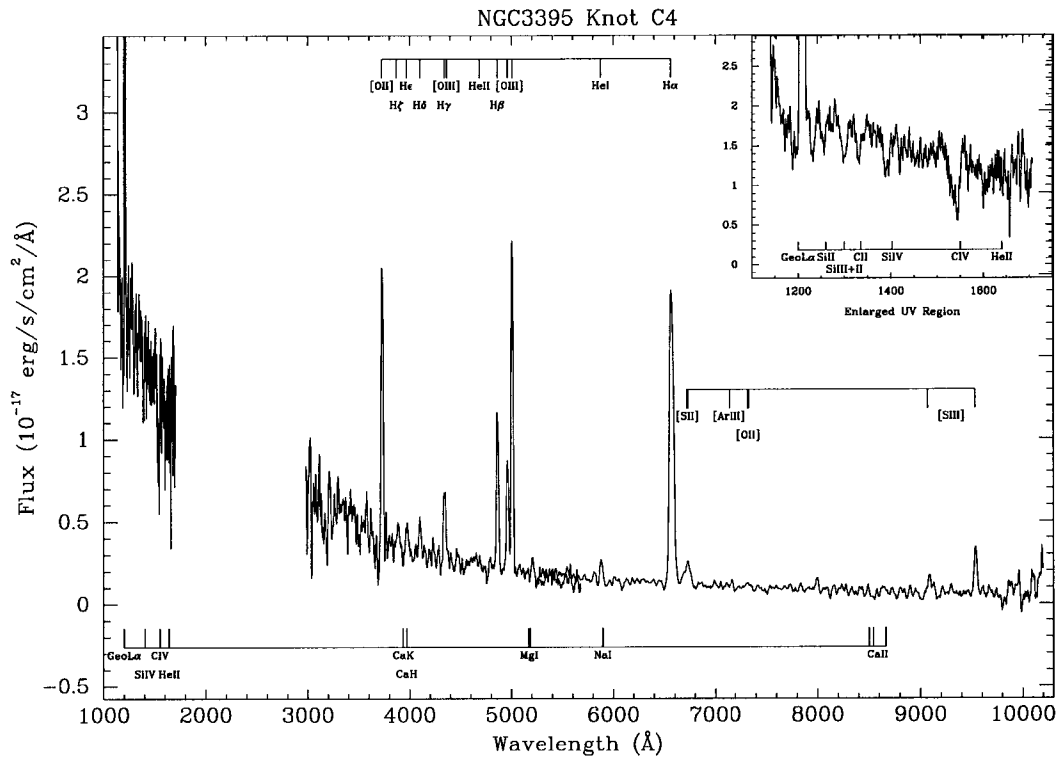
NGC3395 Knot C4

Figure 3h. NGC 3395 Knot C4
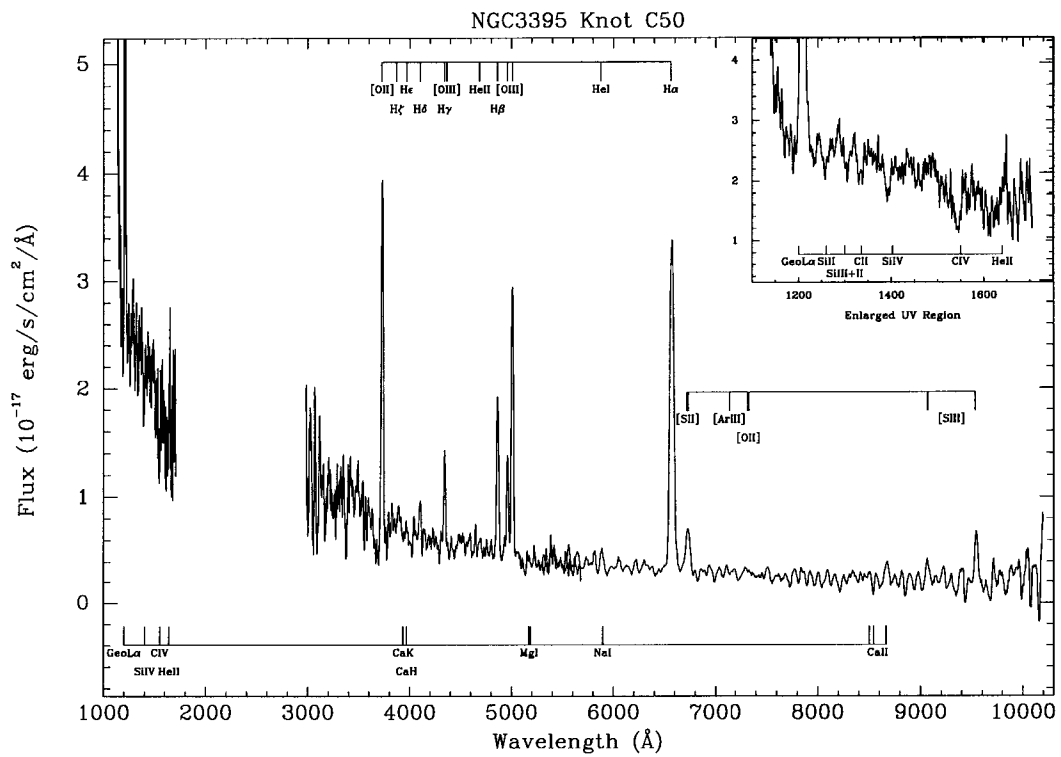
NGC3395 Knot C50

Figure 3i. NGC 3395 Knot C50
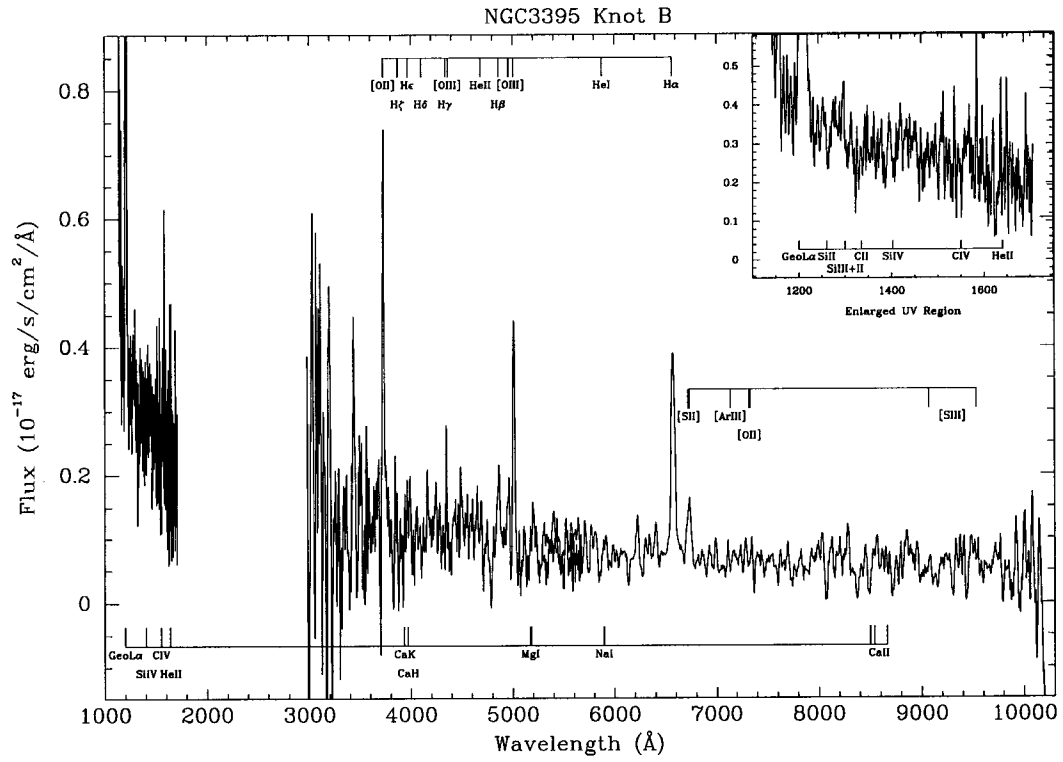
Figure 3j. NGC 3395 Knot B
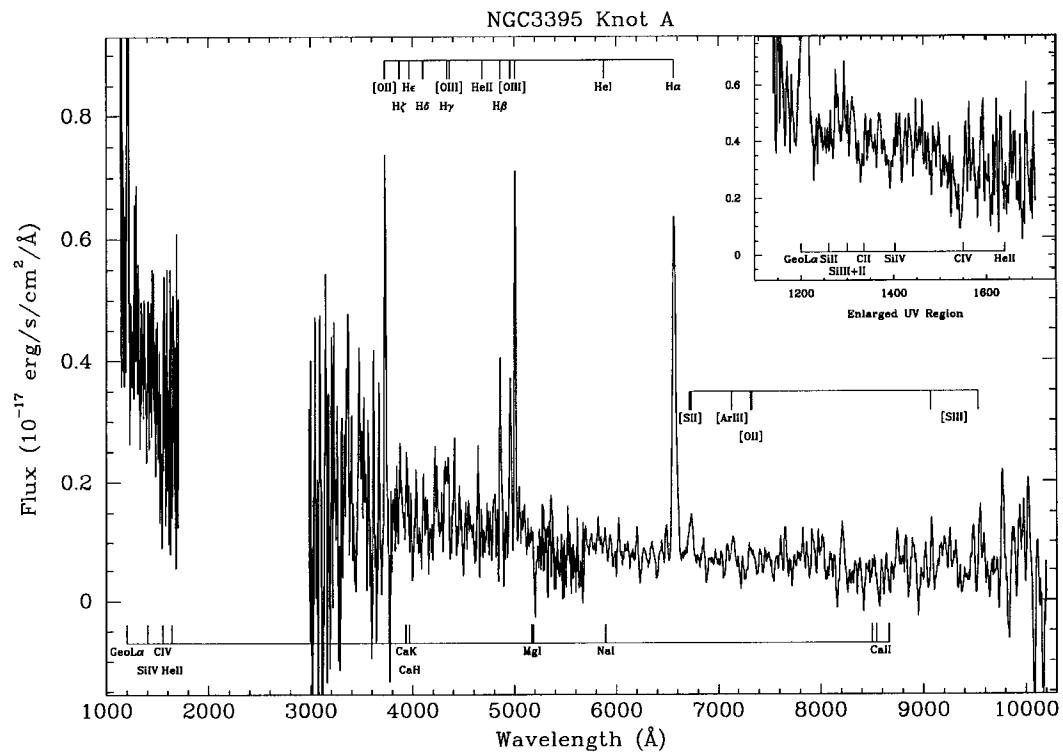
Figure 3k. NGC 3395 Knot A
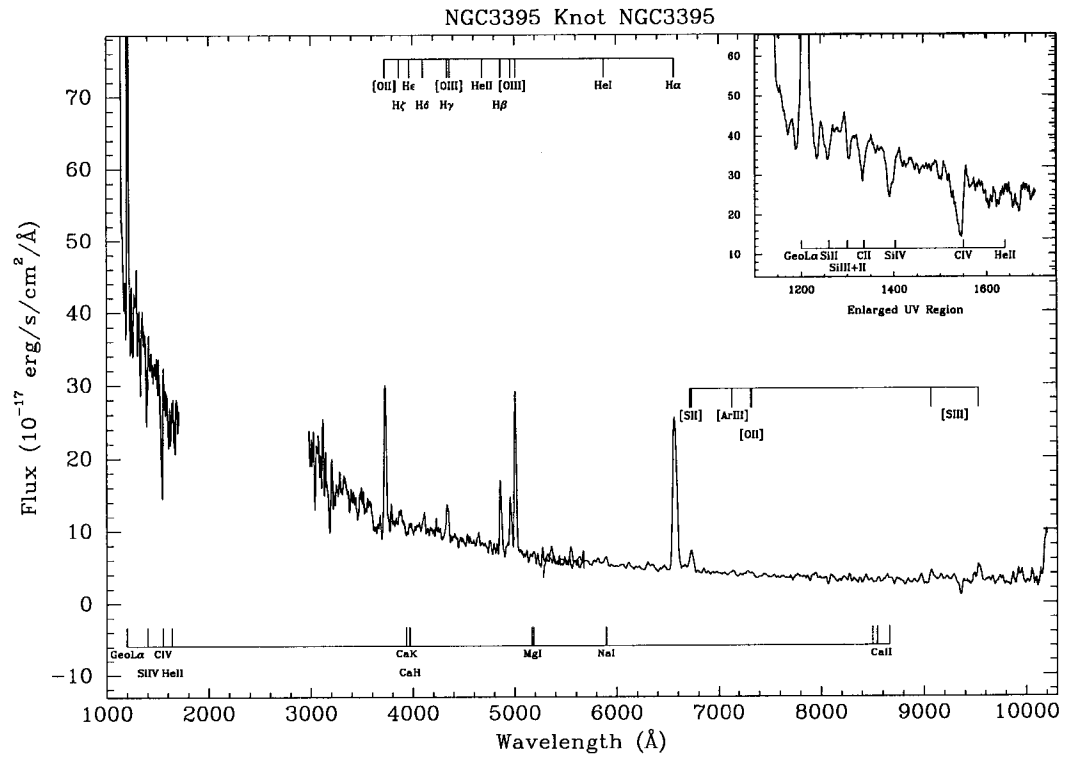
Figure 31. NGC 3395 unresolved Knot

NGC 3396 Measurement Knots

The analysis method described above was applied to NGC 3396. Figure 4 shows the spatial flux profile and the knots that were defined from it. In Table IV, column (1) is the name of the knot, which is arbitrary; column (2) is the pixel row coordinates in the STIS FUV MAMA detector with the G140L grating; column (3) is the pixel row coordinates in the STIS CCD detector with the G430L grating; column (4) is the pixel row coordinates in the STIS CCD detector with the G750L grating. Figure 5a-s presents the spectrum for each individual knot.

Table IV. NGC 3396 Measurement Knots

Knot[a]	FUV MAMA GL 140[b]	CCD GL430[b]	CCD GL 750[b]
S3	440-445	524-526	524-526
S1	446-471	527-539	527-539
S2	472-482	540-544	540-544
S10	483-510	545-557	545-557
R	511-524	558-564	558-564
R10	525-536	565-570	565-570
R20	537-555	571-579	571-579
Q3	556-575	580-588	580-588
Q2	576-588	589-595	589-595
Q1	589-605	596-604	596-604
Q30	606-616	605-608	605-608
Q20	617-656	609-628	609-628
Q10	657-674	629-637	629-637
P2	675-700	638-649	638-649
P	712-728	655-662	655-662
O	729-745	663-670	663-670
N	746-770	671-683	671-683
M	787-797	691-696	691-696
NGC 3396	100-1100	360-842	360-842

[a] Knot names are arbitrary.
[b] Locations are the STIS rows of interest in detector pixel coordinates
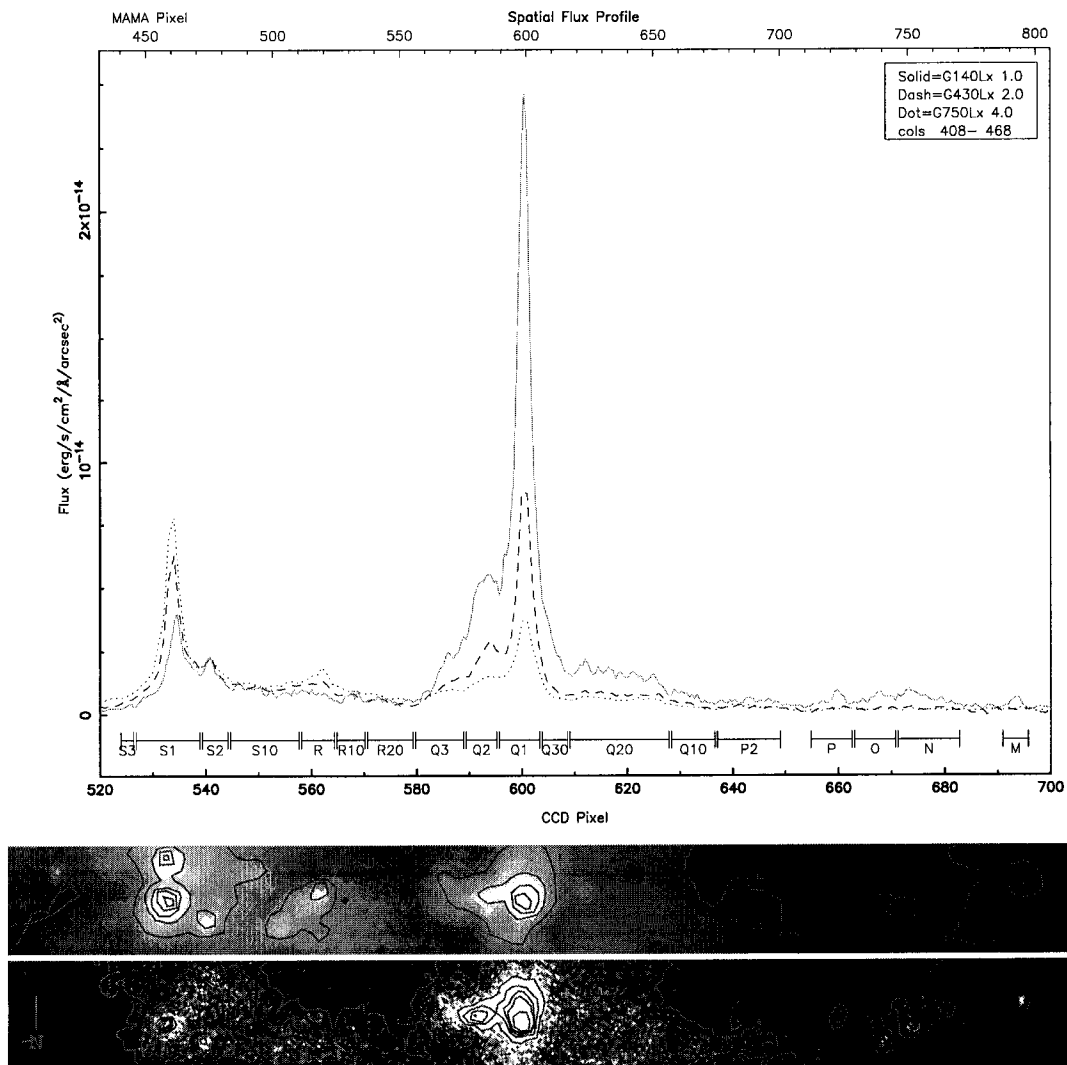
Figure 4. NGC 3396 Spatial Flux Profile

In the top panel, the solid line is the G140L spectra, the dashed is G430L and the dotted is G750L. The legend box provides dispersion columns averaged and the scale factor applied to each detector. The knot names are depicted above the horizontal axis (note: in the interest of clarity, the image is zoomed in on the most interesting section and not all of the knots are shown). The middle panel shows the STIS visible image for the slit region and the bottom panel shows the FUV image of the slit region from Hancock et al. (2003). Intensity contours have been drawn on the images to enhance clarity. Note these images are for illustration purposes only: there are small errors in the relative alignment and scaling between the three panes.

Figure 5a. NGC 3396 Knot S3

Figure 5a-s. NGC 3396 measurement knots. Each figure has been blueshifted by a velocity of 1625 km/s (NASA/IPAC Extragalactic Database) to the rest frame and boxcar smoothed by 5 pixels. Across the top/bottom of the figure, the rest wavelength of several emission/absorption lines is denoted. Geo Lyα stands for geocoronal Lyman α. There is a break between approximately 1700-2800 Å where no data were taken. The names of the knots were assigned somewhat arbitrarily, so the figures are not presented alphabetically, but rather based on spatial slit position, from the top of the detector to the bottom except for the unresolved knot which is presented last.
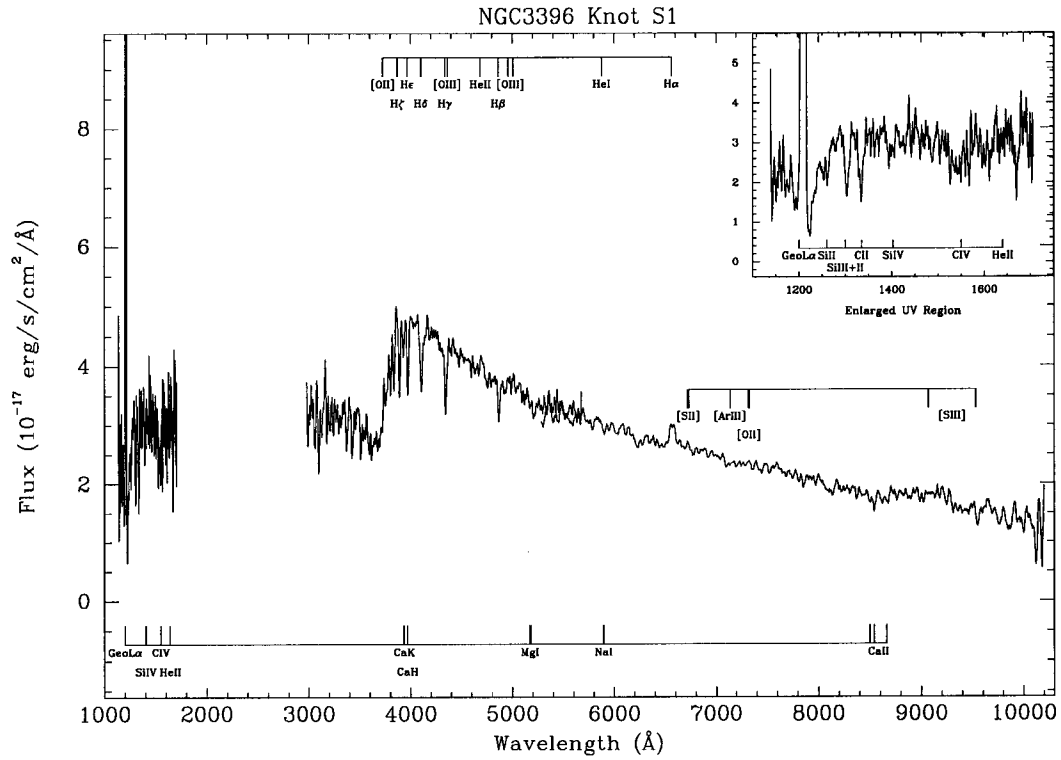
Figure 5b. NGC 3396 Knot S1
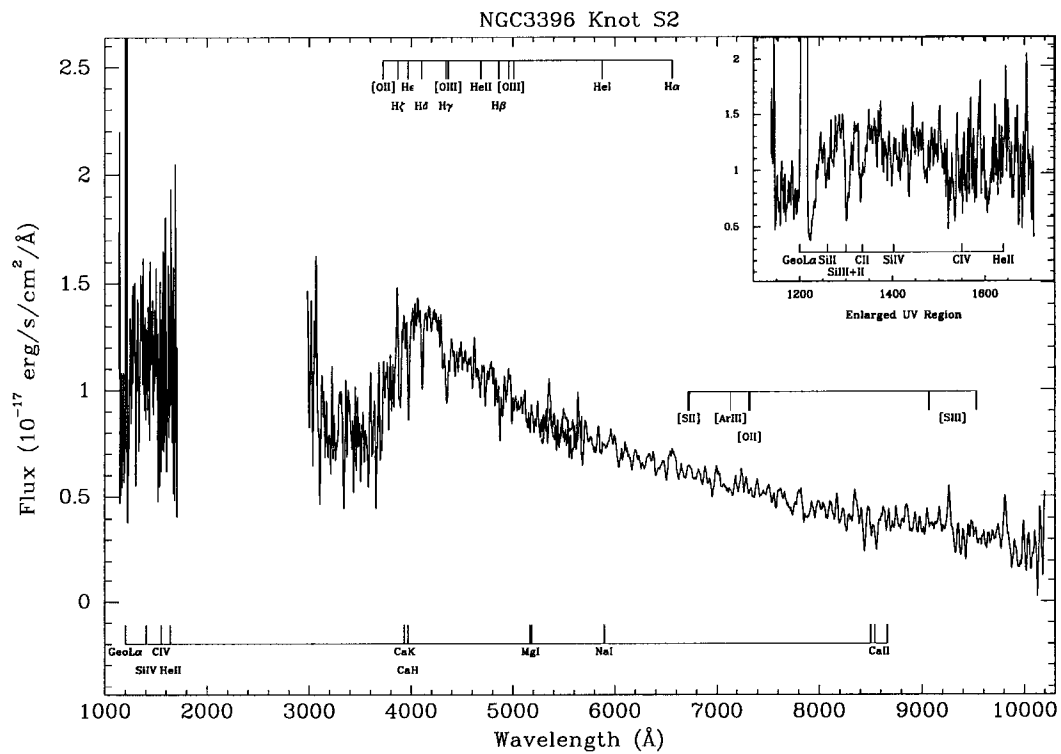
Figure 5c. NGC 3396 Knot S2
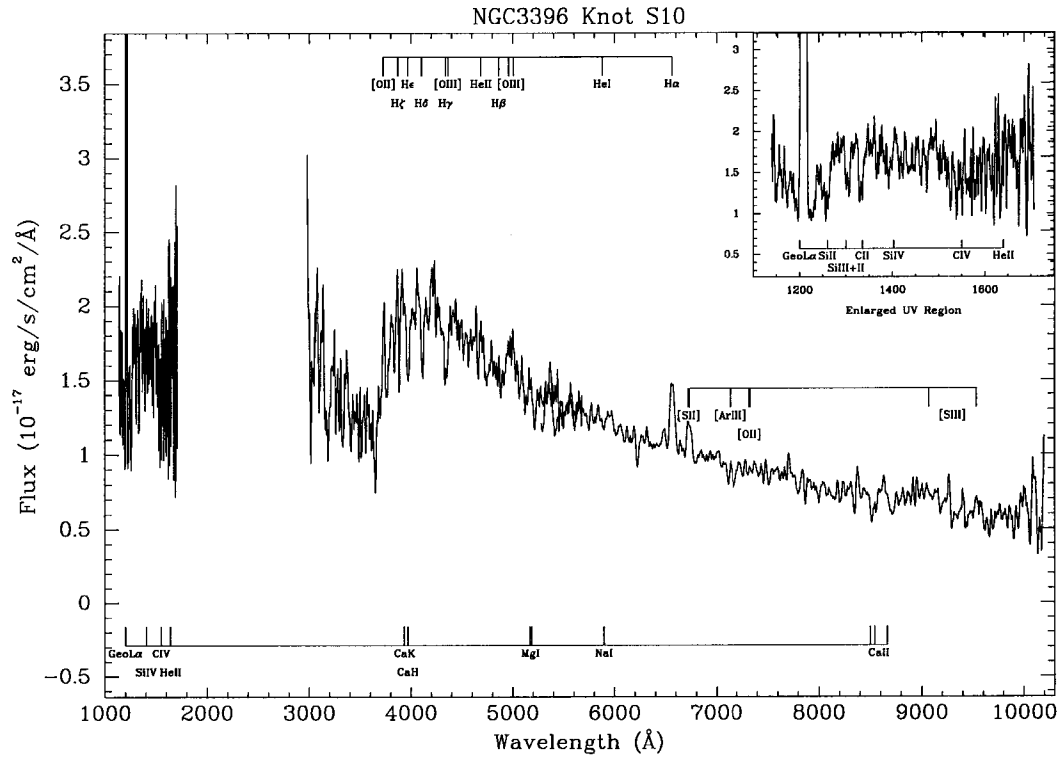
NGC3396 Knot S10

Figure 5d. NGC 3396 Knot S10
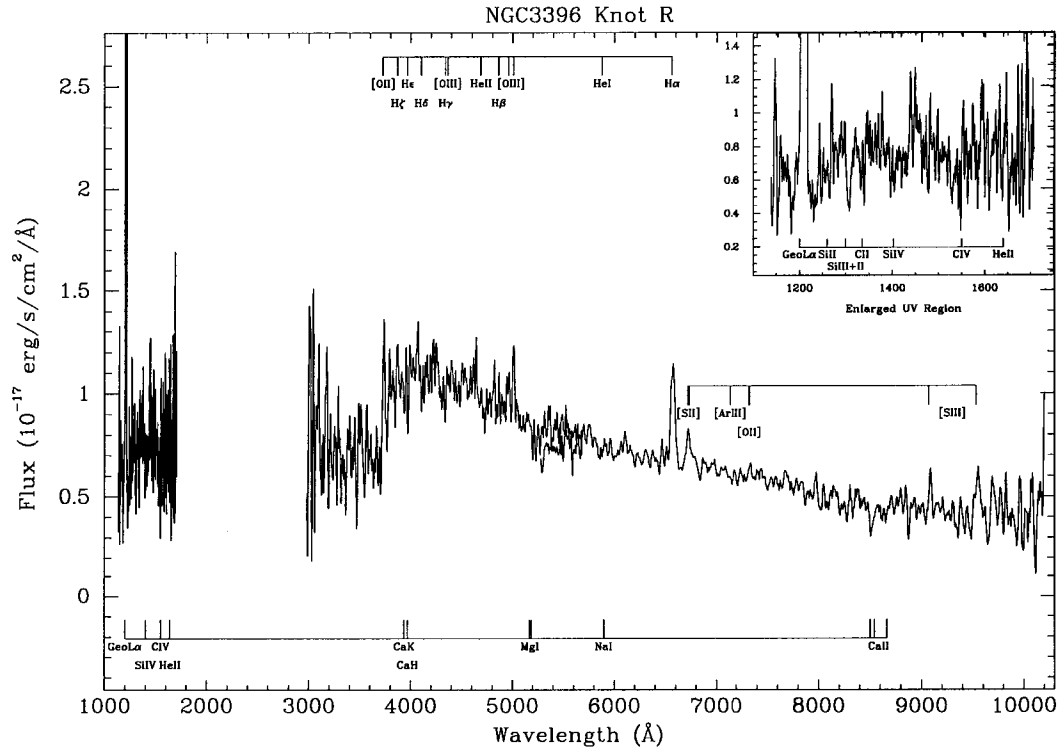
NGC3396 Knot R

Figure 5e. NGC 3396 Knot R
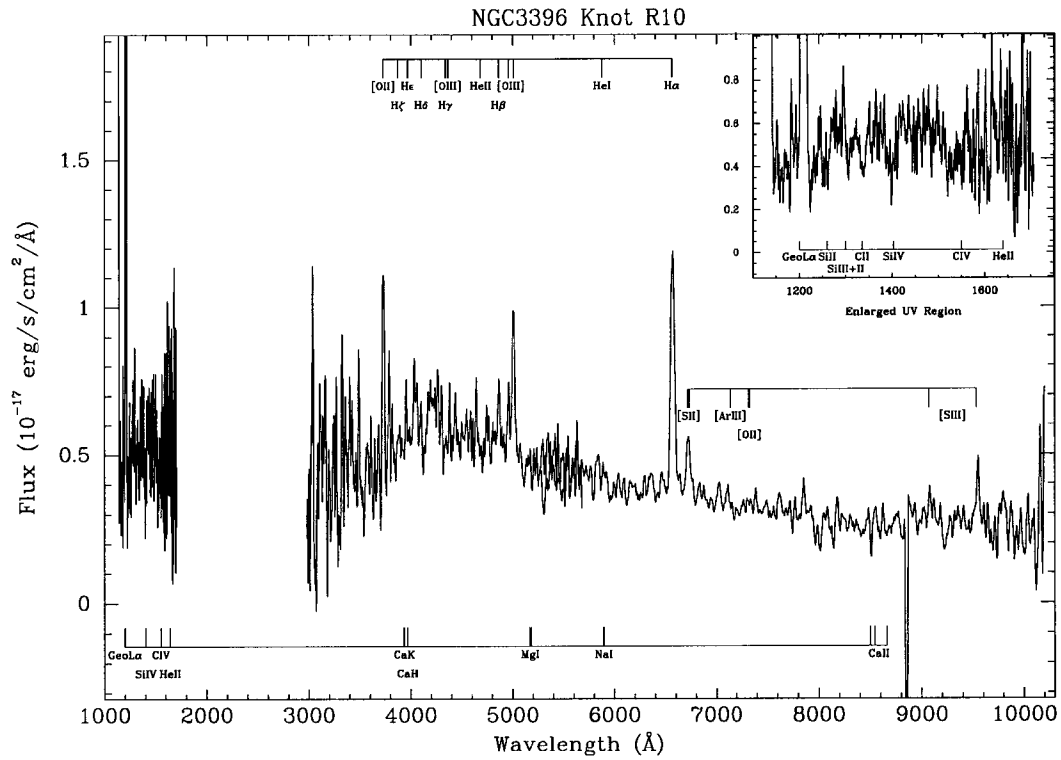
Figure 5f. NGC 3396 Knot R10
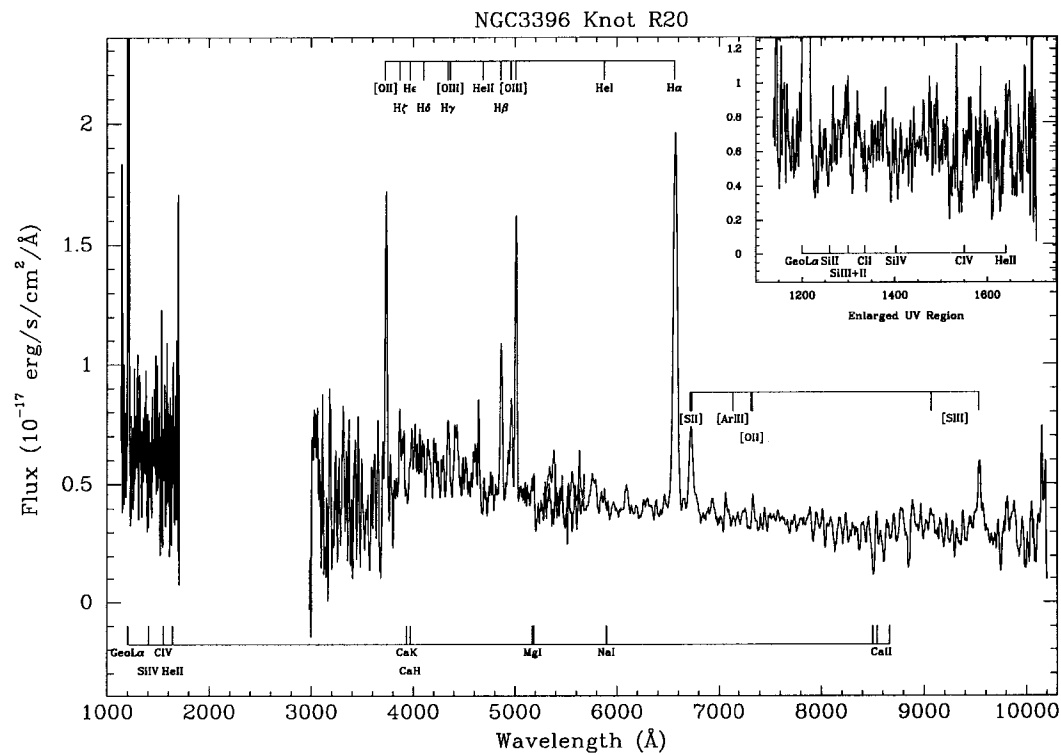
Figure 5g. NGC 3396 Knot R20
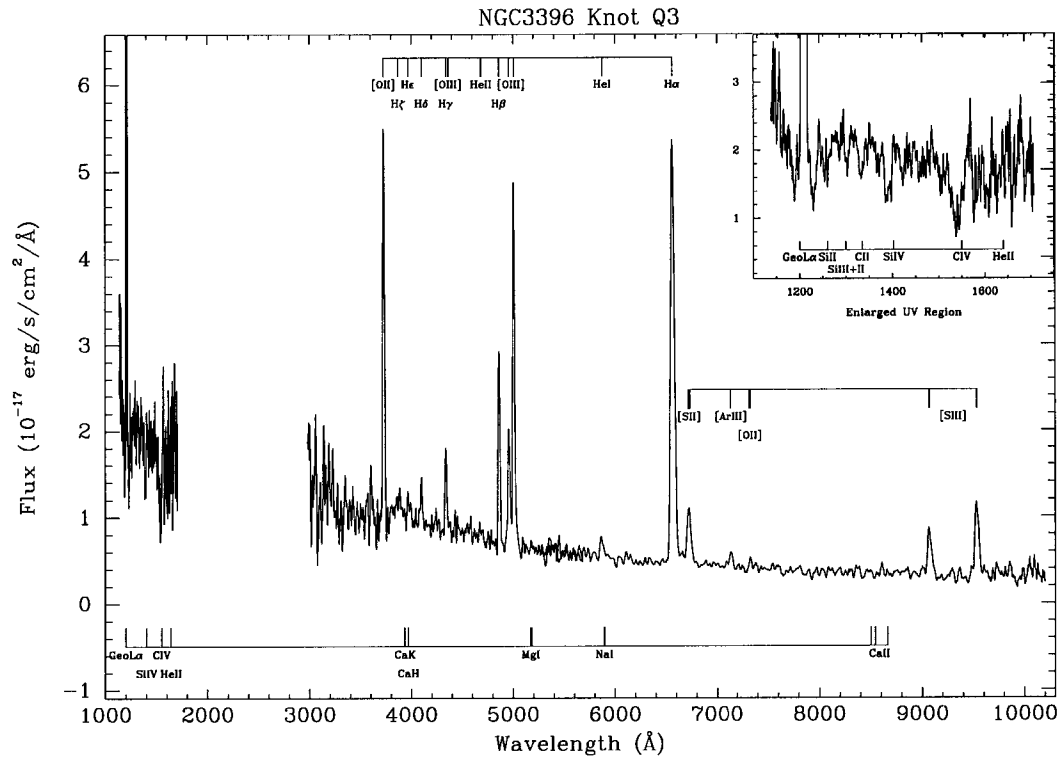
Figure 5h. NGC3396 Knot Q3
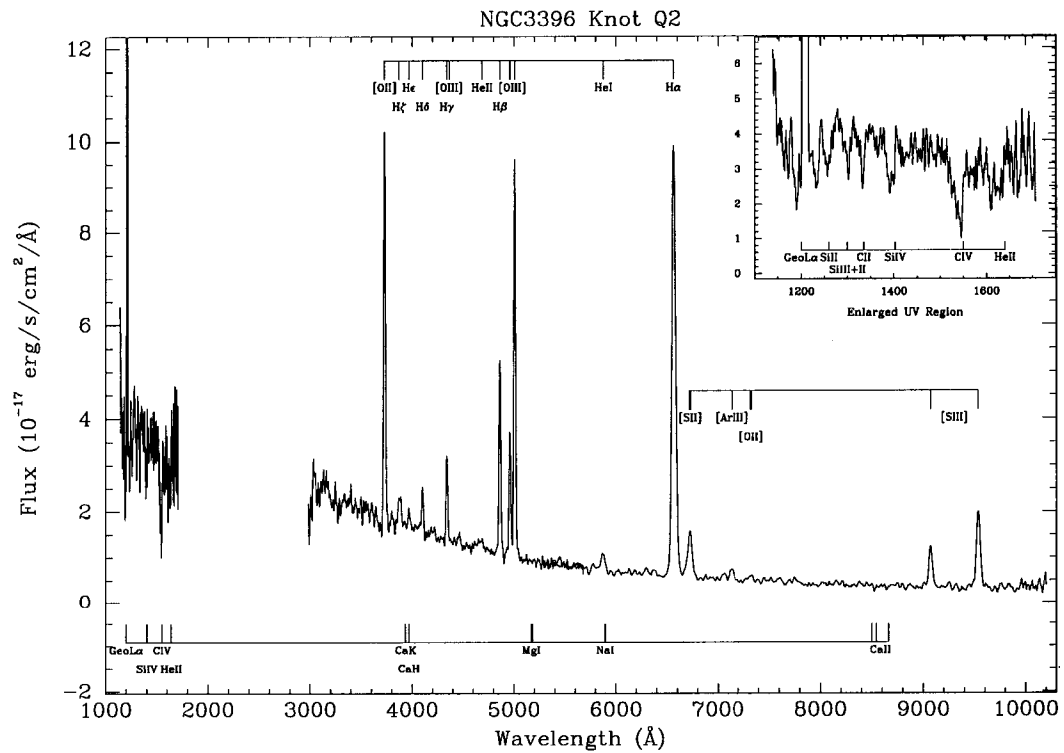
Figure 5i. NGC 3396 Knot Q2
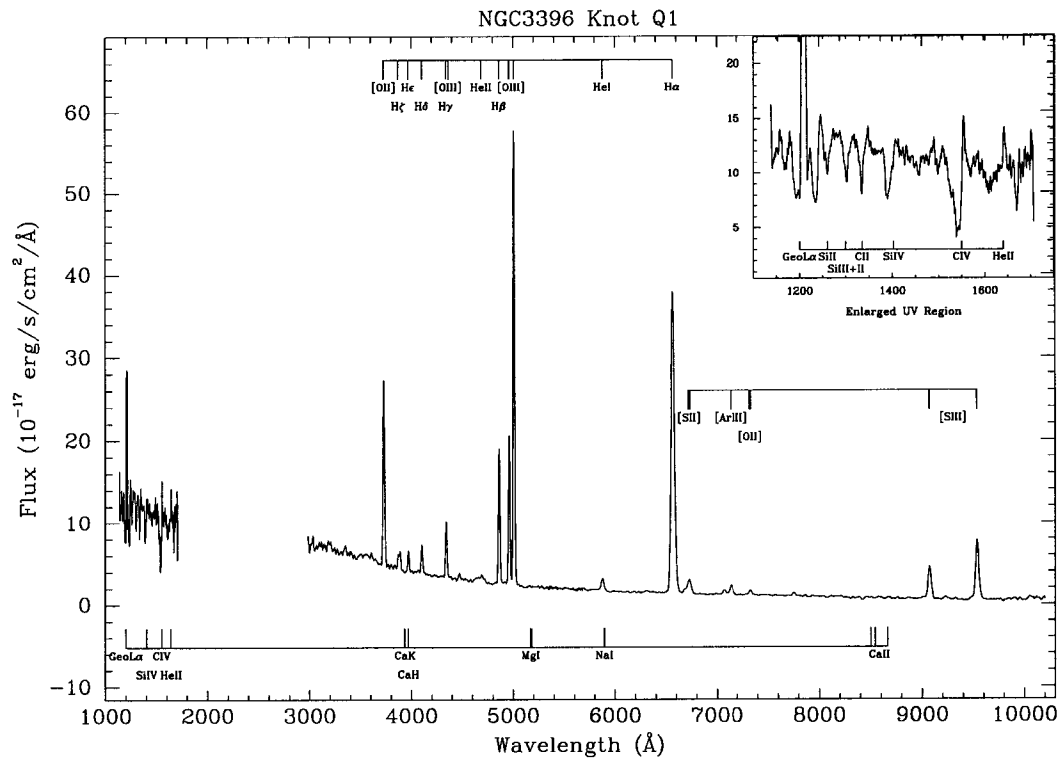
Figure 5j. NGC3396 Knot Q1
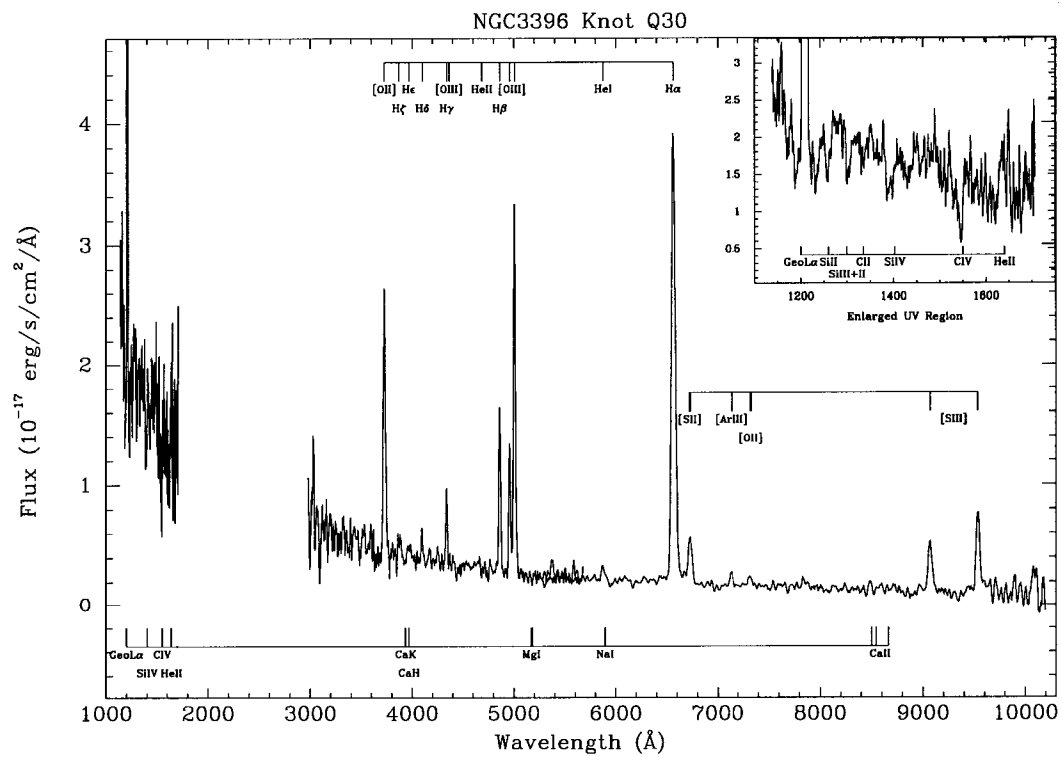
Figure 5k. NGC 3396 Knot Q30
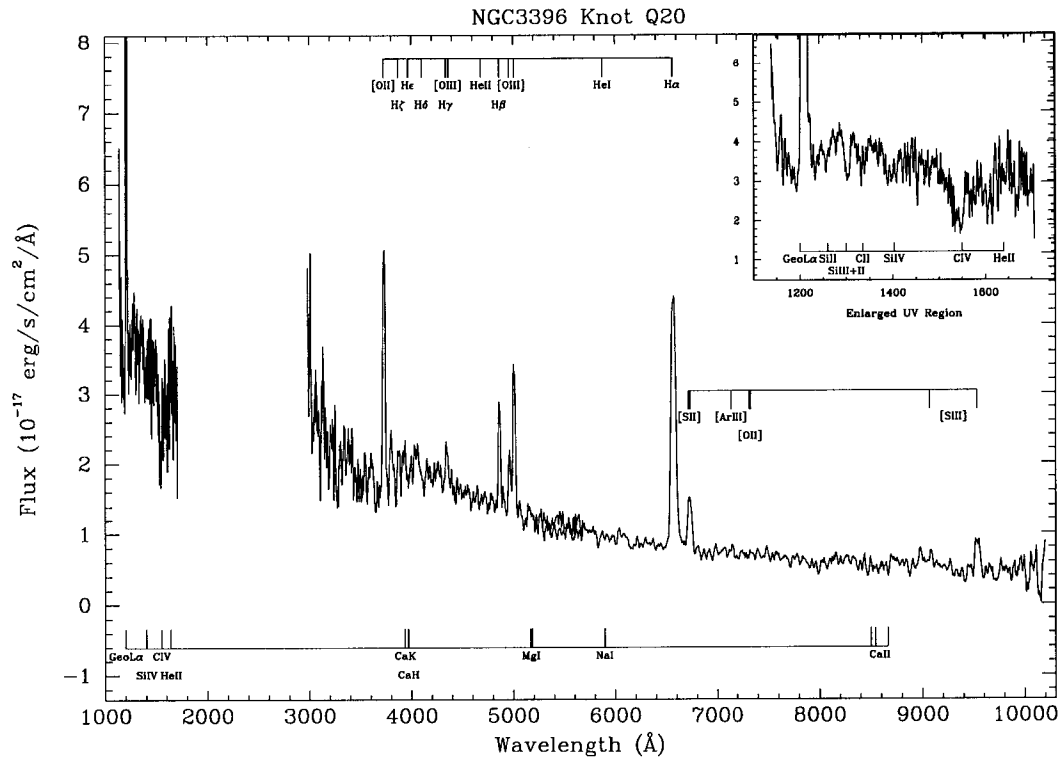
NGC3396 Knot Q20

Figure 5l. NGC 3396 Knot Q20
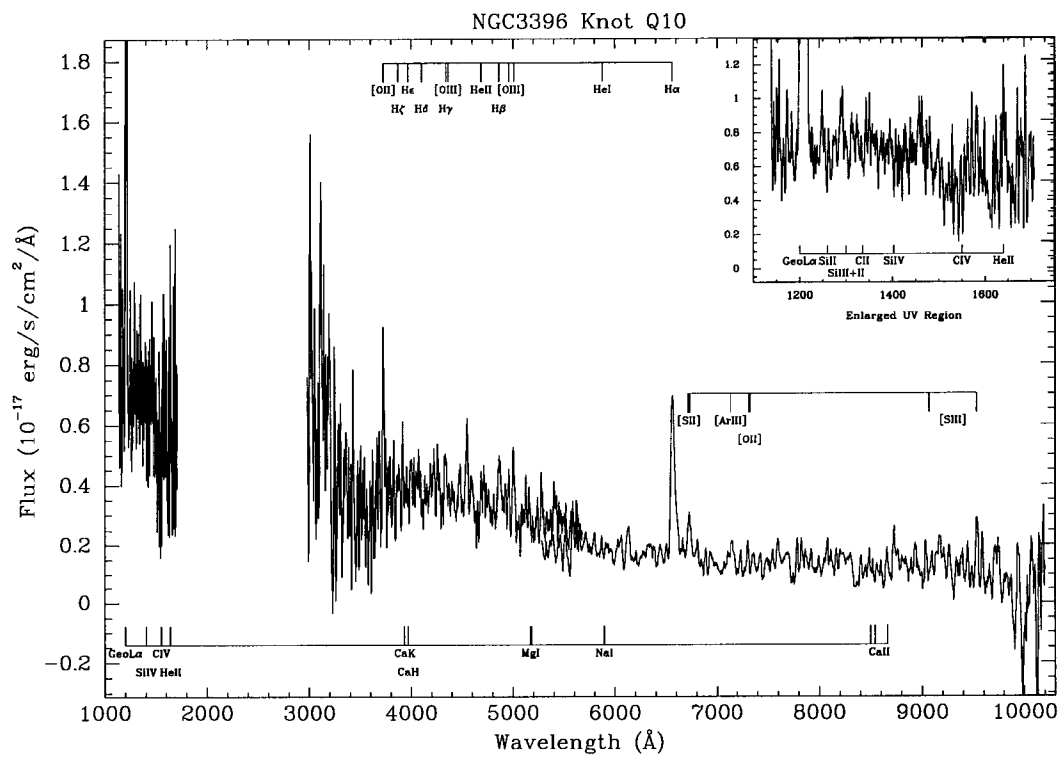
NGC3396 Knot Q10

Figure 5m. NGC 3396 Knot Q10
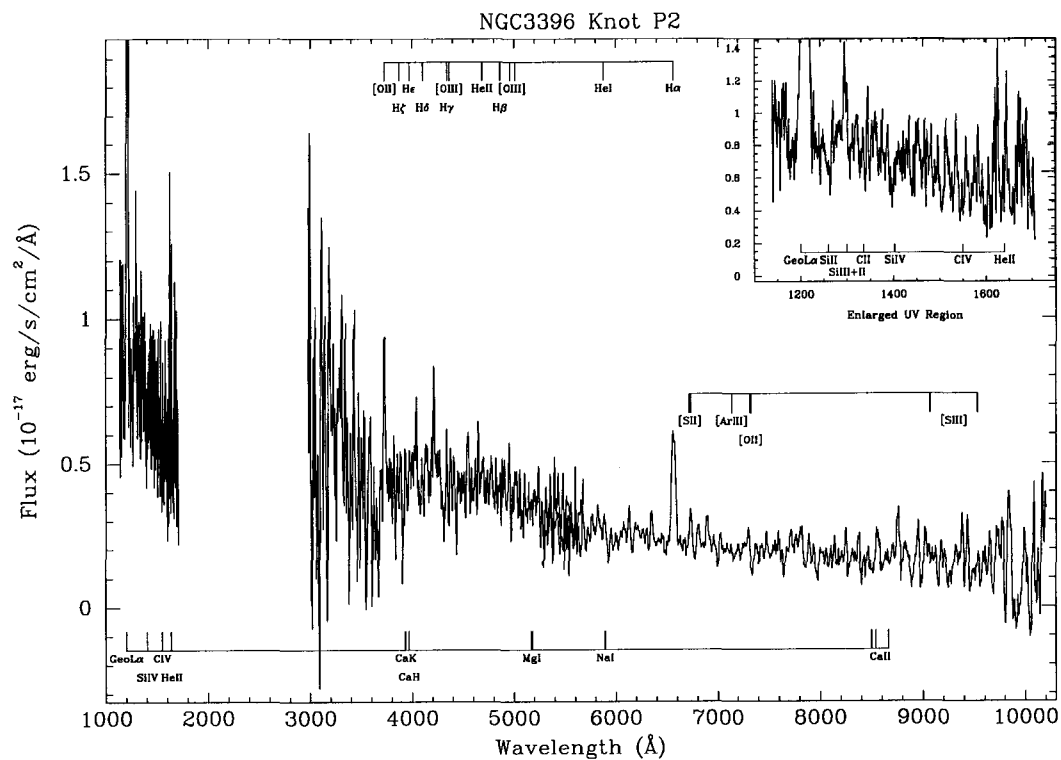
NGC3396 Knot P2

Figure 5n. NGC 3396 Knot P2
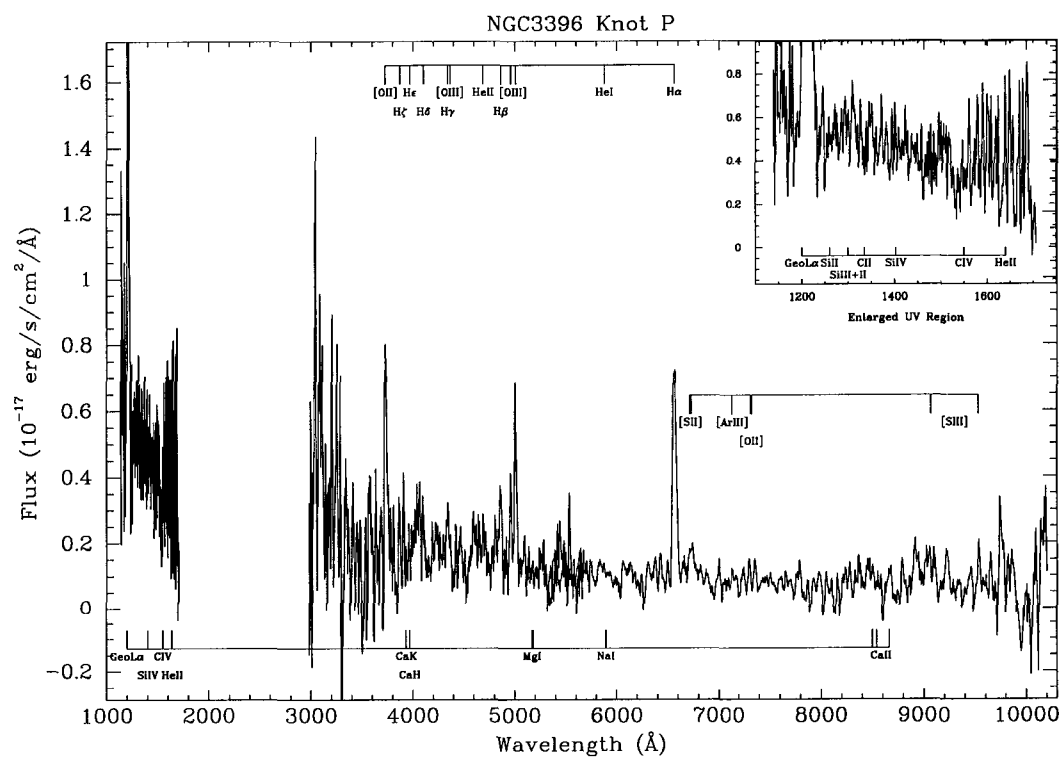
NGC3396 Knot P

Figure 5o. NGC 3396 Knot P
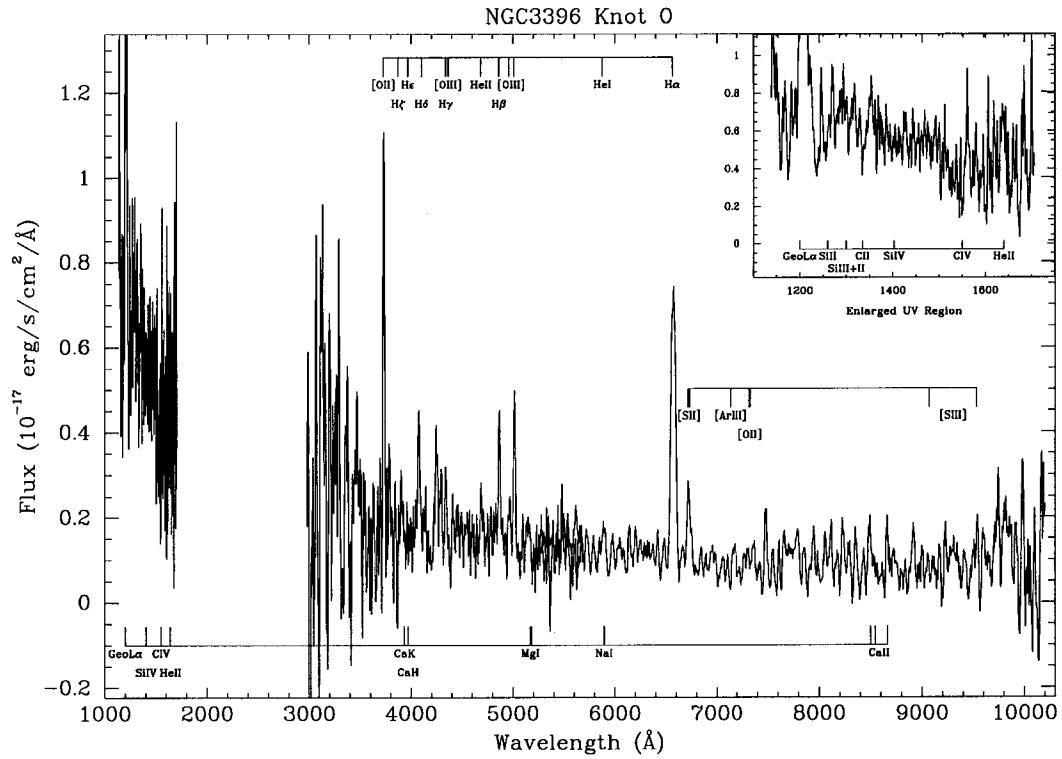
Figure 5p. NGC 3396 Knot O
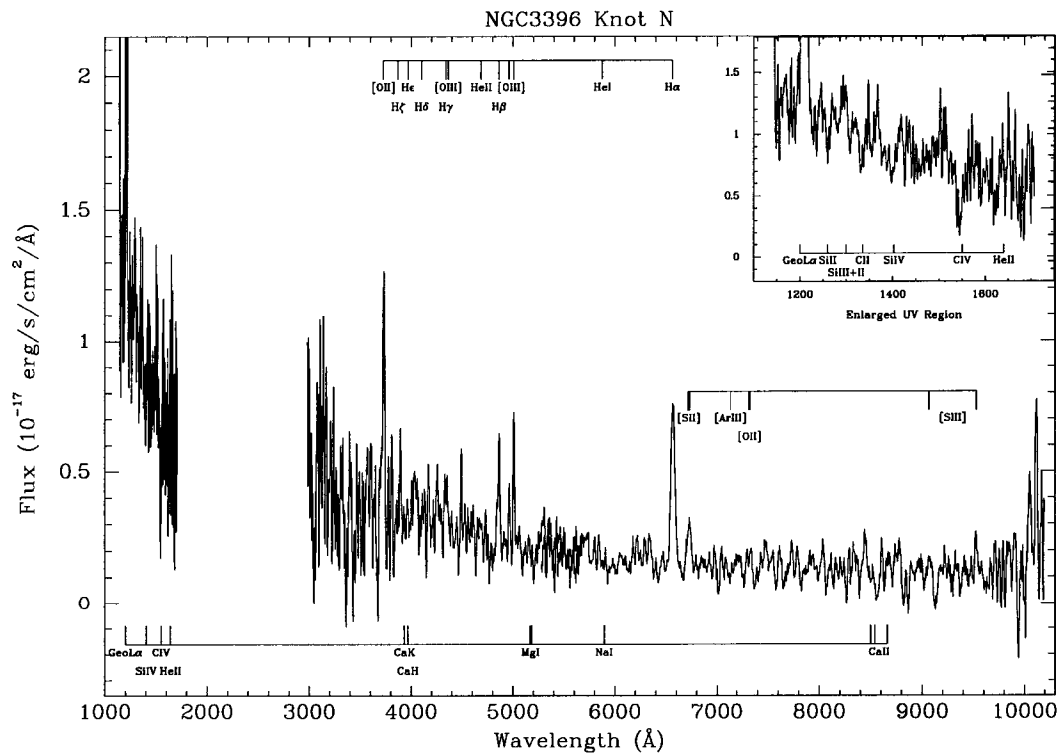
Figure 5q. NGC 3396 Knot N
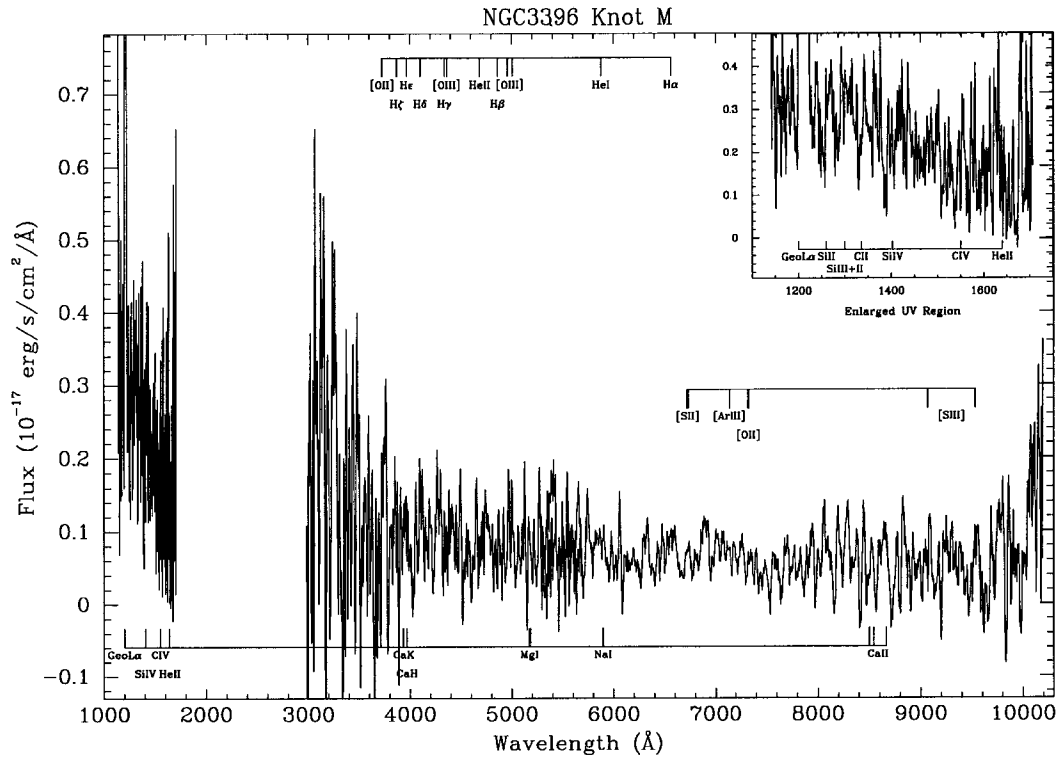
NGC3396 Knot M

Figure 5r. NGC 3396 Knot M

NGC3396 Knot NGC3396
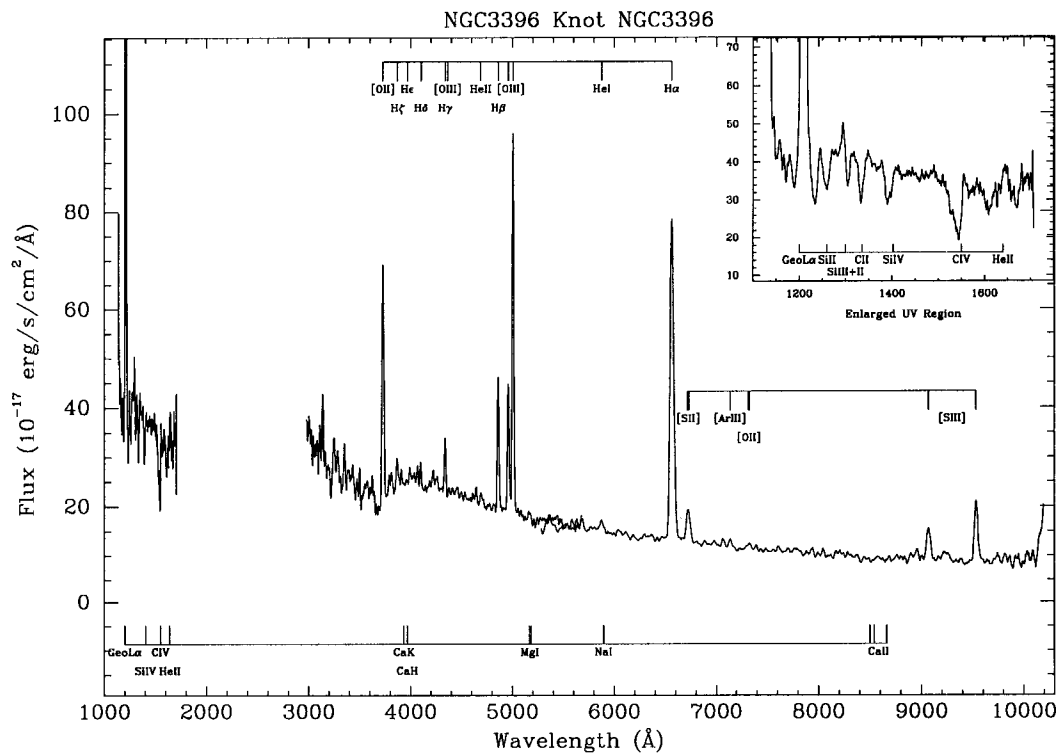
Figure 5s. NGC 3396 unresolved Knot

CHAPTER 5

DATA ANALYSIS AND RESULTS

One of the primary tools that will be used to determine the metallicity of the knots is analysis of emission line strengths. Therefore it is important to accurately measure these lines and quantify the error in their flux. This section will detail the steps performed in measuring the emission line strengths.

Line Strength Measurements

Each knot is a group of rows in the CCD or MAMA detector. The first step in line measurement was to convert the two-dimensional knot spectra into one-dimensional spectra in order to ease analysis, to increase signal-to-noise ratio (SNR), and to derive meaningful information about the knot as a whole. Each two-dimensional knot was reduced to a one-dimensional spectrum by summing the pixels for each column into a single pixel. The column pixel errors were added in quadrature.

Lines strengths were measured from the one-dimensional spectra using a custom software package written by Dr. Charles Nelson and subsequently modified by the author. For each emission line of interest, for example $H\alpha$, the rest wavelength was redshifted by 1625 km/s, which is the proper value for these galaxies (NASA/IPAC Extragalactic Database), and a marker was placed at the appropriate wavelength. Then a user selectable portion of the spectrum was plotted in the neighborhood of the

45

wavelength of interest. We then linearly modeled the continuum as follows. We graphically selected two small continuum regions, one redward and one blueward of the emission region. In each continuum region, we came up with an average flux value and then we connected the red and the blue continuum average values by a line. We took care to ensure that the continuum regions were close enough to model well the continuum at the emission by a line. We then graphically delineated the extent of the line profile above the continuum fit and the continuum subtracted line strength was numerically integrated. The pipeline photometric calibration assumes a continuum source uniformly illuminating the slit. For an emission line source, the dispersion direction is no longer uniformly illuminated, therefore the photometry must be scaled by the header parameter CONT2EML which is the slit width expressed in Angstroms. It is very important to stress that when one uses CONT2EML, it includes the dispersion; therefore to calculate the total flux in an emission line one must calculate only CONT2EML $*$ Σ(pixels) and not calculate the integral of the energy = Σ(pixels $*$ dispersion). Failure to take this into account will result in double counting the dispersion and will yield erroneous measurements. The continuum fit error and the line flux error were added in quadrature.

Absorption was measured in a similar fashion, and used the same graphical continuum fitting technique. We will use our measured equivalent widths in the Storchi-Bergmann metallicity estimation techniques (described later in the section on metallicity), so we measured the emission lines using the Storchi-Bergmann defined wavelength intervals. Absorption was not scaled by CONT2EML since it is not appropriate.

Deblending Hα and [NII]

We chose to observe using the 0.5 arcsecond wide slit in order to obtain adequate SNR in the UV region of the spectrum. Unfortunately in the far red portion of the spectrum the width of the slit used and the extended nature of the target can result in a full width at half maximum (FWHM) of a line profile as great as 50 Å (STIS Handbook). This is of concern because Hα λ6563 is required to correct the measured line strengths for dust reddening, but Hα λ6563 and [N II] λλ6548, 6583 were totally blended in our data. We attempted to deblend Hα and [N II], but they were too blended to yield credible results. Therefore, for all our analysis, we measured the entire flux of Hα + [N II] emission and assigned it to Hα only. Depending on the strength of the [O III] λ5007/Hβ emission, this could lead to errors as great as 40% in the measured Hα flux (Osterbrock, 1989). We typically measure [O III] λ5007/Hβ ~ 2.5 in our knots which is consistent with up to a 40% error. When we deredden the emission lines we will assign a systematic 40% Hα flux error and add it in quadrature with the measurement errors. We will discuss the impact of this later, in the reddening section.

Correction for Stellar Absorption

It has been shown by Shields and Searle (1978) and McCall et. al (1985) that when observing combined stellar and H II region spectra, the stellar atmospheres provide an underlying absorption in the H II region Balmer series emission. To account for this, the references above correct the Balmer hydrogen emission lines for this underlying absorption by adding 2 Å of continuum flux to the measured emission. We therefore do the same.

Correction for Reddening

Photons suffer extinction due to the effects of interstellar dust. Strong dust extinction is expected in and around the H II region itself. Calzetti et al. (1994) conducted an extensive survey of extinction in starburst galaxies and have published an extinction law appropriate for the UV and optical region. This extinction law has a slope that is more gray than standard Milky Way law and does not exhibit the characteristic 2175 Å feature. The emission line strengths were referenced to Hβ as is standard and the line ratio of I_λ/I_β were dereddened according to the formula

$$\frac{I_\lambda^o}{I_\beta^o} = \frac{I_\lambda}{I_\beta} e^{\left[\tau(\lambda) - \tau(\beta)\right]} = \frac{I_\lambda}{I_\beta} e^{\tau_\beta^l \left[Q_e(\lambda) - Q_e(\beta)\right]} \tag{2}$$

where

$$\tau_\beta^l = -\frac{\ln\left(\dfrac{I_\alpha/I_\beta}{2.88}\right)}{Q_e(\alpha) - Q_e(\beta)} \tag{3}$$

The I's are line intensities, the superscript '0' denotes unreddened source intensity, the subscripts α, β, λ denote the Hα, Hβ, or the emission line of interest and Q_e is as given in Calzetti et al. (1994). The value 2.88 in the definition of τ_β^l is the theoretical unreddened value of I_α^o/I_β^o which we assume at the source.

As mentioned previously, we were unable to deblend Hα and [N II] which could cause us to overestimate Hα by as much as 40%. This will cause us to overestimate τ_β^l which in turn will cause us to overestimate the reddening of the emission lines. We therefore add a 40% systematic flux error in quadrature to the Hα measurement error in

determining the lower error limit in the Balmer optical depth, τ^l_β, and propagate this error

in our reddening. For the upper error limit we assign the 1 sigma measurement error.

Fortunately, since the error in Hα only enters in the natural log, large errors in Hα do not

cause objectionably large errors in the dereddened line flux. The only exception is the

dereddened value of Hα itself, since the error enters directly into the ratio Hα/Hβ in this

case.

We also attempted to correct for reddening using the optical depth calculated from

Hγ/Hβ to assess the impact of our inability to deblend Hα and [N $_{II}$]. All the mathematics

are the same, except we replace 2.88 in formula 3 with 0.469, the theoretical unreddened

ratio of Hγ/Hβ.

The results are presented in Tables V and VI where column (1) is the knot name;

column (2) is the Balmer optical depth calculated from Hα/Hβ; column (3) is the Balmer

optical depth calculated from Hγ/Hβ; and column (4) is the color excess calculated from

Hα/Hβ from emission lines. When we were unable to calculate a value due to the lack of

a required emission line, we enter "n/a" for not available. The lower error estimates for

$\tau^l_{\beta, H\alpha/H\beta}$ and E(B-V) include the up to 40% error in Hα due to our inability to deblend Hα

and [N $_{II}$]. We present 1 sigma errors for $\tau^l_{\beta, H\gamma/H\beta}$ and the upper error estimates for $\tau^l_{\beta, H\alpha/H\beta}$

and E(B-V).

As can be seen, the optical depth from Hγ/Hβ is frequently negative, which would

imply the physically impossible amplification of photons at all wavelengths rather than

attenuation. Therefore the optical depth from Hγ/Hβ is inferior to the optical depth from

Hα/Hβ, even considering the large errors in Hα. Therefore, we use the Balmer optical depth calculated from for Hα/Hβ all further analyses.

Calzetti et al. (1994), among others, has noted that the color excess calculated from emission lines is typically double the value calculated from the color excess calculated from the continuum. Therefore our emission line color excess values of 0.1-0.8 correspond to values calculated from the continuum of 0.05-0.4. These values are in good agreement with the values found by Hancock et al. (2003) and Bachilla (2003)

Table V. NGC 3395 Reddening Coefficients

Region	$\tau^l_{\beta,H\alpha/H\beta}$	$\tau^l_{\beta, H\gamma/H\beta}$	$E(B-V)_{H\alpha/H\beta}$
D	n/a	n/a	n/a
C80	0.86 +0.21 -0.85	-2.38 ±0.97	0.35 +0.09 -0.35
C70	0.50 +0.09 -0.83	1.08 ±0.68	0.21 +0.04 -0.34
C60	0.43 +0.16 -0.84	0.03 ±0.62	0.18 +0.06 -0.35
C1	0.64 +0.16 -0.84	0.17 ±0.81	0.27 +0.07 -0.35
C2	0.40 +0.07 -0.83	0.65 ±0.50	0.16 +0.03 -0.34
C3	0.50 +0.05 -0.83	-0.14 ±0.34	0.21 +0.02 -0.34
C4	0.44 +0.07 -0.83	0.02 ±0.37	0.18 +0.03 -0.34
C50	0.82 +0.10 -0.83	-0.44 ±0.45	0.34 +0.04 -0.34
B	1.22 +0.51 -0.97	-2.98 ±1.70	0.50 +0.21 -0.40
A	1.16 +0.51 -0.97	-1.31 ±2.61	0.48 +0.21 -0.40
NGC 3395	0.84 +0.11 -0.83	-2.12 ±0.54	0.35 +0.04 -0.34

Table VI. NGC 3396 Reddening Coefficients

Region	$\tau^{l}_{\beta,H\alpha/H\beta}$	$\tau^{l}_{\beta,H\beta/H\gamma}$	$E(B-V)_{H\alpha/H\beta}$
S3	n/a	n/a	n/a
S1	n/a	n/a	n/a
S2	n/a	n/a	n/a
S10	n/a	n/a	n/a
R	n/a	n/a	n/a
R10	1.90+0.26 -0.87	n/a	0.78+0.11 -0.36
R20	0.96+0.13 -0.84	n/a	0.40+0.05 -0.34
Q3	0.97+0.05 -0.83	0.75±0.30	0.40+0.02 -0.34
Q2	0.96+0.03 -0.83	0.98±0.18	0.40+0.01 -0.34
Q1	0.94+0.01 -0.83	0.51±0.08	0.39+0.01 -0.34
Q30	1.45+0.06 -0.83	0.84±0.33	0.60+0.03 -0.34
Q20	1.38+0.10 -0.83	1.49±0.66	0.57+0.04 -0.34
Q10	1.00+0.42 -0.93	n/a	0.41+0.17 -0.38
P2	n/a	n/a	n/a
P	1.05+0.34 -0.89	n/a	0.43+0.14 -0.37
O	1.17+0.27 -0.87	-0.47±1.43	0.48+0.11 -0.36
N	-0.31+0.28 -0.87	n/a	-0.13+0.11 -0.36
M	n/a	n/a	n/a
NGC 3396	1.23+0.03 -0.83	1.91±0.20	0.50+0.01 -0.34

Results

Following the procedures outlined above, the emission and absorption lines in Table

VII were measured (when present) for each knot in both galaxies. Columns (1) and (3)

are the rest wavelengths in Angstroms and columns (2) and (4) are the atomic lines associated with those wavelengths respectively.

The measured emission lines are presented in Tables VIII and X where each emission line is presented relative to Hβ, except Hα and Hβ itself which are presented in units of 10^{-16} erg s^{-1} cm^{-2} Å^{-1}. Errors presented are one sigma errors associated with the flux ratio except for Hα and Hβ which are the 1 sigma errors in the flux itself. Tables IX and XI give the equivalent widths of both the absorption lines (positive value) and the emissions lines (negative value) in Angstroms. Errors presented are measurement errors associated with the equivalent width.

Table VII. Measured Emission and Absorption Lines

Rest wavelength (Å)	Name	Rest wavelength (Å)	Name
1403 (1380-1415)[a]	Si IV	4861[b]	Hβ
1550 (1523-1576)[a]	C IV	4959[b]	[O III]
1640[b]	He II	5007[b]	[O III]
3727[b]	[O II]	5876[b]	He I
3869[b]	[Ne III]	6563[b,e]	Hα
3889[c]	Hζ	6718 + 6732[b]	[S II]
3969[c]	Hε	7136[b]	[Ar III]
4102[c]	Hδ	9069[b]	[S III]
4340[c]	Hγ	9531[b]	[S III]
4686 (4600-4700)[d]	He II (WR Bump)		

[a] Region was always in absorption when measured. In these regions, absorption was defined as the difference between the fit continuum and the data over a range of wavelengths denoted by the parentheses. The wavelength range is chosen to correspond with the measurement windows defined by Storchi-Bergmann, Calzetti, and Kinney (1994).

[b] Region always in emission

[c] Region measured in emission in some knots, in absorption in others

[d] Region always measured in emission. Wavelength range from Kunith & Joubert (1985)

[e] Line flux includes [N II] λλ6548,6583 since unable to deblend

Table VIII NGC 3395 Dereddened Emission Line Fluxes

Knot	He II λ1640 (/Hβ)	[O II] λ3727 (/Hβ)	[Ne III] λ3869 (/Hβ)	Hζ λ3889 (/Hβ)	Hε λ3969 (/Hβ)	Hδ λ4102 (/Hβ)	Hγ λ4340 (/Hβ)	He II λ4686 (/Hβ)	Hβ λ4861 (see a)	[O III] λ4959 (/Hβ)	[O III] λ5007 (/Hβ)	He I λ5876 (/Hβ)	Hα λ6563 (see a)	[S II] λ6718, λ6732 (/Hβ)	[Ar III] λ7136 (/Hβ)	[S III] λ9069 (/Hβ)	[S III] λ9531 (/Hβ)
D	--	--	--	--	--	--	--	--	--	--	--	--	22.43 ±1.23	--	--	--	--
C80	--	2.79 ±1.27	--	--	--	--	0.89 ±0.24	--	7.16 ±0.70	0.84 ±0.11	2.42 ±0.26	--	31.21 ±0.92	0.41 ±0.19	--	0.17 ±0.14	--
C70	0.31 ±0.52	2.17 ±0.88	0.18 ±0.09	0.26 ±0.12	0.15 ±0.08	0.16 ±0.07	0.42 ±0.09	0.04 ±0.06	21.10 ±0.85	0.66 ±0.05	2.14 ±0.13	0.11 ±0.05	77.34 ±1.19	0.25 ±0.11	0.10 ±0.06	0.10 ±0.08	0.27 ±0.22
C60	--	1.77 ±0.77	--	--	0.17 ±0.08	0.14 ±0.08	0.51 ±0.11	0.25 ±0.11	9.30 ±0.65	1.14 ±0.11	2.16 ±0.18	--	33.00 ±0.94	0.33 ±0.15	0.14 ±0.08	0.17 ±0.15	0.16 ±0.15
C1	1.56 ±2.90	1.48 ±0.66	0.42 ±0.19	--	--	--	0.51 ±0.12	1.00 ±0.17	14.69 ±1.10	1.02 ±0.11	2.53 ±0.21	--	57.78 ±1.56	0.23 ±0.12	--	0.16 ±0.13	0.27 ±0.23
C2	--	1.78 ±0.71	0.19 ±0.07	0.14 ±0.06	--	0.25 ±0.08	0.45 ±0.09	0.16 ±0.05	25.86 ±0.74	1.07 ±0.05	3.00 ±0.15	0.13 ±0.04	90.20 ±1.23	0.15 ±0.07	0.11 ±0.06	0.17 ±0.14	0.28 ±0.23
C3	--	1.91 ±0.76	0.12 ±0.05	--	0.13 ±0.05	0.20 ±0.06	0.53 ±0.10	0.13 ±0.04	42.07 ±0.91	0.85 ±0.04	2.58 ±0.12	0.07 ±0.02	154.17 ±1.59	0.20 ±0.09	0.05 ±0.03	0.19 ±0.14	0.28 ±0.23
C4	--	2.01 ±0.80	0.07 ±0.05	--	0.19 ±0.08	0.23 ±0.08	0.51 ±0.09	0.20 ±0.05	24.96 ±0.78	0.71 ±0.04	2.00 ±0.11	0.15 ±0.05	89.13 ±1.30	0.25 ±0.11	--	0.14 ±0.11	0.27 ±0.23
C50	--	3.31 ±1.35	--	--	--	0.27 ±0.10	0.60 ±0.12	0.06 ±0.07	35.56 ±1.65	0.53 ±0.05	1.71 ±0.11	--	152.06 ±2.32	0.35 ±0.16	--	0.10 ±0.08	0.23 ±0.19
B	--	7.38 ±4.71	--	--	--	--	1.08 ±0.48	--	2.57 ±0.62	0.95 ±0.31	3.31 ±0.79	--	13.32 ±0.67	0.65 ±0.32	--	--	--
A	--	4.69 ±3.05	0.79 ±0.66	0.40 ±0.54	--	0.43 ±0.37	0.76 ±0.45	--	4.78 ±1.14	1.19 ±0.35	2.17 ±0.52	--	24.06 ±1.51	0.36 ±0.19	--	--	--
NGC 3395	1.03 ±1.72	3.07 ±1.25	--	--	0.10 ±0.08	0.29 ±0.11	0.84 ±0.17	0.20 ±0.06	235.14 ±11.91	0.83 ±0.07	2.15 ±0.14	--	1015.93 ±10.85	0.34 ±0.15	0.04 ±0.03	0.11 ±0.08	0.17 ±0.14

a flux (10^{-16} erg s^{-1} cm^{-2} Å^{-1})

Table IX NGC 3395 Equivalent Widths

Knot	Si IV λ1403 (Å)	C IV λ1550 (Å)	He II λ1640 (Å)	[O II] λ3727 (Å)	[Ne III] λ3869 (Å)	Hζ λ3889 (Å)	Hε λ3969 (Å)	Hδ λ4102 (Å)	Hγ λ4340 (Å)	He II λ4686 (Å)	Hβ λ4861 (Å)	[O III] λ4959 (Å)	[O III] λ5007 (Å)	He I λ5876 (Å)	Hα λ6563 (Å)	[S II] λ6718, λ6732 (Å)	[Ar III] λ7136 (Å)	[S III] λ9069 (Å)	[S III] λ9531 (Å)
D	9.28 ±1.89	16.80 ±4.19	-5.83 ±2.72	-57.49± 18.66	---	---	---	---	---	---	---	-8.28 ±3.67	-35.43 ±5.57	---	-85.94 ±4.82	---	---	---	---
C80	8.50 ±1.57	12.36 ±3.08	---	-25.01 ±3.24	---	---	---	---	-21.47 ±3.08	2.33 ±4.73	-25.50 ±2.38	-25.51 ±2.30	-78.94 ±4.21	---	-98.58 ±3.47	-13.25 ±2.49	---	-10.08 ±3.76	---
C70	6.41 ±1.04	16.49 ±1.91	-3.45 ±1.26	-37.24 ±2.14	-3.40 ±1.08	-7.05 ±1.36	-4.95 ±1.39	-5.31 ±1.31	-13.48 ±1.49	-1.09 ±2.16	-40.86 ±1.67	-27.00 ±1.69	-87.97 ±2.21	-3.96 ±1.67	-154.60 ±2.83	-13.25 ±1.98	-5.64 ±2.10	-8.69 ±1.83	-29.71 ±4.18
C60	6.22 ±0.80	19.81 ±1.69	---	-15.66 ±1.96	---	---	-3.65 ±0.45	-3.33 ±0.55	-8.52 ±0.66	-4.00 ±1.79	-22.43 ±1.40	-26.11 ±1.65	-52.85 ±1.85	---	-81.34 ±2.33	-12.21 ±1.93	-4.27 ±1.25	-10.66 ±3.34	-12.10 ±6.45
C1	7.94 ±0.28	19.27 ±0.57	-0.79 ±0.47	-1.62 ±0.25	-0.52 ±0.14	---	---	---	-2.84 ±0.13	-2.60 ±0.34	-4.90 ±0.23	-3.39 ±0.25	-8.59 ±0.23	---	-17.61 ±0.42	-1.63 ±0.39	---	-3.46 ±1.11	-6.76 ±1.47
C2	7.94 ±0.50	16.14 ±1.04	---	-9.89 ±0.51	-1.16 ±0.22	-2.84 ±0.22	---	-3.81 ±0.32	-5.81 ±0.34	-1.77 ±0.53	-14.84 ±0.37	-14.77 ±0.44	-43.07 ±0.54	-1.80 ±0.39	-60.25 ±0.85	-3.60 ±0.43	-2.65 ±0.60	-10.68 ±1.98	-21.71 ±2.03
C3	7.38 ±0.43	13.88 ±0.85	---	-16.57 ±0.66	-1.07 ±0.25	---	-3.41 ±0.33	-4.33 ±0.36	-9.95 ±0.52	-2.87 ±0.71	-24.25 ±0.48	-20.48 ±0.50	-65.35 ±0.67	-1.60 ±0.25	-94.41 ±1.06	-7.59 ±0.72	-1.94 ±0.63	-24.75 ±2.31	-43.02 ±3.40
C4	5.13 ±0.87	5.56 ±1.81	---	-34.74 ±1.60	-1.49 ±0.99	---	-6.30 ±1.08	-7.87 ±1.32	-17.05 ±1.01	-7.77 ±2.05	-45.08 ±1.40	-31.52 ±1.29	-89.86 ±1.69	-5.85 ±1.13	-144.00 ±2.26	-14.31 ±1.86	---	-16.51 ±3.96	-42.76 ±6.26
C50	6.07 ±0.72	5.70 ±1.57	---	-40.77 ±2.14	---	---	---	-6.14 ±1.06	-14.00 ±0.94	-1.14 ±1.64	-27.22 ±1.16	-14.23 ±0.93	-46.28 ±1.16	---	-99.33 ±1.52	-11.37 ±1.14	---	-7.28 ±2.06	-16.80 ±2.03
B	3.24 ±1.97	-5.19 ±4.49	---	-32.16 ±5.14	---	---	---	---	-6.94 ±1.18	---	-10.74 ±2.24	-9.84 ±2.37	-40.71 ±3.98	---	-36.16 ±1.75	-9.84 ±2.38	---	---	---
A	6.69 ±1.24	15.94 ±3.00	---	-44.90 ±10.25	-8.15 ±5.20	-5.14 ±4.40	---	-4.71 ±2.81	-9.49 ±3.62	6.58 ±5.23	-15.71 ±2.98	-18.54 ±3.60	-32.47 ±4.07	---	-69.84 ±4.36	-9.99 ±2.81	---	---	---
NGC 3395	7.05 ±0.18	15.08 ±0.36	-1.44 ±0.30	-12.24 ±0.70	---	---	-2.43 ±0.35	-3.41 ±0.38	-7.14 ±0.49	-1.87 ±0.59	-11.23 ±0.47	-8.31 ±0.46	-22.31 ±0.55	---	-46.66 ±0.48	-5.88 ±0.41	-0.80 ±0.36	-3.48 ±0.65	-5.34 ±0.77

Table X NGC 3396 Dereddened Emission Line Fluxes

Knot	He II λ1640 (/Hβ)	[O II] λ3727 (/Hβ)	[Ne III] λ3869 (/Hβ)	Hζ λ3889 (/Hβ)	Hε λ3969 (/Hβ)	Hδ λ4102 (/Hβ)	Hγ λ4340 (/Hβ)	He II λ4686 (/Hβ)	Hβ λ4861 (see a)	[O III] λ4959 (/Hβ)	[O III] λ5007 (/Hβ)	He I λ5876 (/Hβ)	Hα λ6563 (see a)	[S II] λ6718, λ6732 (/Hβ)	[Ar III] λ7136 (/Hβ)	[S III] λ9069 (/Hβ)	[S III] λ9531 (/Hβ)
S3	--	--	--	--	--	--	--	--	--	--	--	--	6.69 ±0.61	--	--	--	--
S1	--	--	--	--	--	--	--	--	--	--	--	--	23.91 ±1.62	--	--	--	--
S2	--	--	--	--	--	--	--	--	--	--	--	--	5.56 ±0.88	--	--	--	--
S10	--	--	--	--	--	--	--	--	--	--	--	--	25.12 ±1.24	--	--	--	--
R	--	--	--	--	--	--	--	--	--	--	--	--	23.97 ±0.89	--	--	--	--
R10	--	6.88 ±3.24	--	--	--	--	--	0.07 ±0.28	5.51 ±0.69	0.95 ±0.16	2.73 ±0.36	--	39.71 ±0.80	0.59 ±0.26	0.03 ±0.04	--	--
R20	--	2.57 ±1.07	--	--	--	--	--	0.35 ±0.10	16.91 ±1.05	0.57 ±0.06	1.58 ±0.12	--	77.54 ±1.08	0.62 ±0.27	--	--	0.26 ±0.22
Q3	0.66 ±1.10	3.20 ±1.26	0.13 ±0.05	0.14 ±0.06	0.14 ±0.05	0.23 ±0.06	0.49 ±0.09	0.08 ±0.04	49.25 ±1.11	0.73 ±0.04	1.93 ±0.09	0.13 ±0.04	226.49 ±1.42	0.37 ±0.25	0.06 ±0.03	0.19 ±0.15	0.29 ±0.24
Q2	0.95 ±1.58	3.14 ±1.23	0.13 ±0.04	0.21 ±0.07	0.10 ±0.03	0.26 ±0.07	0.47 ±0.08	0.16 ±0.02	91.83 ±1.41	0.64 ±0.02	1.95 ±0.09	0.13 ±0.04	421.53 ±1.86	0.33 ±0.22	0.06 ±0.03	0.17 ±0.13	0.34 ±0.28
Q1	0.91 ±1.49	2.20 ±0.86	--	0.16 ±0.05	0.19 ±0.06	0.29 ±0.07	0.51 ±0.08	0.13 ±0.01	316.20 ±2.13	1.01 ±0.03	3.08 ±0.13	0.12 ±0.03	1432.29 ±3.32	0.15 ±0.08	0.08 ±0.04	0.20 ±0.16	0.37 ±0.30
Q30	5.45 ±9.06	3.54 ±1.41	--	--	--	0.20 ±0.06	0.53 ±0.09	0.14 ±0.04	29.96 ±0.87	0.75 ±0.04	2.25 ±0.12	0.10 ±0.03	174.24 ±1.18	0.28 ±0.12	0.06 ±0.03	0.19 ±0.14	0.24 ±0.20
Q20	--	5.27 ±2.13	--	--	--	--	0.46 ±0.10	--	37.19 ±1.69	0.44 ±0.04	1.52 ±0.10	--	208.36 ±1.92	0.47 ±0.21	--	--	0.15 ±0.12
Q10	3.89 ±7.64	2.55 ±1.50	--	--	--	--	--	--	5.71 ±1.14	0.41 ±0.15	0.85 ±0.22	--	26.62 ±0.98	0.58 ±0.26	--	--	--

Table X NGC 3396 Dereddened Emission Line Fluxes (Continued)

Knot	He II λ1640 (/Hβ)	[O II] λ3727 (/Hβ)	[Ne III] λ3869 (/Hβ)	Hζ λ3889 (/Hβ)	Hε λ3969 (/Hβ)	Hδ λ4102 (/Hβ)	Hγ λ4340 (/Hβ)	He II λ4686 (/Hβ)	Hβ λ4861 (see a)	[O III] λ4959 (/Hβ)	[O III] λ5007 (/Hβ)	He I λ5876 (/Hβ)	Hα λ6563 (see a)	[S II] λ6718, λ6732 (/Hβ)	[Ar III] λ7136 (/Hβ)	[S III] λ9069 (/Hβ)	[S III] λ9531 (/Hβ)
P2	---	---	---	---	---	---	---	---	(see a)	---	---	---	17.02 ±0.99	---	---	---	---
P	---	3.95 ±2.05	---	---	---	---	---	0.59 ±0.37	6.18 ±0.99	0.78 ±0.18	1.94 ±0.33	---	29.57 ±1.03	0.49 ±0.23	---	---	---
O	---	4.80 ±2.28	---	---	---	---	0.65 ±0.23	---	6.71 ±0.84	0.25 ±0.11	1.21 ±0.23	---	33.99 ±1.17	0.48 ±0.22	---	---	---
N	---	1.56 ±0.75	---	---	---	---	---	0.22 ±0.17	11.19 ±1.40	0.36 ±0.08	0.80 ±0.13	---	27.81 ±1.31	0.64 ±0.30	---	---	---
M	---	---	---	---	---	---	---	---	---	---	---	---	---	---	---	---	---
NGC 3396	3.98 ±6.49	3.92 ±1.54	0.22 ±0.08	---	---	0.15 ±0.04	0.41 ±0.07	0.14 ±0.03	548.24 ±7.04	0.97 ±0.03	2.66 ±0.12	0.10 ±0.03	2856.66 ±8.87	0.28 ±0.17	0.04 ±0.02	0.16 ±0.13	0.26 ±0.21

a flux (10^{-16} erg s^{-1} cm^{-2} Å^{-1})

Table XI NGC3396 Equivalent Widths

Knot	Si IV λ1403 (Å)	C IV λ1550 (Å)	He II λ1640 (Å)	[O II] λ3727 (Å)	[Ne III] λ3869 (Å)	Hζ λ3889 (Å)	Hε λ3969 (Å)	Hδ λ4102 (Å)	Hγ λ4340 (Å)	He II λ4686 (Å)	Hβ λ4861 (Å)	[O III] λ4959 (Å)	[O III] λ5007 (Å)	He I λ5876 (Å)	Hα λ6563 (Å)	[S II] λ6718, λ6732 (Å)	[Ar III] λ7136 (Å)	[S III] λ9069 (Å)	[S III] λ9531 (Å)
S3	4.58 ±4.50	11.13 ±6.97	---	---	---	3.12 ±0.94	2.57 ±0.53	2.60 ±0.65	---	1.67 ±1.48	---	---	---	---	-11.12 ±0.83	---	---	---	---
S1	1.54 ±1.11	12.57 ±1.61	---	-0.73 ±0.15	---	1.69 ±0.11	1.90 ±0.12	2.04 ±0.12	2.33 ±0.12	-0.26 ±0.22	1.48 ±0.12	---	---	---	-3.88 ±0.12	---	---	---	---
S2	6.79 ±1.65	10.62 ±2.74	---	---	---	2.71 ±0.32	2.43 ±0.22	1.96 ±0.21	---	0.09 ±0.45	---	---	---	---	-3.74 ±0.28	---	---	---	---
S10	1.99 ±1.35	9.17 ±2.39	---	-2.69 ±0.39	---	1.57 ±0.18	2.82 ±0.23	2.27 ±0.24	3.19 ±0.24	-1.69 ±0.43	---	---	---	---	-6.95 ±0.24	---	---	---	-1.99 ±0.59
R	8.24 ±1.67	13.94 ±3.21	---	-3.30 ±0.86	---	---	1.36 ±0.21	---	1.37 ±0.22	-1.22 ±0.62	---	-2.39 ±0.34	-3.32 ±0.31	---	-9.14 ±0.27	---	---	---	---
R10	9.54 ±1.73	6.97 ±4.11	---	-10.24 ±0.83	---	---	---	---	---	-0.52 ±0.88	-5.60 ±0.46	-3.90 ±0.47	-11.79 ±0.66	---	-23.39 ±0.44	---	-0.36 ±0.33	---	---
R20	6.82 ±1.83	6.60 ±4.13	---	-20.47 ±1.24	---	---	---	---	---	-3.93 ±1.09	-15.21 ±0.78	-7.77 ±0.68	-21.50 ±0.69	---	-42.29 ±0.57	---	---	---	-7.62 ±0.99
Q3	7.56 ±0.99	9.68 ±2.30	-2.42 ±0.79	-36.16 ±0.75	---	-3.67 ±0.38	-3.45 ±0.33	-4.95 ±0.33	-9.98 ±0.44	-1.66 ±0.95	-26.56 ±0.57	-19.41 ±0.67	-53.34 ±0.77	-3.43 ±0.35	-101.70 ±0.76	---	-2.59 ±0.37	-12.73 ±0.83	-23.04 ±1.19
Q2	6.53 ±0.72	22.32 ±1.46	-3.22 ±1.06	-36.83 ±0.63	-1.31 ±0.18	-4.34 ±0.26	-3.40 ±0.20	-5.87 ±0.27	-10.71 ±0.28	-4.15 ±0.53	-31.90 ±0.49	-20.81 ±0.41	-67.32 ±0.66	-4.43 ±0.24	-137.30 ±0.77	---	-4.32 ±0.31	-22.07 ±0.93	-49.93 ±1.23
Q1	7.26 ±0.42	16.48 ±0.87	-3.69 ±0.46	-32.25 ±0.31	-2.26 ±0.14	-4.58 ±0.12	-5.60 ±0.15	-8.36 ±0.16	-16.61 ±0.22	-5.08 ±0.31	-47.67 ±0.39	-48.48 ±0.40	-153.40 ±0.93	-5.80 ±0.14	-206.40 ±0.60	---	-7.86 ±0.22	-51.12 ±0.85	-117.70 ±1.61
Q30	7.99 ±1.15	12.17 ±2.43	-5.39 ±1.58	-40.30 ±1.52	---	---	---	-5.20 ±0.61	-14.23 ±0.72	-4.66 ±1.42	-39.40 ±1.15	-30.62 ±1.11	-97.46 ±1.88	-3.76 ±0.52	-179.70 ±1.56	---	-4.41 ±0.49	-41.03 ±2.47	-68.34 ±3.92
Q20	6.92 ±0.84	17.13 ±1.52	---	-22.98 ±0.87	---	---	---	---	-4.47 ±0.32	0.18 ±0.67	-11.22 ±0.41	-4.04 ±0.37	-15.80 ±0.54	---	-54.86 ±0.51	---	---	---	-9.06 ±0.99
Q10	3.93 ±2.32	10.66 ±3.56	-2.97 ±1.36	-10.21 ±1.78	---	---	---	---	---	5.49 ±1.89	-9.26 ±1.33	-3.04 ±0.88	-6.58 ±1.22	---	-34.36 ±1.25	---	---	---	---

57

58

Table XI NGC3396 Equivalent Widths (Continued)

Knot	Si IV λ1403 (Å)	C IV λ1550 (Å)	He II λ1640 (Å)	[O II] λ3727 (Å)	[Ne III] λ3869 (Å)	Hζ λ3889 (Å)	Hε λ3969 (Å)	Hδ λ4102 (Å)	Hγ λ4340 (Å)	He II λ4686 (Å)	Hβ λ4861 (Å)	[O III] λ4959 (Å)	[O III] λ5007 (Å)	He I λ5876 (Å)	Hα λ6563 (Å)	[S II] λ6718, λ6732 (Å)	[Ar III] λ7136 (Å)	[S III] λ9069 (Å)	[S III] λ9531 (Å)
P2	8.15 ±1.95	7.16 ±3.45	---	-4.49 ±1.32	---	---	---	---	---	-2.48 ±1.89	---	---	---	---	-16.46 ±0.84	---	---	---	---
P	0.04 ±2.26	23.02 ±3.41	---	-25.79 ±3.11	---	---	---	---	---	-6.44 ±4.19	-17.41 ±2.62	-13.14 ±2.40	-35.62 ±3.23	---	-69.78 ±2.58	---	---	---	---
O	6.40 ±1.85	8.23 ±3.75	---	-35.45 ±3.41	---	---	---	---	-10.48 ±2.15	5.22 ±3.13	-17.81 ±2.26	-4.36 ±1.95	-23.33 ±3.75	---	-65.31 ±2.35	---	---	---	---
N	7.71 ±1.44	21.94 ±2.48	---	-20.69 ±2.04	---	---	---	---	---	-4.27 ±2.88	-19.77 ±2.29	-6.26 ±1.33	-15.44 ±1.65	---	-35.49 ±1.74	---	---	---	---
M	12.72 ±2.87	8.28 ±6.16	---	---	---	---	---	---	---	0.60 ±5.68	---	---	---	---	---	---	---	---	---
NGC 3396	5.48 ±0.26	15.72 ±0.48	-5.09 ±0.38	-21.77 ±0.30	-1.00 ±0.12	---	---	-2.73 ±0.09	-4.47 ±0.10	-1.33 ±0.21	-11.86 ±0.13	-10.35 ±0.15	-30.00 ±0.19	-1.03 ±0.09	-45.93 ±0.16	---	-0.74 ±0.07	-5.92 ±0.22	-10.39 ±0.30

Metallicity Analysis

Determining the age of the starburst is sensitive to the assumed metallicity of the stellar population--the metallicity will be a factor in the stellar evolution, and hence influence our age models. Therefore we estimate the metallicity of the starburst using three different, but complementary methods, (1) via emission line ratios, (2) via UV equivalent widths, and (3) via a UV/visible continuum color ratio.

We find that the line ratio method gives consistent results when applied to a measurement knot or to the unresolved spectrum. The UV equivalent width and color ratio methods provide unreliable results for resolved spectra, but give consistent results when applied to unresolved galaxies. Overall, the methods show that the measurement knots in both galaxies have metallicity (Z) ~0.5-1.0 times solar metallicity ($Z_\odot$).

Metallicity Estimates Via Visible Emission

Line Ratios

The first technique used to estimate the metallicity of the starburst H ɪɪ regions was a forbidden oxygen line ratio method. Pagel et al. (1979) developed a method of estimating the metallicity of H ɪɪ regions using the line ratio R_{23} = ([O ɪɪ] λ3727 + [O ɪɪɪ] $\lambda\lambda$4959, 5007)/Hβ. They calibrated their estimates using several H ɪɪ regions in the Small Magellenic Cloud. The major drawback of using the method of Pagel et al. is that to properly calibrate the method, one needs an independent estimate of electron temperature (for instance the [O ɪɪɪ] and [N ɪɪ] line ratio methods in Osterbrock 1989). Unfortunately these data are frequently not available in extragalactic observations. Edmunds and Pagel (1984) built on the work of Pagel et. al. (1979) and extended the calibration data set from the Small Magellenic Cloud to six different galaxies. McCall, Rybski, and Shields

the Small Magellenic Cloud to six different galaxies. McCall, Rybski, and Shields

(1985) improved on these methods by using a three-level atom model to derive

relationships between temperatures and emission line ratios. Using this model and

extensive observations, they extended the Edmunds and Pagel (1984) calibration to

higher metallicity cases.

Dopita and Evans (1986) continued in the same vein. They modeled several nebular

emission lines and found that they were much more sensitive to the ionization parameter

than to the ionization temperature. They then created new abundance diagnostic

corrected for ionization parameter and then calibrated it using the McCall et al. (1985)

dataset.

Zaritsky, et al. (1994, ZKH hereafter) derived a similar calibration of metallicity

with R_{23}. They examined 39 disk galaxies each of which had at least 5 H II regions in

them and looked for radial abundance gradients. To estimate metallicity they used the

Edmunds and Pagel (1984), McCall, Rybski, and Shields (1985), and Edmunds and Pagel

(1984) calibrations. The metallicity estimates for all three calibrations were averaged and

then the average metallicities were fit analytically as a function of R_{23}.

McGaugh (1991, MCG hereafter) attempted to improve on the R_{23} method by

creating a grid of H II region models as a function of ionizing spectrum, nebular

geometry, and chemical abundance and investigating the sensitivity of the line ratio R_{23} to

the model parameters. From his analysis he defined three metallicity regions as function

of R_{23}: a lower metallicity branch ($Z \leq 0.15\ Z_\odot$), a "turn over" region ($0.15\ Z_\odot \leq Z \leq 0.5$

$Z_\odot$), and an upper branch ($Z \geq 0.5\ Z_\odot$). On the lower branch he found the forbidden

oxygen lines are a primary source of cooling for the electron gas in the H II region and

increasing R_{23} corresponds to increasing metallicity. On the upper branch infrared "fine-

structure" lines are the major source of cooling the electron gas and the intensity of the forbidden oxygen lines declines with increasing metallicity. This results in a double valued relation for metallicity--a given value of R_{23} may be on the upper or lower branch. All of the previously mentioned methods (Pagel, Edwards & Dopita, McCall et al.) were upper branch calibrations.

Furthermore, MCG found that while R_{23} is a good estimator of metallicity on the upper branch, the lower branch is sensitive to both the nebular geometry (through the filling factor) and ionizing spectrum (through the IMF upper stellar mass limit). By measuring the line ratio O_{32} = ([O III] $\lambda\lambda 4959$, 5007)/[O II] $\lambda 3727$, and using it in concert with R_{23}, he found that he could correct for these effects on the lower branch. To numerically determine the actual metallicity, we used the formulae given by Kobulnicky et al. (1999). (MCG never published an analytic expression, only curves. He later fit the curves and Kobulnicky published the expressions.)

MCG broke the R_{23} branch degeneracy by noting that the ratio [N II] / [O II] varies monotonically with Z as well as with R_{23}. He found that the upper branch had log([N II] / [O II]) > -1.0 while the lower branch has log([N II] / [O II]) < -1.0. Unfortunately, as was mentioned in the line measurement section, we are unable to isolate and measure [N II] in our data. Bachilla (2003) analyzed ground based spectra from these galaxies with sufficient spectral resolution to measure the [N II] lines separately. He found that all 36 of his analysis knots had log([N II] / [O II]) > -1.0. While our measurement knots are not the same knots that Bachilla used, the results are suggestive. In an attempt to be more rigorous, we note that Kewley and Dopita (2002, hereafter KD) recommend using the ZKH estimate to break the degeneracy in the McGaugh (1994) method when [N II] is unavailable. The ZKH estimate is most accurate on the upper branch, so if the ZKH

metallicity estimate is on the upper branch ($Z > 0.15\ Z_{\odot}$ or $12+\log(O/H) > 8.1$) then we use the MCG upper branch metallicity solution, otherwise we declare the metallicity to be on the lower branch and use the lower branch calibration. Typically our metallicities were on the upper branch in good agreement with Bachilla (2003).

KD expanded still further on these calibrations. They calculated synthetic ionization parameter and abundance diagnostics for R_{23} and calibrated them using 185 H II regions measured by van Zee (1998). From the van Zee data, they calculated metallicity estimates via the MCG and ZKH methods which they later compare to their KD method. To break the double valued nature of the R_{23} diagnostic, KD parameterized their R_{23} estimate by the ionization parameter, $q = S_H/n$, where S_H is the flux of ionizing photons through a unit area and n is the number density of hydrogen. KD also parameterized the ratio [O III]/[O II] as a function of q to allow iterative determination of q as will be described later.

KD defined an "optimal" method of metallicity determination. The optimal method starts with an initial abundance estimate using the ZKH R_{23} method and then follows one of three paths:

High metallicity: If the ZKH estimate for $12 + \log(O/H) > 9.0$ then we use this value to estimate the ionization parameter, q, from KD's modeling of [O III] / [O II]. We then use this q to calculate the KD R_{23} method abundance. We then iterate, using the new abundance to get a new q which generates a new abundance, etc. until we converge to a solution. We then form an error bar weighted average of the KD, ZKH and MCG estimates, where the ZKH and MCG metallicity estimates are calculated as described previously. If the KD method does not converge, it is discarded and we form the weighted average with only the ZKH and MCG estimates.

Turn over region: If our initial ZKH estimate yields $8.5 < 12 + \log(O/H) < 9.0$, then we form an error bar weighted average of the ZKH and MCG metallicity estimates, without using the KD estimate.

Low metallicity region: The KD method alone is used since the ZKH method is unreliable at low metallicity and the MCG can be as well. If the iteration doesn't converge with the initial ZKH estimate, we try using the MCG lower branch estimate as the seed to the iteration. If it still doesn't converge, then we form a weighted average of the MCG and ZKH estimates since it the only option remaining.

By forming the weighted average in the methods above, the scatter is reduced, even in the case where we only have the ZKH and MCG metallicity estimates (recall, the ZKH and MCG are computationally independent calibrations even though we use the ZKH to determine whether to calculate the MCG metallicity on the upper or lower branch).

Metallicity Estimates Via C IV $\lambda1550$

and S IV $\lambda1403$ Equivalent Widths

Storchi-Bergmann, Calzetti, and Kinney (1994, SCK hereafter) presented calibrations relating the equivalent width of the C IV $\lambda1550$ and S IV $\lambda1403$ absorption lines to metallicity. SCK observed 44 star forming galaxies, 17 of which were starburst galaxies, and derived calibrations based on their results.

To derive the metallicity, SCK calculated the nebular gas density and relative ionic abundances of O^+, O^{++}, N^{++}, S^+ and S^{++}. They calculated the gas density from the observed [S II] $\lambda 6717$/[S II] $\lambda 6731$ emission line ratio based the McCall (1984) three level atom calibration. In order to do this they calculated T[O II], the nebular O^+ temperature, which they used as a proxy for the nebular S^+ temperature, T[S II].

To determine the relative ionic abundances, they used McCall's (1984) three-level atom model. This model depends on the previously derived gas density as well as the temperature distribution in the nebula.

For the low ionization species O^+, N^+ and S^+, SCK used T[O II] to characterize the nebular temperature. Due to the difficulty of observing the effects of this temperature directly, it was obtained from the following convoluted route. First R_{23} was measured, then T[O III] was obtained from R_{23} via the calibration diagrams of Pagel et al. (1979) and Dopita & Evans (1986). Then the Campbell et al. (1986) relations, described below, were used to obtain T[O II] from T[O III]

The high ionization O^{++} and N^{++} region temperatures were characterized by T[O III] obtained from the emission line ratio [O III] $\lambda\lambda 4959,5007$/[O III] $\lambda 4363$ and the two temperature zone model of Campbell et al. (1986, described below). For the characteristic temperature of the S^+ region T[S II], they used the results of Garnett (1992) who determined that T[S II] is between T[O II] and T[O III] and published a calibration for T[S II] as a function of T[O III].

As mentioned previously, Campbell et. al. (1986) provided a calibration relating the easy to observe [O III] temperature to the harder to observe (due to the weakness of the lines) [O II] temperature. To do this they collected high signal to noise spectra of 32 H II

galaxies, measured the [O III] and [O II] fluxes, and calculated the electron temperatures

for the [O III] and [O II] regions using the method of Osterbrock (1974).

SCK related their calculated metallicities to several measured quantities including

the equivalent width of C IV λ1550 and Si IV λ1403. They defined the equivalent width as

the absorption in the window $\lambda\lambda$1380-1415Å and $\lambda\lambda$1523-1576Å for Si IV and C IV

respectively. Using these definitions, absorption was measured in our spectra and the

metallicities were estimated using the calibration of SCK. For C IV, SCK fit the data both

with a line and a second order polynomial. We will estimate the metallicity using both

fits and assess the relative merits of each.

Metallicity Estimates Via
Continuum Fluxes

SCK also related their derived metallicity to a UV to visible continuum color. They

defined their color as

$$C(14-35) = -2.5 \log \frac{F_{\lambda 1355}}{F_{\lambda 3500}} \qquad (4)$$

We calculate the continuum values in the same manner as SCK. For the UV flux we

calculated the average flux in the range 1348-1365 Å and for the visible flux the average

was calculated over the range 3492.5-3507.5 Å.

Metallicity Estimation Results

Using the methods described above, the metallicity of each knot in each galaxy was

estimated. The resulting metallicity estimates for each of the methods are presented in

Tables XII and XIII for NGC 3395 and NGC 3396 respectively. In these tables, when a

value could not be measured or could not be calculated, we denote this by the entry "---".

Column (1) is the name of the knot; columns (2) and (3) are the equivalent widths of C IV

$\lambda 1550$ and Si IV $\lambda 1403$ in Angstroms; column (4) is the SCK color (14-35); column (5) is

R_{23} = ([O II] $\lambda 3727$ + [O III] $\lambda\lambda 4959, 5007$)/H$\beta$. The error bars for columns (2) through

(5) are the measurement error for each quantity.

In columns (6) through (14) are the various estimates of 12 + log(O/H). The error

bars presented in columns (6) through (14) are the measurement error summed in

quadrature with the systematic error for each estimation method. Columns (6) and (7) are

the SCK linear and polynomial C IV metallicity estimates; column (8) is the Si IV

metallicity estimate; column (9) is the color (14-35) metallicity estimate; column (10) is

the average of the SCK Si IV, linear C IV and color (14-35) metallicity estimates; column

(11) is Z_r, the reduced average of the SCK metallicity estimates limited to Si IV method

metallicity estimates ≥ 8.0, C IV method metallicity estimates ≤ 9.0, and C(14-35) method

metallicity estimates ≤ 9.0. Column (12) is the MCG (1991) metallicity estimate; column

(13) is the ZKH (1994) metallicity estimate; column (14) is the KD (2002) metallicity

estimate.

Column (15) is provided for comparison purposes and represents the metallicity in

units where the metallicity of the sun equals 1.0 (when Z' = 8.92, the solar value for 12 +

log(O/H), Z = 1.0 in the formula below). This value is calculated according to the

formula:

$$Z = 10^{[0.9893 * (Z' - 12.0) + 3.0441]} \tag{5}$$

where Z' is the KD metallicity estimate, if it could be calculated, otherwise it is the

Z_r estimate. (In one knot, S1 in NGC 3395, there was no Z_r estimate either so we used

Z_{avg} since it was all that was available.) We will use this value of the metallicity as our "best" estimate of the metallicity for all further analyses. Error bars presented are the KD, Z_r or Z_{avg} error bars, as appropriate, in this unit system.

Table XII. NGC 3395 Metallicity Estimates

| Knot | EW (Å) | | | R_{23} | Metallicity 12 + log(O/H) | | | | | | | | | |
	$C\ IV$ $\lambda1550$	$Si\ IV$ $\lambda1403$	Color (14-35)		Linear $C\ IV$	Poly. $C\ IV$	$Si\ IV$	Color (14-35)	Z_{avg}	Z_r	MCG	ZKH	KD	Z
D	16.80 ±4.19	9.28 ±1.89	0.58 ±0.47	---	9.45 ±0.44	---	9.00 ±0.41	9.63 ±0.49	9.33 ±0.26	9.00 ±0.41	---	---	---	1.18 ±1.12
C80	12.36 ±3.08	8.50 ±1.57	-0.04 ±0.22	0.78 ±0.09	9.03 ±0.35	---	8.88 ±0.38	9.26 ±0.42	9.04 ±0.22	8.88 ±0.38	8.61 ±0.15	8.66 ±0.25	8.62 ±0.14	0.51 ±0.17
C70	16.49 ±1.91	6.41 ±1.04	-0.78 ±0.21	0.70 ±0.08	9.42 ±0.27	---	8.56 ±0.34	8.82 ±0.42	9.03 ±0.19	8.66 ±0.26	8.71 ±0.13	8.79 ±0.23	8.73 ±0.13	0.64 ±0.19
C60	19.81 ±1.69	6.22 ±0.80	-1.34 ±0.18	0.71 ±0.07	9.74 ±0.26	---	8.53 ±0.32	8.48 ±0.41	9.12 ±0.18	8.51 ±0.26	8.71 ±0.13	8.78 ±0.22	8.73 ±0.13	0.64 ±0.18
C1	19.27 ±0.57	7.94 ±0.28	-1.31 ±0.03	0.70 ±0.06	9.69 ±0.21	---	8.79 ±0.30	8.50 ±0.40	9.26 ±0.16	8.69 ±0.24	8.73 ±0.12	8.78 ±0.22	8.74 ±0.12	0.66 ±0.18
C2	16.14 ±1.04	7.94 ±0.50	-0.95 ±0.06	0.77 ±0.05	9.39 ±0.22	---	8.79 ±0.31	8.71 ±0.40	9.11 ±0.16	8.76 ±0.25	8.66 ±0.12	8.68 ±0.22	8.67 ±0.12	0.56 ±0.16
C3	13.88 ±0.85	7.38 ±0.43	-1.46 ±0.10	0.73 ±0.06	9.18 ±0.22	---	8.71 ±0.31	8.41 ±0.40	8.92 ±0.16	8.60 ±0.24	8.69 ±0.12	8.75 ±0.22	8.70 ±0.12	0.61 ±0.17
C4	5.56 ±1.81	5.13 ±0.87	-1.62 ±0.22	0.67 ±0.07	8.39 ±0.26	8.50 ±0.23	8.37 ±0.33	8.31 ±0.42	8.37 ±0.18	8.37 ±0.18	8.73 ±0.13	8.82 ±0.22	8.75 ±0.12	0.68 ±0.19
C50	5.70 ±1.57	6.07 ±0.72	-0.93 ±0.21	0.74 ±0.11	8.41 ±0.25	8.51 ±0.22	8.51 ±0.32	8.72 ±0.42	8.50 ±0.18	8.50 ±0.18	8.63 ±0.15	8.72 ±0.26	8.65 ±0.14	0.54 ±0.18
B	-5.19 ±4.49	3.24 ±1.97	-0.39 ±0.68	1.07 ±0.18	---	---	8.08 ±0.42	9.05 ±0.57	8.42 ±0.34	8.08 ±0.42	8.62 ±0.36	8.00 ±0.59	8.08 ±0.32	0.15 ±0.11
A	15.94 ±3.00	6.69 ±1.24	-0.36 ±0.64	0.91 ±0.17	9.37 ±0.35	---	8.61 ±0.35	9.07 ±0.55	9.01 ±0.23	8.61 ±0.35	8.42 ±0.31	8.42 ±0.42	8.42 ±0.26	0.32 ±0.19
NGC 3395	15.08 ±0.36	7.05 ±0.18	-1.05 ±0.08	0.78 ±0.09	9.29 ±0.20	---	8.66 ±0.30	8.66 ±0.40	9.03 ±0.16	8.66 ±0.24	8.60 ±0.15	8.66 ±0.25	8.62 ±0.14	0.50 ±0.16

Table XIII. NGC 3396 Metallicity Estimates

| Knot | EW (Å) | | | R_{23} | 12 + Metallicity log(O/H) | | | | | | | | | Z |
	C IV λ1550	Si IV λ1403	Color (14-35)		Linear C IV	Poly. C IV	Si IV	Color (14-35)	Z_{avg}	Z_r	MCG	ZKH	KD	
S3	11.13 ±6.97	4.58 ±4.50	0.29 ±0.35	---	8.92 ±0.69	9.11 ±3.87	8.28 ±0.75	9.45 ±0.45	9.09 ±0.34	8.63 ±0.51	---	---	---	0.51 ±0.59
S1	12.57 ±1.61	1.54 ±1.11	-0.02 ±0.04	---	9.05 ±0.25	---	7.82 ±0.34	9.27 ±0.40	8.76 ±0.18	---	---	---	---	0.69 ±0.28
S2	10.62 ±2.74	6.79 ±1.65	-0.74 ±0.11	---	8.87 ±0.33	8.96 ±0.55	8.62 ±0.39	8.84 ±0.41	8.79 ±0.21	8.79 ±0.21	---	---	---	0.73 ±0.36
S10	9.17 ±2.39	1.99 ±1.35	-0.34 ±0.09	---	8.73 ±0.30	8.77 ±0.31	7.89 ±0.36	9.08 ±0.40	8.56 ±0.20	8.73 ±0.30	---	---	---	0.65 ±0.45
R	13.94 ±3.21	8.24 ±1.67	0.03 ±0.12	---	9.18 ±0.36	---	8.84 ±0.39	9.30 ±0.41	9.11 ±0.22	8.84 ±0.39	---	---	---	0.83 ±0.74
R10	6.97 ±4.11	9.54 ±1.73	-0.04 ±0.17	1.02 ±0.13	8.53 ±0.44	8.59 ±0.35	9.04 ±0.40	9.26 ±0.41	8.96 ±0.24	8.80 ±0.29	8.19 ±0.30	8.13 ±0.43	8.17 ±0.25	0.18 ±0.10
R20	6.60 ±4.13	6.82 ±1.83	-0.21 ±0.19	0.67 ±0.10	8.49 ±0.44	8.57 ±0.34	8.62 ±0.41	9.16 ±0.42	8.76 ±0.24	8.56 ±0.30	8.71 ±0.14	8.82 ±0.24	8.74 ±0.13	0.66 ±0.20
Q3	9.68 ±2.30	7.56 ±0.99	-0.75 ±0.09	0.77 ±0.09	8.78 ±0.30	8.83 ±0.33	8.74 ±0.34	8.84 ±0.40	8.78 ±0.19	8.78 ±0.19	8.61 ±0.15	8.68 ±0.25	8.63 ±0.14	0.51 ±0.16
Q2	22.32 ±1.46	6.53 ±0.72	-0.62 ±0.05	0.76 ±0.09	9.97 ±0.24	---	8.58 ±0.32	8.91 ±0.40	9.36 ±0.17	8.71 ±0.25	8.62 ±0.15	8.70 ±0.25	8.64 ±0.14	0.53 ±0.17
Q1	16.48 ±0.87	7.26 ±0.42	-0.73 ±0.02	0.80 ±0.06	9.42 ±0.22	---	8.69 ±0.31	8.84 ±0.40	9.12 ±0.16	8.75 ±0.24	8.62 ±0.13	8.63 ±0.23	8.62 ±0.13	0.50 ±0.15
Q30	12.17 ±2.43	7.99 ±1.15	-1.43 ±0.14	0.82 ±0.09	9.02 ±0.30	---	8.80 ±0.35	8.43 ±0.41	8.80 ±0.20	8.64 ±0.26	8.55 ±0.23	8.60 ±0.26	8.58 ±0.18	0.45 ±0.19

Table XIII. NGC 3396 Metallicity Estimates (Continued)

Knot	EW (Å)				Metallicity log(O/H)									
	C IV λ1550	Si IV λ1403	Color (14-35)	R_{23}	Linear C IV	Poly. C IV	Si IV	Color (14-35)	Z_{avg}	Z_r	MCG	ZKH	KD	Z
Q20	17.13 ±1.52	6.92 ±0.84	-0.82 ±0.09	0.86 ±0.13	9.48 ±0.25	---	8.64 ±0.33	8.79 ±0.40	9.10 ±0.18	8.70 ±0.25	8.44 ±0.25	8.52 ±0.32	8.47 ±0.21	0.36 ±0.17
Q10	10.66 ±3.56	3.93 ±2.32	-0.60 ±0.31	0.58 ±0.17	8.87 ±0.39	8.97 ±0.72	8.19 ±0.46	8.92 ±0.44	8.69 ±0.25	8.69 ±0.25	8.78 ±0.16	8.93 ±0.27	8.82 ±0.15	0.79 ±0.27
P2	7.16 ±3.45	8.15 ±1.95	-0.31 ±0.26	---	8.54 ±0.38	8.61 ±0.32	8.83 ±0.42	9.10 ±0.43	8.80 ±0.24	8.67 ±0.28	---	---	---	0.56 ±0.36
P	23.02 ±3.41	0.04 ±2.26	-3.94 ±9.59	0.82 ±0.14	10.04 ±0.38	---	7.60 ±0.46	6.93 ±5.72	9.04 ±0.29	6.93 ±5.72	8.53 ±0.26	8.59 ±0.32	8.55 ±0.21	0.43 ±0.21
O	8.23 ±3.75	6.40 ±1.85	-0.84 ±0.36	0.80 ±0.16	8.64 ±0.41	8.69 ±0.37	8.56 ±0.41	8.78 ±0.45	8.65 ±0.24	8.65 ±0.24	8.52 ±0.26	8.63 ±0.34	8.56 ±0.21	0.44 ±0.22
N	21.94 ±2.48	7.71 ±1.44	-1.08 ±0.38	0.43 ±0.12	9.94 ±0.31	---	8.76 ±0.37	8.64 ±0.46	9.28 ±0.21	8.71 ±0.29	8.90 ±0.12	9.05 ±0.22	7.81 ±0.25	0.08 ±0.04
M	8.28 ±6.16	12.72 ±2.87	0.01 ±0.40	---	8.65 ±0.61	8.69 ±0.55	9.52 ±0.53	9.29 ±0.46	9.21 ±0.30	9.15 ±0.40	---	---	---	1.68 ±1.53
NGC 3396	15.72 ±0.48	5.48 ±0.26	-0.48 ±0.03	0.88 ±0.09	9.35 ±0.21	---	8.42 ±0.30	9.00 ±0.40	9.05 ±0.16	8.63 ±0.24	8.47 ±0.24	8.48 ±0.27	8.48 ±0.19	0.36 ±0.16

Metallicity Estimation Technique

Consistency Analysis

We will examine the different metallicity estimates for consistency with each other. To assist us, in Figure 6, we plot metallicities determined by the various methods against each other. In Figures 6a, b and c, notice that the emission line metallicity estimates (KD, MCG and ZKH) all trend well together. This is unsurprising since the underlying physics is the same for all three methods and furthermore, the KD estimate is typically the average of the MCG and ZKH methods. There can be some disagreement at low metallicity, when the ZKH and MCG metallicity estimate a knot is on the upper branch while the KD method predicts it to be on the lower branch. In particular, the knot with the smallest KD estimate of 7.81 disagrees with all the other methods and comes from a fairly noisy spectrum (Figure 5q). We therefore ignore this data point in all subsequent analysis. The color (14-35) method (Figure 6d) generally trends well with Z_{avg}. For values less than a metallicity of about 9.0, it gives similar results to the emission line methods, but then diverges for larger values. This is on the upper branch where we expect the emission line method's calibrations to be the most accurate. Therefore we recommend against using the color (14-35) method for $12 + \log (O/H) > 9.0$.
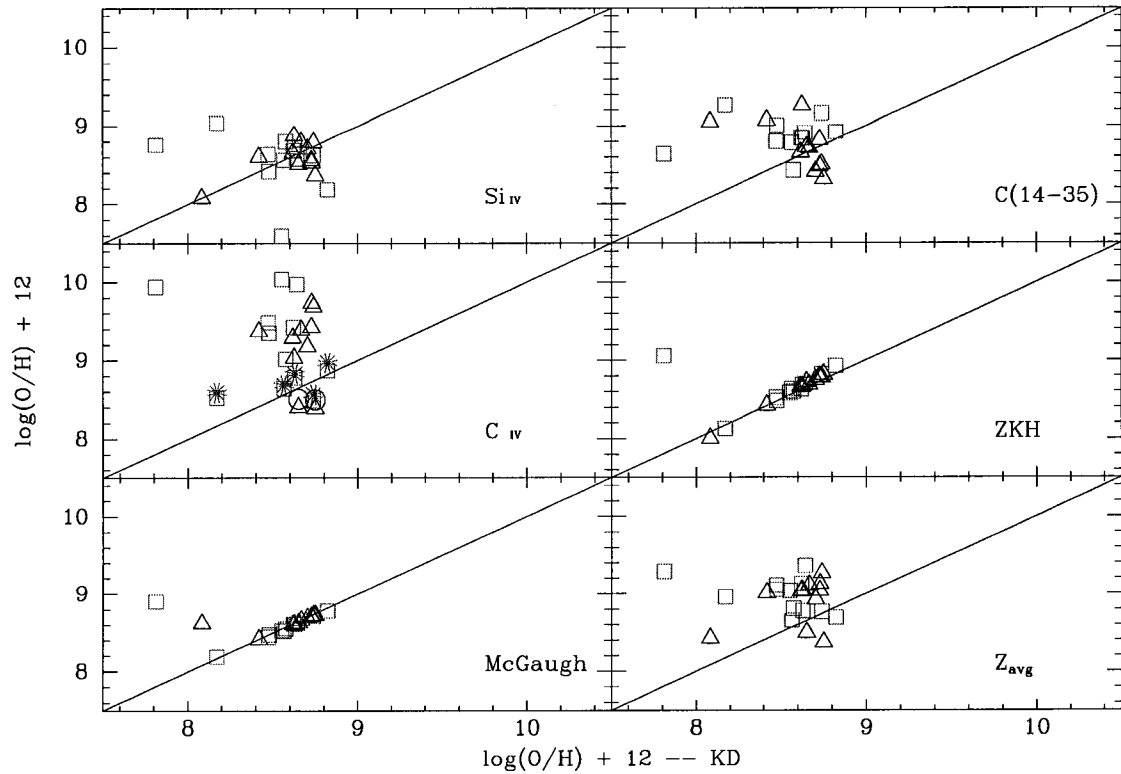
Figure 6a. Kewley Dopita Metallicity Comparison

Figure 6a-h. Metallicity comparisons. NGC 3395 measurement knots are shown as triangles, NGC 3396 measurement knots are shown as squares. When the SCK C IV polynomial fit method is displayed it is shown as circles in NGC 3395 and asterisks in NGC 3396. Each pane has the same x-axis but the y-axis for each pane is the metallicity estimate as labeled in that pane. The diagonal line represents x-axis = y-axis. For clarity, only the C IV linear fit is used for the x-axis in figure (f).
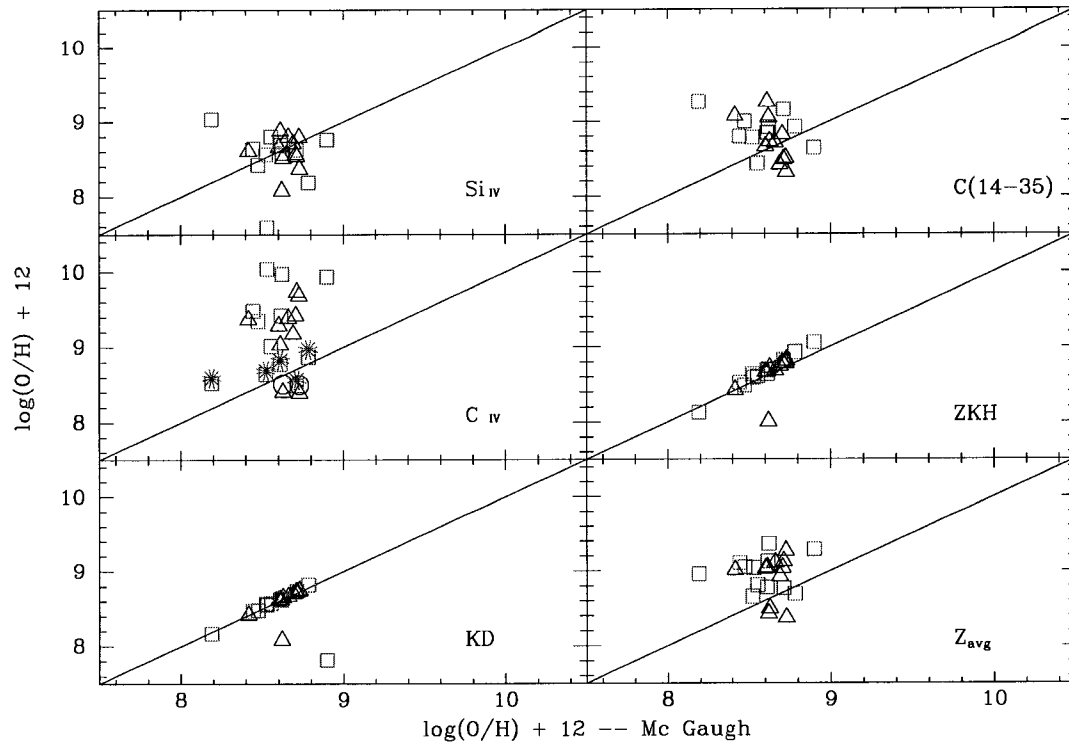
Figure 6b. McGaugh Metallicity Comparison
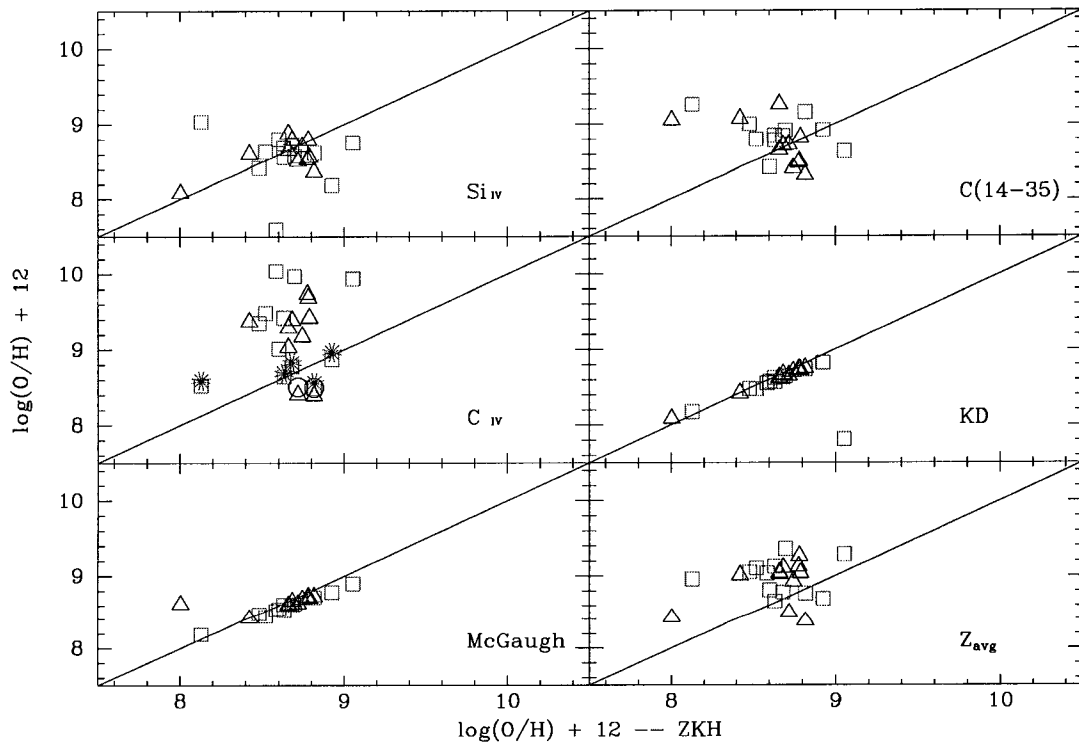
Figure 6c. ZKH Metallicity Comparison
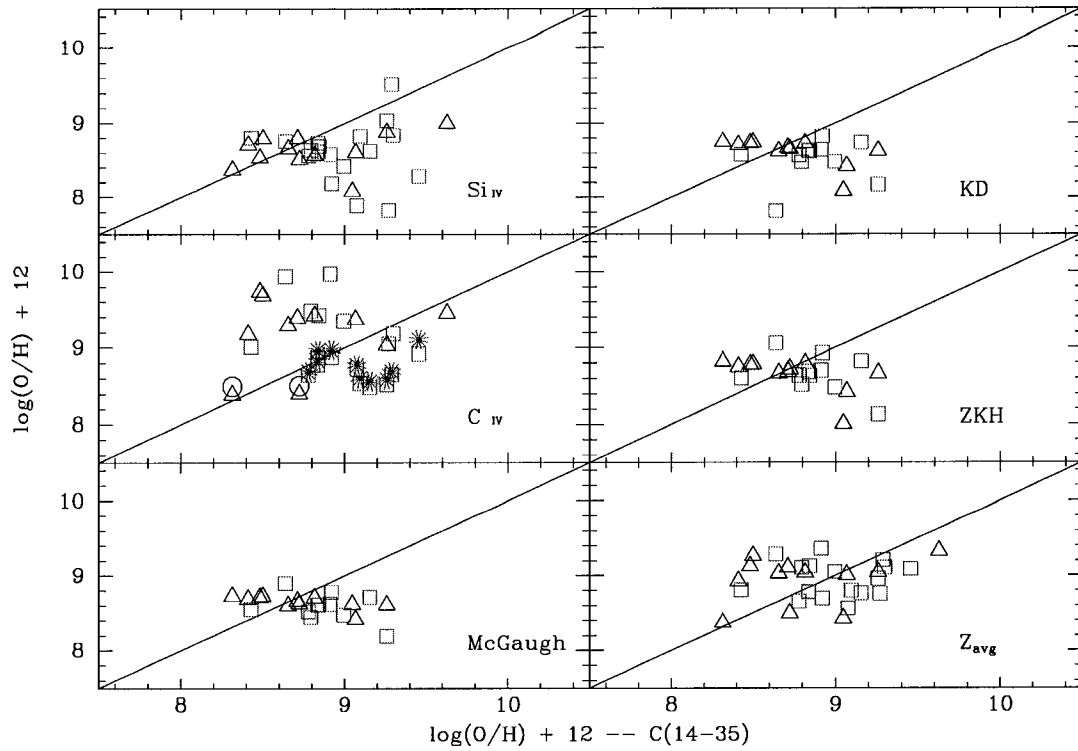
Figure 6d. SCK Color (14-35) Metallicity Comparison
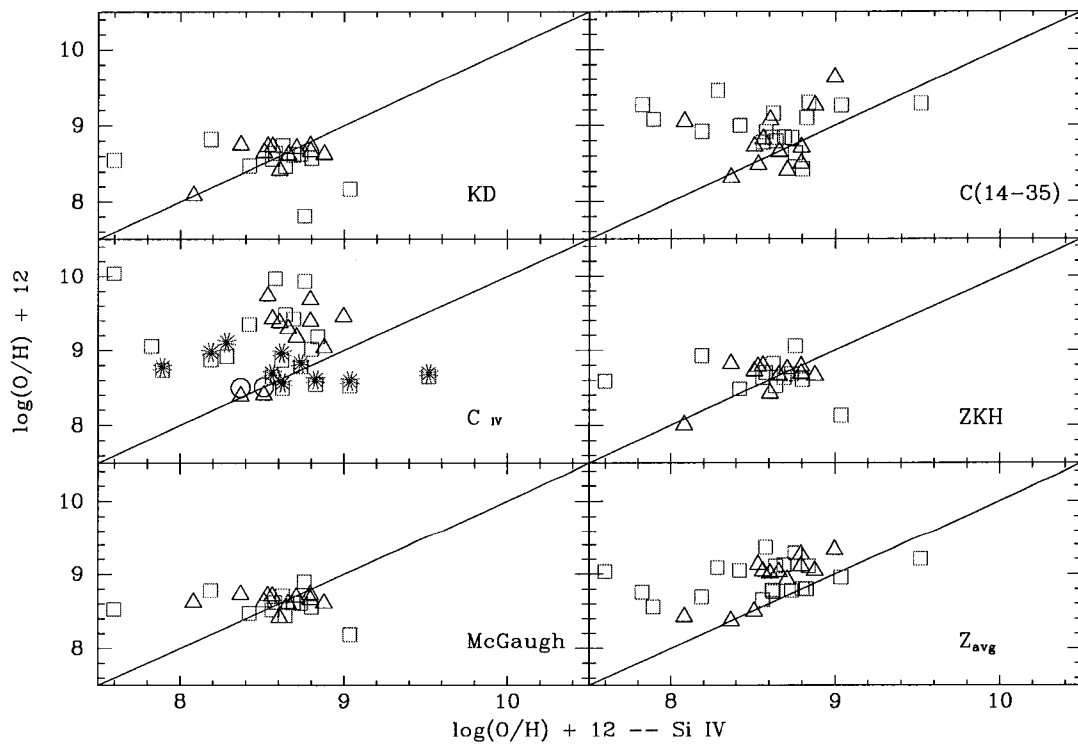
Figure 6e. SCK Si IV Metallicity Comparison
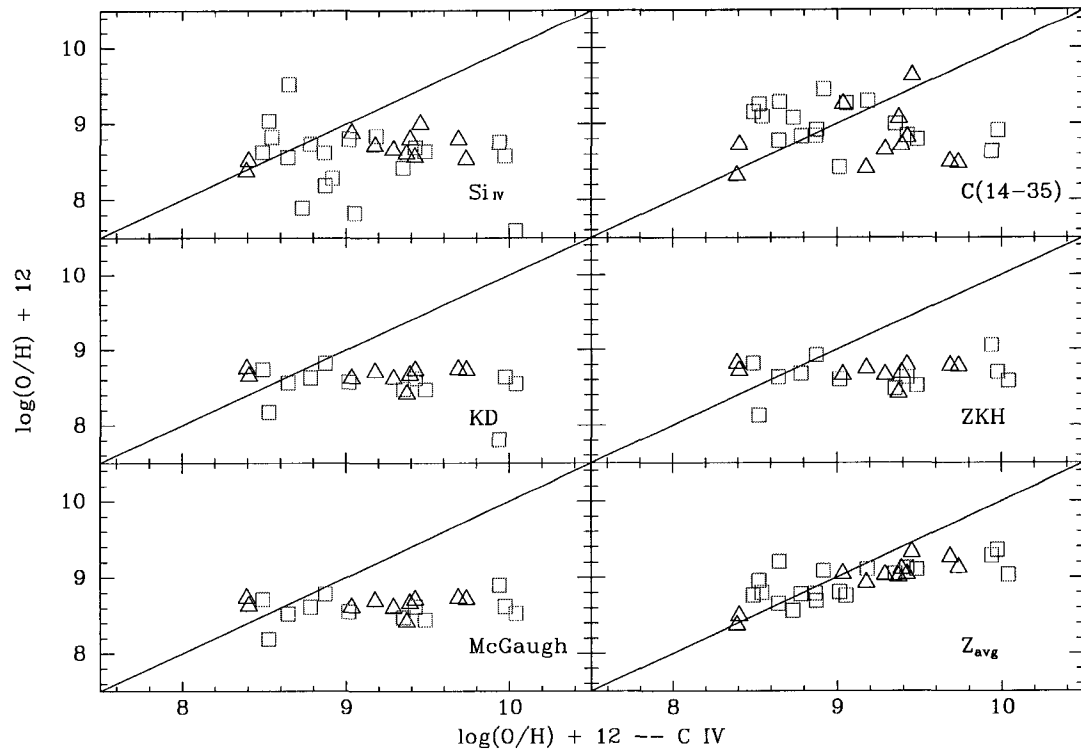
Figure 6f. SCK C ɪᴠ Metallicity Comparison

(For clarity, only the linear fit is shown on the x-axis)
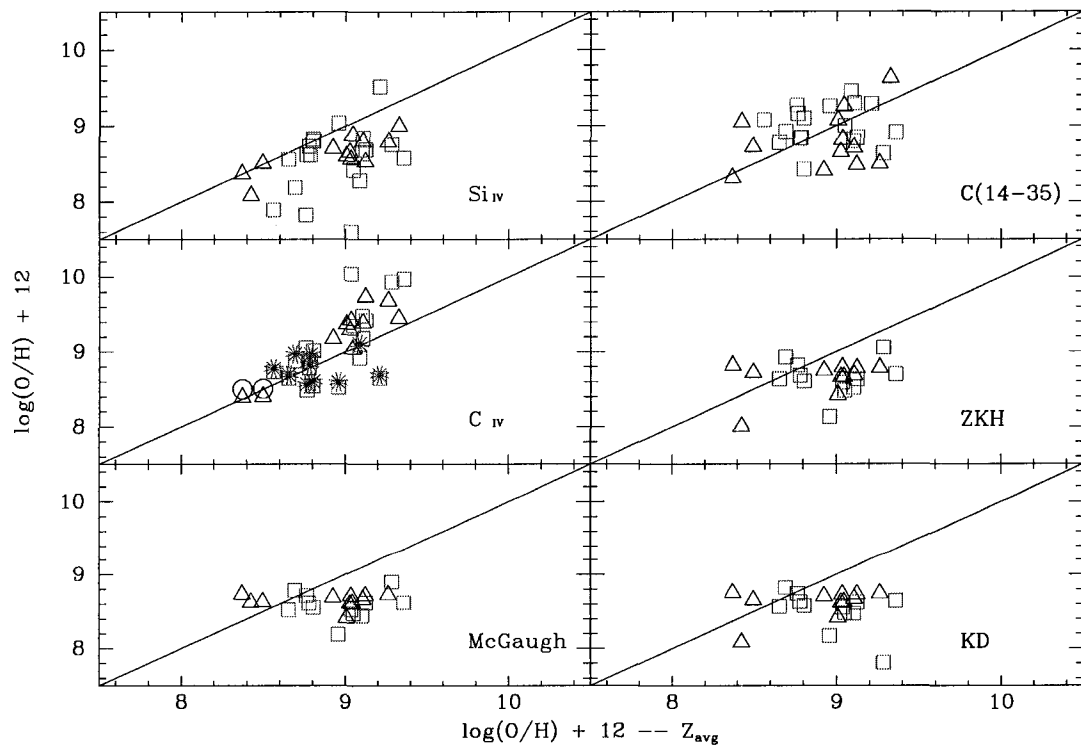
Figure 6g. SCK 94 Average Metallicity Comparison
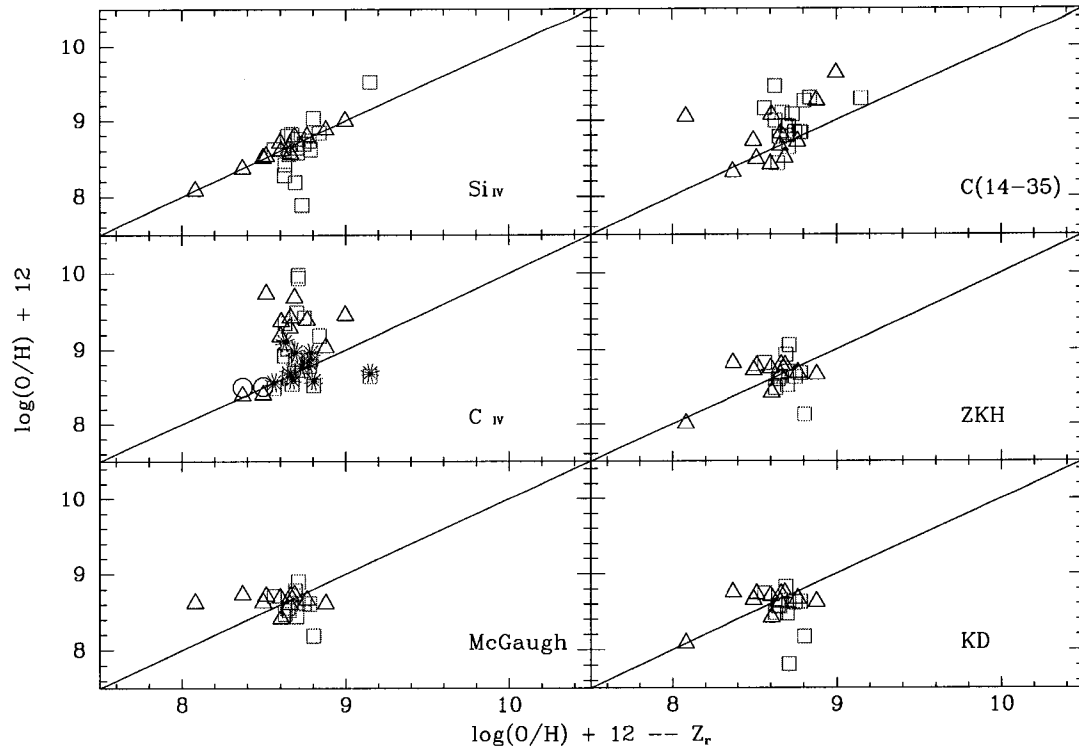
Figure 6h. SCK 94 Reduced Average Metallicity Comparison

Next we examine the Si IV method in Figure 6e. The Si IV method and the emission line methods give comparable estimates around a metallicity of 8.6 with a few outliers. The furthest outlier is knot P in NGC 3396 with an Si IV method estimate of a metallicity of 7.60. From Figure 5(o) we see that this spectrum does not exhibit strong starburst features and has a pronounced Balmer decrement. The weak Si IV absorption measurement was noisy (EW = 0.04 Å ± 2.26) and is therefore discarded. Referring back to SCK, the minimum metallicity that the Si IV method was calibrated against was approximately a metallicity of 8.3. To determine how low the calibration is valid, note that the Si IV method is consistent with both the KD and Z_{avg} methods down to approximately a metallicity of 8.0 and with the C(14-35) method down to about a metallicity of 8.3. The conservative approach would be to disregard all Si IV method estimates below a metallicity of 8.3; however we believe this would be overly

conservative. From SCK, there is considerable scatter in the C(14-35) calibration compared to the Si IV calibration, therefore we recommend against using the Si IV method below a metallicity of $12 + \log (O/H) = 8.0$ based on our results.

Figure 6f shows the C IV method has difficulty at high metallicity. (Note that in the interest of clarity, in this figure we only show the linear method, not both the linear and polynomial methods. Since the metallicities calculated from the linear and polynomial methods are so close to each other over the region where the polynomial can be solved, it unduly clutters the chart.) Above about a metallicity of 9.2 the C IV method is consistently larger than all the other methods and diverges from the emission line methods. Above a metallicity of about 9.5 the C IV method diverges from the Si IV and C(14-35) estimates. Reviewing the SCK paper, we note that the maximum metallicity that they calibrated against was a metallicity of $12 + \log(O/H) \sim 9.2$ which is in general lower than the estimates we are obtaining. Furthermore, above a metallicity of about 9.0 the C IV method strongly diverges above the emission line methods. This is on the upper branch where we expect the emission line methods calibrations to be the most accurate. Therefore we recommend against using the C IV method above a metallicity of $12 + \log (O/H) = 9.0$.

Figure 6g shows the SCK average metallicity, Z_{avg}, vs. the various estimates. We calculated Z_{avg} to reduce the scatter of the various SCK methods by combining them into a weighted average. As can be seen, the results are not very satisfactory. Z_{avg} is in poor agreement with the emission line estimates everywhere except at approximately a metallicity of $12 + \log (O/H) = 8.6$. It does not even trend well with its components above a metallicity of about 9.0. The C IV method drastically diverges above the average, pulling the average up and causing the Si IV method to diverge below. The color (14-35)

method seems to trend with the average in a very general sense, but the scatter is enormous.

We attempt to remedy the deficiencies in Z_{avg} by applying the restrictions we derived in the previous paragraphs on it's components. We calculated the weighted average of these restricted estimates and called it the reduced SCK average, or Z_r. The component estimates are limited as follows:

- Si IV method metallicity estimates ≥ 8.0

- C IV method metallicity estimates ≤ 9.0

- C(14-35) method metallicity estimates ≤ 9.0

Figure 6h shows the results and Table XIV tabulates the change in RMS between the various estimation methods and Z_{avg} or Z_r. In the figure and the table, we show the correlation for all the SCK estimate values with Z_r, not just the SCK values that met our requirements for inclusion in the Z_r average. In the table each entry is the RMS between the metallicity estimates generated by the row and the column. Row (2) is the RMS values with respect to Z_{avg}; row (3) is the RMS values with respect to Z_r; row(4) is change in RMS: $RMS(Z_r) - RMS(Z_{avg})$; and row (5) is $(RMS(Z_r) - RMS(Z_{avg}))/RMS(Z_{avg})$: the percent change. Column (2-7) are the RMS with respect to the C IV, Si IV, Color (14-35), MCG, ZKH, and KD metallicity estimates respectively.

Overall, there is dramatic improvement in the correlation between most of the methods and Z_r, except for the C IV method. The C IV looks worse because it is--by excluding the large values of C IV from our average, we make Z_r trend worse with C IV. Therefore, for spatially resolved galaxies, the SCK reduced average exhibits significant scatter, but is reliable to approximately 0.4 dex with respect to the emission line methods.

Table XIV. Estimation Method RMS Change Between Z_{avg} and Z_r

	C IV (RMS)	Si IV (RMS)	Color (14-35) (RMS)	MCG (RMS)	ZKH (RMS)	KD (RMS)
Z_{avg}	0.37	0.50	0.53	0.44	0.42	0.53
Z_r	0.83	0.25	0.36	0.40	0.41	0.43
Δ RMS	0.46	-0.25	-0.17	-0.04	-0.01	-0.10
%	124.34	-50.00	-32.07	-9.09	-2.38	-18.87

There are several possible explanations for the observed problems with the SCK methods. It is likely that the observed problem with the SCK methods is due to the fact that we are using them on spatially resolved spectra when they were calibrated against spatially unresolved spectra. First of all, unresolved spectra of an entire galaxy may include horizontal branch or other older hot stars which are not included in our smaller starburst knots. These older stars may contribute to the UV continuum and absorption in different ways from our strictly young population, although we have no way of proving this from the data at hand.

Secondly, several of our measurement knots are well outside of the metallicity region over which the SCK methods were calibrated. If this is the reason for the disagreement, then the reduced average, Z_r, should compensate for this. To assess whether or not this is the case, we examine the unresolved knots. From Tables XII and XIII, the NGC 3395 unresolved knot has $Z_r = 8.66 \pm 0.24$ and $Z_{KD} = 8.62 \pm 0.14$ while the NGC 3396 unresolved knot $Z_r = 8.63 \pm 0.24$ and $Z_{KD} = 8.48 \pm 0.19$. Both estimates in both galaxies are in excellent agreement. Note that in both cases the C IV estimate was outside the restricted range and was removed from the reduced average. Therefore we find that the reduced average of the SCK methods is appropriate for spatially unresolved galaxies based on these data.

For the remainder of this dissertation, we will use the KD metallicity estimate, when it is available, for all future analyses. When the KD is not available, we will use the reduced SCK average, Z_r.

Unresolved Spectra Representativeness and

Metallicity Gradient Analysis

Now we will analyze the data for consistency of the metallicity estimates between the spatially resolved and unresolved spectra. We seek to characterize how representative the unresolved knots are of the measurement knots of which they are composed. We also seek to determine if there is any metallicity gradient in the galaxies. To assist our analysis, we employ the graphical technique depicted in Figures 7 and 8. Each figure consists of 8 panels, one for each metallicity estimation technique. For each knot in each panel, we plot the calculated metallicity with error bars on the vertical axis. On the horizontal axis we plot the spatial center pixel of the knot in the G430L detector. In each panel, we also plot two dotted horizontal lines depicting the unresolved knot metallicity estimate ± measurement error in that panel.

Reviewing the figures, it is immediately apparent that there is no metallicity gradient in the data shown. We also see that the unresolved spectra are in general very representative of the measurement knots they are composed of. Almost all the knots in both galaxies are within one error bar of the unresolved estimates. The improvement between Z_{avg} and Z_r is also apparent, particularly in NGC 3395. From these plots we conclude that the metallicity estimate of the unresolved knots are representative of the underlying metallicity estimates of the star forming knots of which they are composed.
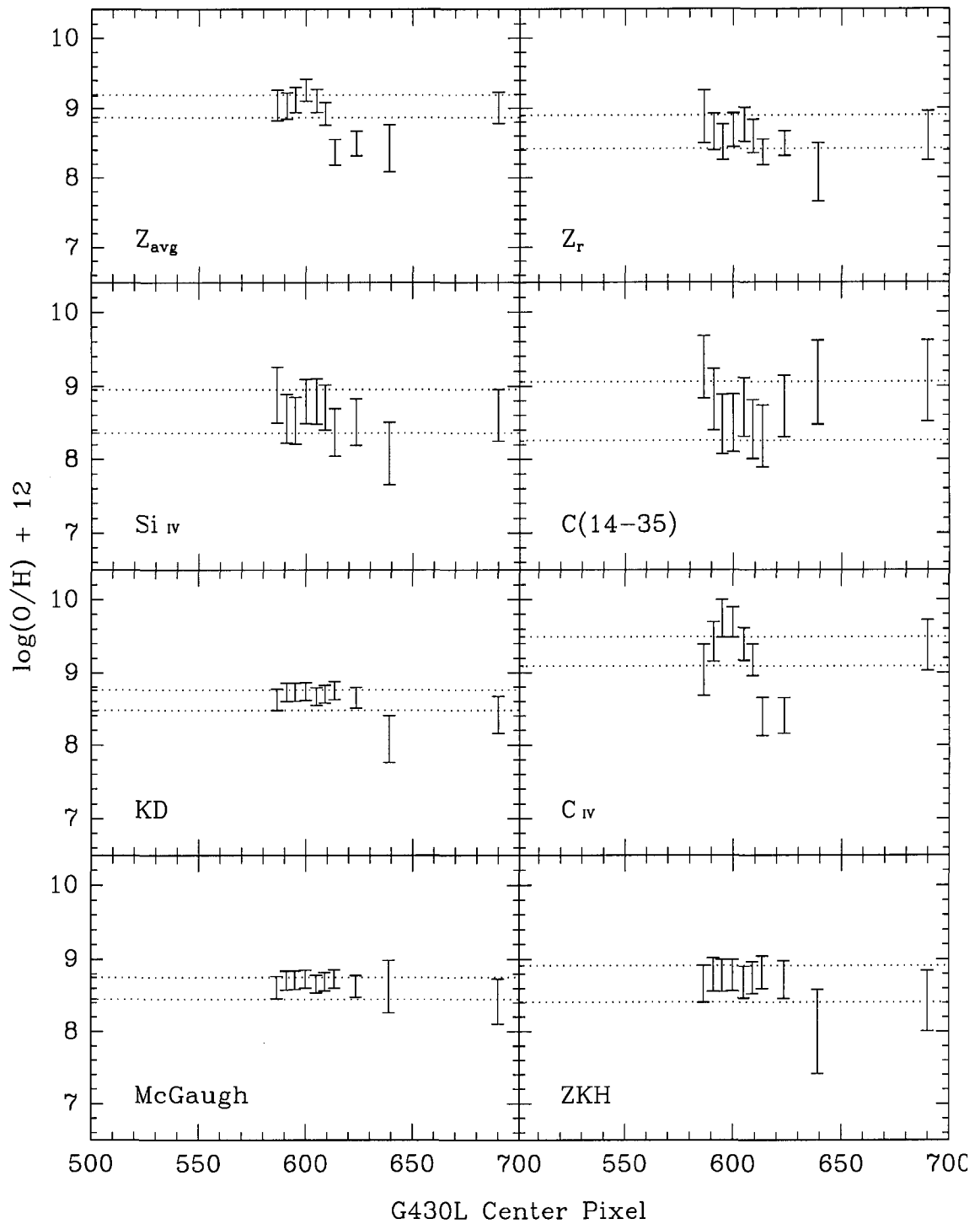
Figure 7. NGC 3395 Metallicity Errors

Each panel is labeled with the estimation technique plotted in that panel for each knot. The horizontal dotted lines are the upper and lower limits on the unresolved knot metallicity estimate for that technique.
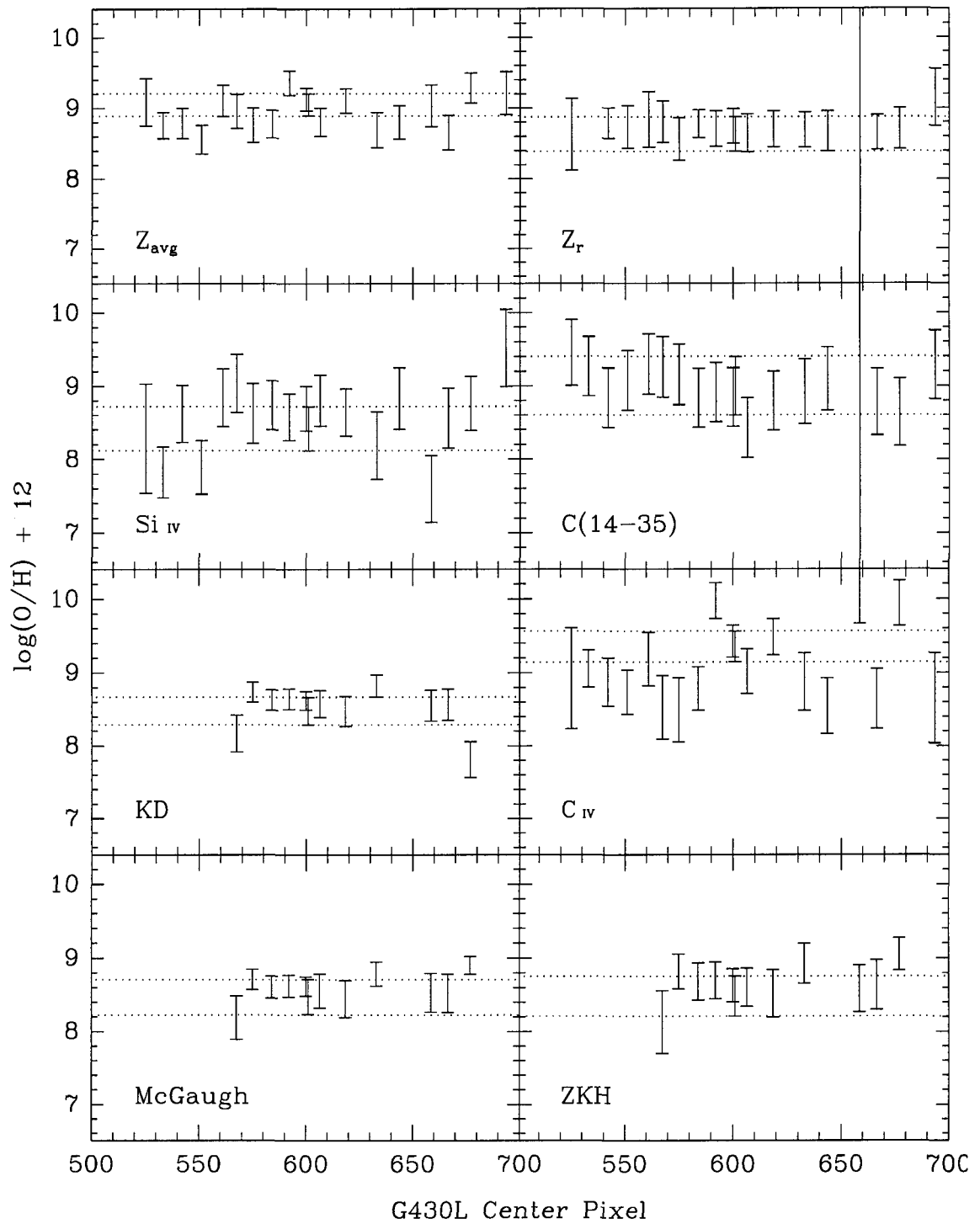
Figure 8. NGC 3396 Metallicity Errors

Each panel is labeled with the estimation technique plotted in that panel for each knot. The horizontal dotted lines are the upper and lower limits on the unresolved knot metallicity estimate for that technique.

Wolf-Rayet Star Analysis

Wolf-Rayet (WR) stars are evolved from super massive O stars that have such strong winds that layers deep into the star which contain materials that have previously been processed by nucleosynthesis are exposed. These stars are characterized by strong P Cygni absorption/emission line profiles, He II $\lambda 1640$ emission and a He II $\lambda 4686$ "bump" which is a blend of He II $\lambda 4686$ and several other lines the most prominent of which are N III/N v $\lambda 4640$ and C III/ C IV $\lambda 4650$. We observe the He II lines and have measured them in the brightest starburst knots in both galaxies.

We have adopted the conventional (Kunith and Joubert 1985; Mas-Hesse & Kunith 1991) rest frame measurement limits of 4600-4700 Å for the WR bump. This seems to fit our data reasonably everywhere, except perhaps knot Q1. In this knot it appears the emission could extend as much as 40 Å beyond 4700 Å and there may be a narrow nebular He II $\lambda 4686$ emission on top of the broad stellar emission. However, since all the literature and theory use the 4600-4700 Å we will follow the conventional limits.

There are three subcategories of WR stars, all of which show strong helium emission. WC star spectra also show strong carbon emission lines, in particular C III $\lambda 4650$ and C IV $\lambda 5808$. WN stars also show strong nitrogen emission lines, in particular N II $\lambda\lambda 4634, 4640$, N IV $\lambda 4057$ and N v $\lambda 4604$. WO stars are rarer than the other two subcategories and their spectra are similar to WC stars with the addition of strong oxygen emission lines, in particular O IV $\lambda 3400$ and O VI $\lambda 3811$.

Unfortunately all of the lines which subcategorize WR stars are weak or blended with other lines and we do not have the spectral resolution and/or SNR to isolate and measure them in our spectra, with the possible exception of N II $\lambda\lambda 4634, 4640$. Knots

R20, Q3, C3, C4 and the unresolved NGC 3396 knot do exhibit some N $\text{\tiny II}$ $\lambda\lambda$4634, 4640 emission, which combined with the presence of the WR bump and He $\text{\tiny II}$ λ1640 emission suggest the presence of WN stars. No attempt was made to deblend the nitrogen and carbon emission from the rest of the bump emission.

We begin our analysis by estimating the number of WR stars present in a knot from the luminosity in the He $\text{\tiny II}$ λ4686 WR bump. Several authors have used various luminosities to characterize the luminosity in the WR bump for a "typical" WR star, we use the Vacca and Conti (1992) value of L(4686)=1.7e36 erg/s. We use a Virgocentric inflow corrected distance of 28.3 Mpc to NGC 3395 and NGC 3396 (Hancock et al., 2003) to calculate the observed bump source luminosity. We then solved for the number of WR stars both as observed, and corrected for reddening using the Calzetti et al. (1994) reddening law.

Following estimation of the number of WR stars, we estimated the number of O stars present in the knots using the results of Schaerer & Vacca (1998, S&V hereafter). S&V have done extensive modeling and have created calibrations that predict the ratio of WR and O stars as a function of the He $\text{\tiny II}$ λ4686 WR bump/Hβ ratio as well as the equivalent width of He $\text{\tiny II}$ λ4640. Using the estimated number of WR stars, we solved the ratio for the number of O stars, both as observed as well as corrected for reddening.

While employing these estimation techniques, we encountered spurious results. These were due to the fact that we attempted to measure the equivalent width and WR bump in all the knots, regardless of whether we expected to see WR features in that spectrum based on other factors such as the strength of the UV continuum, the presence of P Cygni profiles, etc. In order to eliminate these spurious results, we empirically

demand that the WR bump be larger than its associated measurement error. For the equivalent width of He II λ1640, we empirically demand that it be at least twice its error. We placed one other restriction on the data. Examining S&V, we see that the predicted WR/O ratio diverges at log(EW(He II λ1640)) = 0.5, therefore, we do not calculate an estimate if our measured log(EW(He II λ1640)) > 0.5.

S&V caution that their calibrations are only valid for WR emission and that nebular [Fe III] λ4658 and [Ar IV] $\lambda\lambda$4711, 4740 can contaminate the measurement. We cannot rule out the presence of these contaminants, but we do note that we observe no other iron emission. In the brightest knots we do see some [Ar III] λ7136 emission, but since we limit our measurement region for the WR bump to 4600-4700 Å, any [Ar IV] $\lambda\lambda$4711, 4740 contamination is outside the region we are measuring. We therefore assess that the impact of any potential contamination is within our somewhat large error bars.

With these caveats, we obtain consistent, reasonable results which are presented in Tables XV and XVI. In the tables, column (1) is the knot's name; column (2) is the flux in the λ4686 WR bump in units of 10^{-16} erg/s/cm^2/Å and column (3) is the log of this flux divided by the flux in Hβ; column (4) is the the equivalent width of He II λ1640 in Angstroms. Column (5) is the number of WR stars estimated from the measured flux in the λ4686 WR bump uncorrected for reddening; column (6) is the same as column (5) but the flux has been corrected for reddening by the Calzetti (1994) reddening law. Columns (7, 8, 9) are based on the WR bump ratio method: column (7) is the Wolf Rayet star to O star ratio; column (8) is the number of O stars uncorrected for reddening; and column (9) is the number of O stars corrected for redding by the Calzetti (1994) reddening law.

Columns (10, 11, 12) are the same as (7, 8, 9) but determined via the He II λ1640 equivalent width method.

The last two rows in the tables are provided for comparison purposes. The second to last row is the sum of the stars in all the measurement knots, excluding the unresolved knot. The errors in this row are the measurement knot errors summed in quadrature. The last row is the the unresolved knot value minus the sum of the other knots. As can be seen, the sum of our knots is almost always within approximately one error bar of the unresolved knot, which gives us confidence in the consistency of our calculations. It also tells us that there are few WR stars in the background in the unresolved knot that are not in one of our measurement knots implying that WR stars are relatively rare, which is in good agreement with the observed scarcity of WR stars in our galaxy. Lastly, we note that our results demonstrate that the WR estimates for the unresolved knots are representative of the resolved knots of which they are composed.

It is interesting to note that the NGC 3396 deltas are a considerably smaller percentage of an error bar than the NGC 3395 estimates both as observed and for dereddened values. There are many more WR and O stars in NGC 3396 so it may just be a matter of a larger sample size, because if anything, one would expect more disagreement in NGC 3396 due to the slit placement (There is more emission in the NGC 3396 unresolved knot that is not in any of the other individual resolved knots than in NGC 3395). In the next section we will discuss the NGC 3395 data further and offer a possible explanation. We emphasize however, that since almost all the knot sums are within ~ 1 error bar of the unresolved knot the data are in excellent agreement.

Table XV. NGC 3395 Wolf-Rayet and O Star Estimates

Knot	Flux(WR)	Log (WR/Hβ)	EW He II λ1640 (Å)	N(WR)	Dered. N(WR)	WR/HΒ method $\frac{WR}{(WR+O)}$	N(O)	Dered. N(O)	EW λ1640 method $\frac{WR}{(WR+O)}$	N(O)	Dered. N(O)
C60	2.27 ±0.98	-0.61 ±0.47	---	12.86 ±5.54	14.44 ±7.04	0.23 ±0.09	41.97 ±27.23	47.14 ±32.41	---	---	---
C1	14.14 ±1.89	-0.01 ±0.45	-0.10 ±0.26	79.93 ±10.69	95.10 ±25.07	0.75 ±0.10	26.41 ±14.30	31.42 ±18.45	---	---	---
C2	4.06 ±1.21	-0.80 ±0.46	---	22.94 ±6.84	25.53 ±9.51	0.16 ±0.04	119.72 ±50.92	133.19 ±63.99	---	---	---
C3	5.44 ±1.44	-0.89 ±0.45	---	30.75 ±8.13	35.17 ±12.17	0.14 ±0.03	194.64 ±72.36	222.61 ±96.53	---	---	---
C4	4.87 ±1.25	-0.71 ±0.45	---	27.54 ±7.05	31.04 ±10.56	0.19 ±0.04	114.72 ±42.86	129.32 ±56.31	---	---	---
NGC 3395	44.34 ±13.34	-0.72 ±0.46	0.16 ±0.09	250.64 ±75.41	314.18 ±117.98	0.19 ±0.05	1082.54 ±474.98	1357.00 ±668.94	0.09 ±0.03	2686.18 ±1240.97	3367.20 ±1729.83
Knot Total	---	---	---	174.02 ±17.54	201.28 ±32.07	---	497.46 ±103.02	563.68 ±134.07	---	---	---
Delta	---	---	---	76.62	112.9	---	585.08	793.32	---	---	---

87

Table XVI. NGC 3396 Wolf-Rayet and O Star Estimates

Knot	EW He II			WR/Hβ method					EW λ1640 method		
	Flux(WR)	Log (WR/Hβ)	λ1640 (Å)	N(WR)	Dered. N(WR)	$\frac{WR}{(WR+O)}$	N(O)	Dered. N(O)	$\frac{WR}{(WR+O)}$	N(O)	Dered. N(O)
R20	5.57 ±1.52	-0.48 ±0.45	---	31.49 ±8.60	40.80 ±14.46	0.30 ±0.07	72.77 ±31.81	94.28 ±46.38	---	---	---
Q3	3.52 ±2.05	-1.14 ±0.50	0.38 ±0.14	19.90 ±11.57	25.83 ±16.08	0.08 ±0.04	221.55 ±175.55	287.53 ±236.70	0.19 ±0.09	86.42 ±73.09	112.15 ±98.10
Q2	13.53 ±1.76	-0.83 ±0.44	0.51 ±0.14	76.48 ±9.96	99.16 ±25.61	0.15 ±0.02	425.26 ±78.71	551.37 ±159.79	---	---	---
Q1	38.79 ±2.46	-0.91 ±0.44	0.57 ±0.05	219.27 ±13.92	282.19 ±65.39	0.13 ±0.01	1461.58 ±130.13	1881.00 ±451.44	---	---	---
Q30	3.86 ±1.19	-0.89 ±0.46	0.73 ±0.13	21.84 ±6.75	32.31 ±12.33	0.14 ±0.04	138.61 ±60.27	205.04 ±100.24	---	---	---
P	3.42 ±2.02	-0.25 ±0.51	---	19.35 ±11.44	25.67 ±16.39	0.47 ±0.24	21.85 ±25.04	28.98 ±33.93	---	---	---
N	2.54 ±1.92	-0.64 ±0.55	---	14.34 ±10.88	---	0.22 ±0.14	50.90 ±57.54	---	---	---	---
NGC 3396	73.32 ±12.40	-0.87 ±0.44	0.71 ±0.03	414.45 ±70.09	576.67 ±161.38	0.14 ±0.02	2537.82 ±604.46	3531.11 ±1152.04	---	---	---
Knot Total	---	---	---	402.68 ±28.21	505.96 ±76.29	---	2392.52 ±250.06	3048.20 ±546.54	---	---	---
Delta	---	---	---	11.77	70.71	---	145.3	482.92	---	---	---

Unfortunately we have very few knots with log(EW(He ɪɪ λ1640)) < 0.5, only one

per galaxy. When the EW estimate can be calculated, the WR/(WR+O) ratios are within

about a factor of two of each other, but it is a very small sample size.

Unsurprisingly, in both galaxies, the UV-brightest knots are the hub of the WR

activity. There is no apparent gradient in the number of WR stars, other than the fact that

the brighter knots have more.

In summary, we have obtained consistent reasonable results for the number of WR

and O stars using both the WR bump/Hβ and the equivalent width of He ɪɪ λ1640

calibrations of S&V. We find that the results for spatially unresolved spectra are

consistent with the results for spatially resolved spectra and therefore this technique will

provide good insight into the massive star population. This is of obvious interest at high

redshift where one cannot obtain spatially resolved spectra.

The Superbubble in NGC 3395

Knot C1 in NGC 3395 has an anomalously high WR/(WR+O) ratio of 0.75. Even

assuming that the true ratio is one error bar smaller, that is a WR/(WR+O) ratio of 0.65.

Table XII shows that the metallicity for this knot is approximately 0.5 solar. From S&V

the WR/(WR+O) ratio can go as high as 1.0 for solar and higher metallicities, so 0.65 is a

possible value. It is worthwhile to refer back to C1's spectrum (Figure 3e). Despite its

large UV flux, there is little emission in the Balmer lines. It appears that C1 is a bubble,

and has blown out most of its surrounding nebula.

In an effort to follow this line of reasoning further we consider the Balmer emission

in the knot and attempt to estimate how efficiently the gas in the knot is converting UV

flux into Balmer radiation. In Figures 9 and 10 for each knot in NGC 3395 and NGC

3396 respectively, we plot as a solid line the equivalent width of Hα as a function the

spatial center pixel of the knot in the G750L 2D spectrum. This allows us to get a sense

of the spatial gradient in the values of the equivalent width. We use the flux at 1550 Å as

a proxy for the ionizing radiation available for Balmer photon production and plot as a

dotted line $\log[EW(H\alpha)/F_{1550}]$ which we will use as an indication for the efficiency of the

recycling of ionizing photons into Balmer emission.
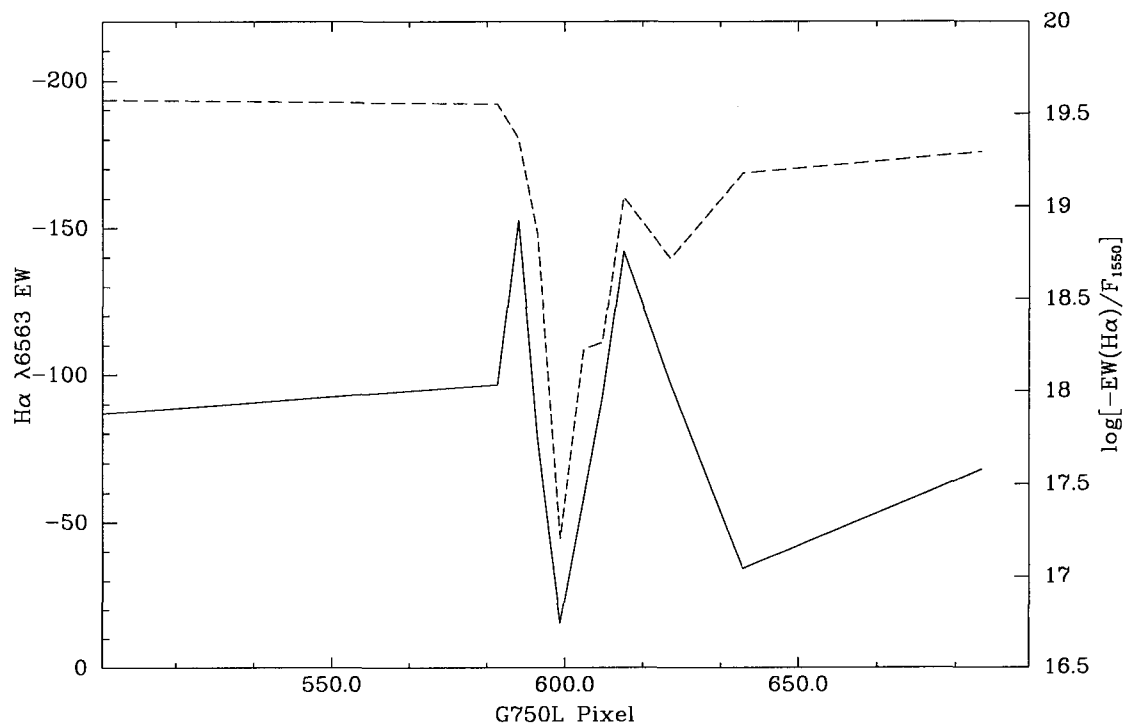
Figure 9. NGC 3395 Hα Equivalent Width and Ionizing Photon Efficiency

As can be seen, in NGC 3396 the efficiency is fairly constant regardless of

equivalent width—when the ionizing flux increases, so does the Balmer radiation, and

these knots seem to be well modeled by a radiation bounded nebula. Now examining

NGC 3395 we also see a fairly constant efficiency until knot C1 (near G750L pixel 600)

We see a dramatic drop in efficiency along with a sharp drop in the equivalent width.

The nebula is no longer turning the same proportion of UV flux into Balmer emission,

and the nebula no longer appears to be radiation bound.
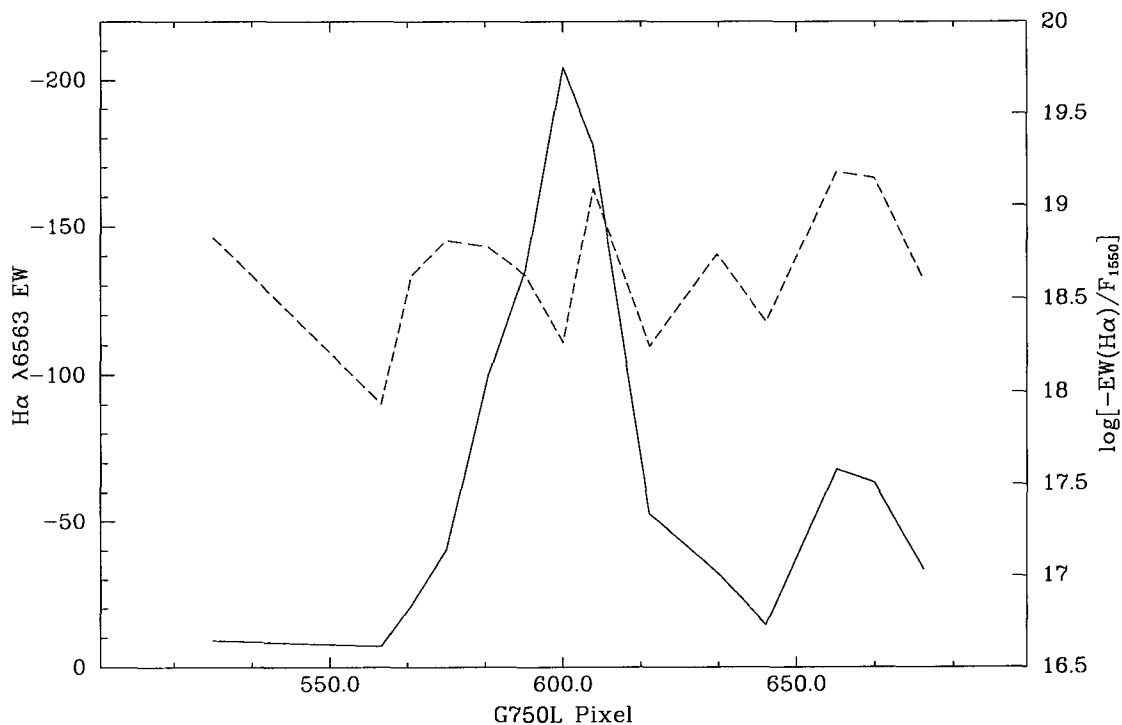
Figure 10. NGC 3396 Hα Equivalent Width and Ionizing Photon Efficiency

The Hα emission is reduced since there is little to no hydrogen in the region and

thus much of the UV radiation escapes without being converted into Balmer emission.

Hβ emission will be reduced for the same reason and the reduced Hβ emission will

increase the ratio of WRbump/Hβ, thus driving us to a higher WR/(WR+O) ratio. S&V

assumed radiation bounded nebulae, which clearly does not appear to be the case here, so

our results for knot C1 are suspect. Specifically, we have almost certainly overestimated

the WR/(WR+O) ratio. If so, we will underestimate the number of O stars. This O star

deficit is further confirmed by the large difference between the sum of the number of O

stars in the measurement knots and the NGC 3395 unresolved knot in Table XV. Since C1 has the most WR stars of any knot in NGC 3395, if we overestimated the WR/(WR+O) ratio, we will have a proportionally greater number of O stars.

The spatial extent of knot C1 is 7 pixels in the G430L data. This corresponds to 0.35" which projected out to 28.3 Mpc is a diameter of 48.0 pc or a radius of ~ 24 pc. In the age estimation section we will calculate the best fit model age of the spectrum as 5 Myr. An order of magnitude estimate of the velocity of the stellar wind that would be required to evacuate a 24 pc = 77.76 lyr bubble in 5 Myr is ~ 5 km/s. Typical WR stellar winds are a few hundred to a few thousand km/s, so a bubble of this size is easily achievable within the time scales involved.

Strickland & Stevens (1999) have observed the starburst galaxy NGC 5253 with ROSAT and found X-ray emission from a complex of multiple WR bubbles. This sort of wind driven bubble around WR stars has been discussed by Miller and Chu (1993). They defined these so-called "W-type" shells and found that they tend to be 10-20 pc in radius. Bransford et al (1999) measured the bubbles around 24 WR stars in M31 and found they had bubbles typically ≤ 40 pc diameter which compares well with our bubble. Our values also compare well with the results of Rizzo & Martin-Pintado (2001) who determined that the optical nebula NGC 2359 contains a 50pc bubble expanding at 12 km/s around a single WR star, HD 56925. Therefore our values are reasonable and well within the accepted values for superbubbles.

Assuming C1 is a bubble, and the extreme WR stellar winds do not disrupt O star formation, then we will have overestimated the WR/(WR+O) ratio. To assess the potential impact of this overestimation, we examine the next three UV-brightest knots in NGC 3395: C2, C3 and C4 which are all very similar chemically to C1 with all four knots

having metallicities ~0.6 $Z_\odot$. The average WR/(WR+O) ratios of C2, C3 and C4 is 0.16 which, if applied to the observed number of WR stars in C1, would yield ~420 O stars uncorrected for reddening. This in and of itself would account for over 70% of the difference between the sum of the number of O stars in the knots and the number of O stars in the unresolved knot, bringing these numbers to well within one error bar of each other.

The spectra indicate that C1 is a bubble and order of magnitude calculations demonstrate that a bubble of this magnitude is reasonable. Furthermore, if C1 were a bubble it would account for the observed disparity between the number of O stars in our measurement knots and in the unresolved knot. We therefore conclude that C1 is a bubble.

Starburst 99 Fitting Tools

The ages of the starburst knots were estimated using the Leitherer et. al. (1999)

Starburst 99 (SB99) spectral synthesis models. The models use a variety of template

stellar spectra and compute synthetic spectra for starburst knots based on Initial Mass

Function (IMF), upper mass limit, starburst type, metallicity, and age.

The IMF characterizes the number N(M) of stars with mass M as a power law with

exponent value, α, according to the formula

$$N(M)dM \propto \left[\frac{M}{M_\odot}\right]^{-\alpha} dM \qquad (6)$$

The models then create synthetic spectra for populations described by this

distribution. The SB99 models use a lower mass limit of 1 $M_\odot$ and an upper limit for star

formation of either 30 $M_\odot$ or 100 $M_\odot$.

Previously we found that there are WR stars present in our knots which places

constraints on the IMF lower mass limit. Kudritzki et. al. (1989) have shown that the

mass loss rate from a Wolf-Rayet star is proportional to $M/Z^{1/2}$ where M is the mass and

Z is the metallicity. This mass loss rate drives the lower mass allowed for a Wolf-Rayet

star to develop. Maeder (1998) as reported by Foellmi et al. (2003) estimated the lower

mass limits of WR stars for the Milky Way as 25 $M_\odot$, 35 $M_\odot$ for the LMC, and 45 $M_\odot$ for

the SMC. The metallicity for our knots is ~0.5-0.6 $Z_\odot$ which would place the lower limit

at approximately 35 $M_\odot$. Furthermore, since WR stars are thought to be evolved Of stars,

which typically have masses 2-4 times as great, the lower mass limit is clearly well

beyond 30 $M_\odot$. Based on these results, we do not employ models with an upper mass

limit of 30 $M_\odot$.

The models are created assuming that starbursts come in two generic types,

instantaneous and continuous. In an instantaneous starburst, all the stars are formed at

once with no further star formation. In a continuous starburst, stars are continually

formed. The models are also created with metallicities of Z=0.040, 0.020, 0.008, 0.004,

and 0.001 where solar metallicity is Z=0.020. Since we know the metallicity from our

previous analyses, we use the model with the closest metallicity to our value. Most of

our knots have metallcities ~0.5-0.6 $Z_\odot$ so our knot metallicities are well represented by

the models.

Age estimation was performed employing two types of model spectra, a continuum

model and a UV feature model. The continuum models compute synthetic spectra from

stellar evolution models via isochrone synthesis over a broad wavelength regime from the

extreme UV (100 Å) out to the far IR (160 μm) both for the case where the stars are not

embedded in a nebula ("Stellar only") and for the case where the stars are embedded in a

nebula ("Stellar + Nebular"). While the continuum models have line absorption and

continuum emission taken into account, the UV feature models are created from IUE

template spectra and thus provide more detailed models of the UV portion of the

spectrum with special emphasis on the stellar absorption. Table XVII describes the

models that were considered. Column (1) is the figure number from Leitherer et al

(1999); column (2) is the type of model: continuum or UV feature (for models with

various metallicities, the appropriate model was used based on our metallicity estimates);

column (3) is the Initial Mass Function given as the power law exponent value, α, and the

upper limit for star formation; column (4) is the type of starburst: instantaneous or continuous.

In general, from the observations it is difficult to differentiate among all the parameters that effect the models, such as age, metallicity, IMF, type, and reddening. Furthermore, many of these parameters, such as age and reddening, produce similar effects in the model. To resolve some of these difficulties, we use the reddening we calculated in the previous sections to constrain the problem and reduce the number of variables. In the analyses that follow, we use two types of fitting tools: UV feature fitting and continuum fitting.

Table XVII Starburst 99 Model Parameters

No.	Model	IMF	Type
1	Stellar + Nebular Continuum	$\alpha=2.35$, 100 $M_{\odot}$	Instantaneous
2	Stellar + Nebular Continuum	$\alpha=2.35$, 100 $M_{\odot}$	Continuous
3	Stellar + Nebular Continuum	$\alpha=3.30$, 100 $M_{\odot}$	Instantaneous
4	Stellar + Nebular Continuum	$\alpha=3.30$, 100 $M_{\odot}$	Continuous
7	Stellar Only Continuum	$\alpha=2.35$, 100 $M_{\odot}$	Instantaneous
8	Stellar Only Continuum	$\alpha=2.35$, 100 $M_{\odot}$	Continuous
9	Stellar Only Continuum	$\alpha=3.30$, 100 $M_{\odot}$	Instantaneous
10	Stellar Only Continuum	$\alpha=3.30$, 100 $M_{\odot}$	Continuous
13	UV Feature	$\alpha=2.35$, 100 $M_{\odot}$	Instantaneous
14	UV Feature	$\alpha=2.35$, 100 $M_{\odot}$	Continuous
17	UV Feature	$\alpha=3.30$, 100 $M_{\odot}$	Instantaneous
18	UV Feature	$\alpha=3.30$, 100 $M_{\odot}$	Continuous

UV Feature Fitting Technique

To estimate the age via the UV features, the observed spectra were compared to several synthetic UV spectra produced by SB99. Because we expect the UV spectra to be severely reddened, we chose to use the rectified (continuum normalized to 1.0) SB99 spectra. This removes the UV color dependence (and hence the reddening dependence) of the fit answer.

We prepared the observed spectra as follows. First, we blueshifted them back to the rest frame and corrected them for extinction using the Calzetti et. al. (1994) reddening law. Calzetti et al. (1994) have shown that the continuum reddening in star forming galaxies is half that determined from emission lines therefore a value of half the Balmer optical depth as determined by the emission line ratio of $H\alpha/H\beta$ from Tables V and VI was used as the reddening coefficient. Following the blueshifting and dereddening, we continuum normalized the UV spectra by fitting the UV continuum with the IRAF task CONTINUUM and dividing it out. For the purpose of the continuum normalization, fourth order Legendre polynomial fits were performed in the combined region 1260-1690, 1265-1285, 1340-1370, 1410-1500, 1560-1630, and 1645-1690 Å (to avoid geocoronal Ly α emission and regions of strong absorption), the excluded regions being masked out. Each point in the masked spectrum was replaced by a running 3 sample median and any points more than 1 standard deviation away from the global mean (the mean of all the masked spectrum data points) were rejected.

Following preparation of the data, we prepared the models. In order to compare the data to the models, the fitting routine must have values for both the data and the model at the same wavelength. Therefore we used the STSDAS task CALCSPEC to create custom model spectra for each starburst knot. For each wavelength entry in the knot

data, CALCSPEC interpolated the model flux values. The result was a model table with the same number of rows as the knot data table and with identical wavelength columns.

Following preparation, the data and the models were compared using the STSDAS routine FITSPEC which fits via χ^2 minimization. For the UV spectra the features of particular interest are defined in Table XVIII. In the table, column (1) is the name of the feature; column (2) is the rest frame wavelength of the feature in Angstroms; and column (3) is the weighting assigned to the feature. Because these features are more significant for age estimation than the rest of the spectrum, we created a weighting scheme in order to simultaneously fit all the features while allowing certain features to have a higher significance. The weightings range from 0 (least significant) to 10 (most significant). We adjusted the weightings until the software consistently produced acceptable fits in the regions of interest.

Table XVIII. UV Feature Definitions

Feature	Wavelength Range (Å)	Weight
Continuum	<1208	Excluded
Geocoronal Ly α	1208-1220	Excluded
N v λ1240	1220-1250	2
Si iv λ1403	1370-1410	5
C iv λ1550	1500-1560	5
He ii λ1640	1630-1650	1
Continuum	All other UV wavelengths	1

We use the weightings to adjust the error bars of the data which are then used by the χ^2 fitting routine to determine the best fit. To each error bar e_i we assign a weighted error σ_i as follows

$$\sigma_i = e_i/w \tag{7}$$

where w is the weight for the wavelength region in question from Table XVIII. The χ^2

value for each data point f_i with weighted error σ_i, and model fit value F_i is defined by

$$\chi_i^2 = \frac{(f_i - F_i)^2}{\sigma_i^2} \tag{8}$$

Notice that the more highly weighted regions have smaller proportional weighted

errors which cause larger χ^2 values for a given difference between the data and the model.

Since the best fit has a minimal χ^2 value, we preferentially select models that are in better

agreement in the regions we deem more significant. Said another way, we are willing to

accept a worse fit in some portions of the spectrum in order to get a better fit in the

regions of interest where it matters most. This approach is justified by two factors:

1. The spectra are continuum normalized, so slope/color comparison is not

   relevant. Therefore the non-feature regions outside the regions of interest tell us

   little about the age of the starburst and so weigh less in the final answer. Note

   for the fitting routine to reliably converge, we have to include the UV

   continuum, even though it tells us little.

2. The spectral regions selected are indicative of hot, massive stars. The models

   are based on stellar spectra, but the rest of the UV continuum can be (and

   frequently is) contaminated by significant interstellar absorption lines. Since we

seek to model the stars, not the interstellar media, it is reasonable to inflate the significance of the stellar features and reduce the significance of the interstellar features.

Hot, young stars have strong winds which generate P Cygni profiles in C iv $\lambda1550$ and Si iv $\lambda1403$ so these features are highly weighted. N v $\lambda1240$ is sensitive to star formation too; however in our data, this region is severely contaminated by geocoronal Lyman alpha emission, so it is weighted lower than the other features. In principle He ii $\lambda1640$ should be highly weighted too as it is sensitive to hot massive stars, particularly WR stars. However, we found that the SB99 models consistently underestimate the He ii emission when compared to our data so we have less confidence in the fidelity of the models in this region.

The fits were performed with a simple two parameter model. We allowed for a flux scaling (multiplicative) factor for each model to allow the fitting routine to scale the depth of the absorption below the normalized continuum. This parameter doesn't have any physical significance but rather exists to allow the fitting routine to tweak the model to fit the data. Similarly, even though both the spectra and the models were at zero redshift, we further defined an additional blueshift to allow for small errors in the blueshifting to the rest frame. We did this because both the UV model and observed spectra are feature-rich and small differences in blue shifting can impact the quality of the fit. We expect the additional blue shift parameter to be small in comparison to the overall blueshift of 5.4×10^{-3}, and we find typical values of $\pm 1 \times 10^{-4}$ for this parameter.

Occasionally, a knot will have large error bars associated with its spectral data, particularly if the knot is weak. Since χ^2 fitting attempts to minimize the number of error

bars that our model is away from the data, attempting to fit data with large error bars can result in poor fits, even though the χ^2 is small. To rectify this situation, we also calculated the RMS between the model and the data and disregard any fit which exceeds our RMS limit. Since both the UV models and the UV data were normalized to 1.0, we use a UV RMS limit of 0.2.

Using the above criteria, we calculated our UV fits. In general, the fits were subjectively very good and had low RMS; however, there were some shortcomings that warrant mention. In the brightest, youngest knots, the SB99 models underestimate the depth of the P Cygni absorption and neglect or underestimate the emission component of the P Cygni lines. For example, Q1, the brightest knot in NGC 3396 is shown as a thin line and the best fit to it is shown as a heavy line in Figure 11. The best fit is to an 8 Myr old continuous starburst model with IMF of α=2.35 and an upper mass limit of 100 M$_\odot$. While this is a pretty good fit overall, notice how the depth of the C IV λ1550 and Si IV λ1403 absorption are not quite matched. Also the C IV λ1550 emission is grossly underestimated. Unlike the exclusively stellar C IV λ1550 and Si IV λ1403 lines, the sharp absorption features at 1260, 1300 and 1335 Å are a mix of stellar and interstellar lines. Since the exact mixture of the stellar and interstellar components is unknown, both in our data and in the IUE data which make up the SB99 UV feature models, we will not address any disagreement between our data and the models in these regions.
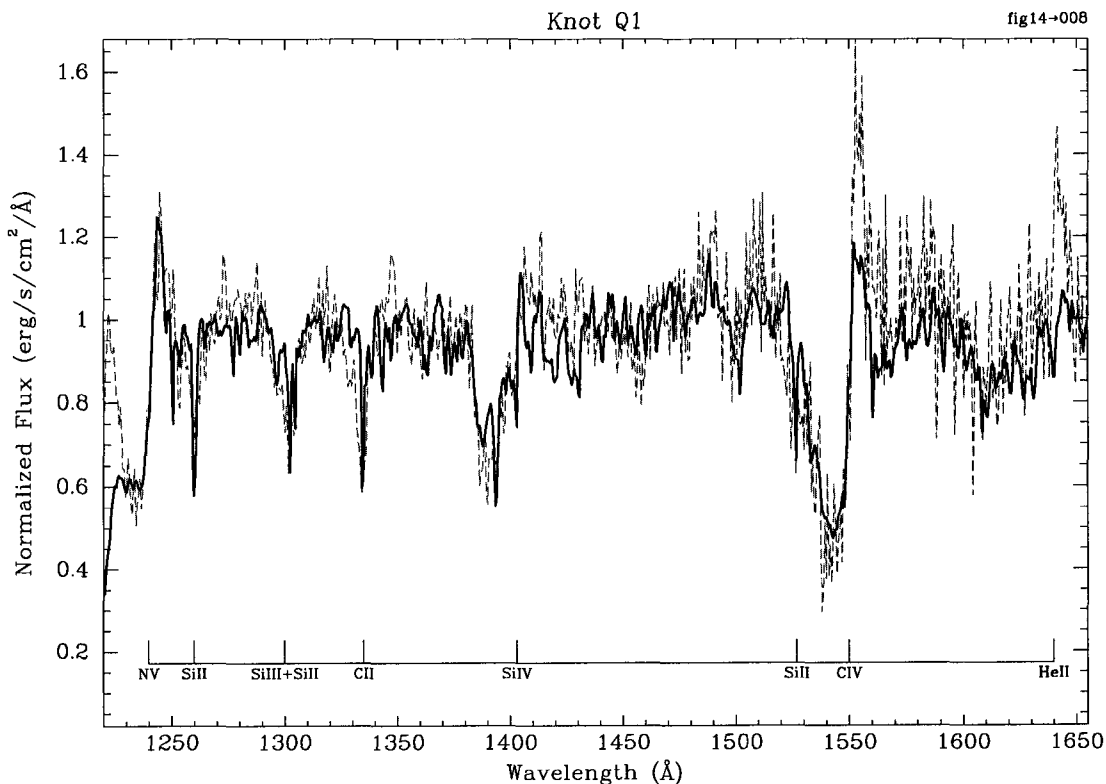
Figure 11 Best UV Feature Fit to NGC 3396 Knot Q1 with Solar Metallicity

The heavy line is the 8 Myr old continuous starburst model with solar metallicity and an α=2.35 IMF with an upper mass limit of 100 $M_\odot$. The thin line is the observed data

SB 99 comes with UV models for solar metallicity only, while the metallicity for

this knot is 0.5 $Z_\odot$. We sought to assess whether the observed shortcomings are due to

the metallicity difference between the model and the data. On the SB99 web site at

http://www.stsci.edu/science/starburst99/ one can run custom models with several

options. For the UV feature spectra one can calculate custom models either for Solar

metallicity, or Large Magellanic Cloud (LMC) metallicity (Z ~ 0.4 $Z_\odot$). We created

some custom models and evaluated them against the spectrum. The best fit is shown in

Figure 12. In this case, the best fit is a 4 Myr old instantaneous starburst with IMF of

α=3.30 and an upper mass limit of 100 $M_\odot$. Notice the deficits are even worse. This is to

be expected, since P Cygni lines are a result of atoms in the stellar wind, so decreasing

the metallicity should decrease the observed P Cygni characteristics and, in fact, it does

in the model. Note that the metallicity as determined by emission lines for this knot is

0.5 $Z_\odot$ therefore it would seem that the UV features are more consistent with a higher

metallicity than the nebular gas predicts. This may be a fruitful venue for future research.
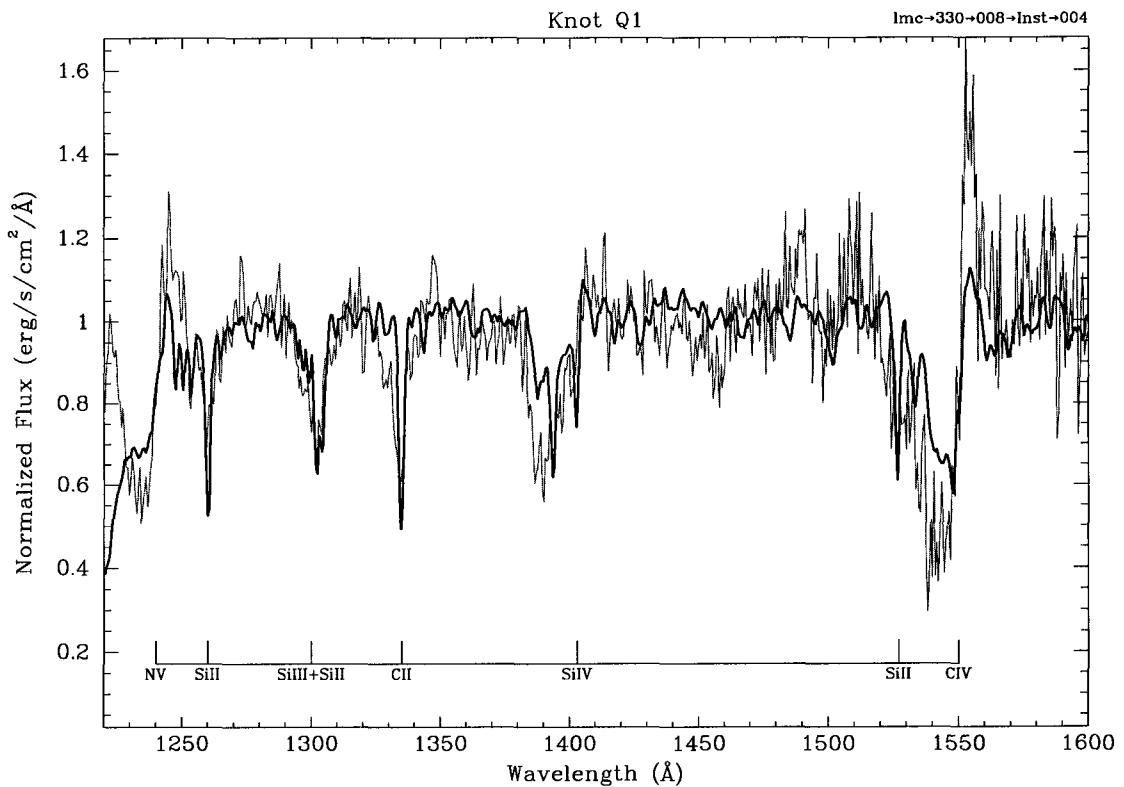
Figure 12 Best UV Feature Fit to NGC 3396 Knot Q1 with LMC Metallicity

The heavy line is the 4 Myr old instantaneous starburst model with 0.4 solar metallicity and an α=3.30 IMF with an upper mass limit of 100 $M_\odot$. The thin line is the observed data. The LMC models only go to 1600 Å.

Continuum Fitting Technique

The continuum fit process closely resembles the UV feature process except the data and models were prepared differently. The continuum fit process basically is a color process where one is concerned about relative magnitude of flux at a given wavelength compared to the flux at another wavelength. As such, the SB99 models are not continuum rectified, so neither are the starburst knots. Both the data and the models were; however, normalized by their median flux value because the numbers involved are very large (flux~10^{35} erg/s/cm^2/Å). Without normalizing by some reasonable number (we chose the median, but our choice is arbitrary) we get round off errors and the software experiences solution conversion problems. We also normalize to account for differences in the total number of stars. The SB99 models are normalized to 10^6 M$_\odot$ for instantaneous starbursts and 1 M$_\odot$ per year for continuous starbursts, which while reasonable values, are almost certainly not what we are actually observing. Following the median normalization, the observed data were blueshifted to the rest frame to ease wavelength region definition. The data were not corrected for extinction.

The models were prepared using CALCSPEC as discussed in the UV feature section, but in addition to interpolating the model data at each knot spectrum data wavelength, CALCSPEC reddened the model data using the Calzetti et. al. (1994) interstellar extinction law. A value of half the Balmer optical depth as determined by the emission line ratio of Hα/Hβ from Tables V or VI was used as the reddening coefficient (Calzetti et. al. 1994). Since the observed data were shifted to the rest frame, the models were left in the rest frame as well.

Table XIX. Continuum Definitions

Feature	Wavelength Range (Å)	Weight
Continuum	<1208	Excluded
Geocoronal Ly α	1208-1220	Excluded
N v λ1240	1220-1250	Excluded
Si iv λ1403	1370-1410	Excluded
C iv λ1550	1500-1560	Excluded
He ii λ1640	1630-1650	Excluded
UV Continuum	1410-1500 + 1560-1630	2
[O ii] λ3727	3675-3775	Excluded
[O iii] λ4363	4310-4410	Excluded
[O iii] λ4959,5007	4925-5050	Excluded
Hβ λ4861	4825-4900	Excluded
Balmer Decrement Region	3000-3675 + 3775-4310	Excluded
Visible Continuum	4410-4825 + 4900-4925 + 5050-5500	1
Hα λ6563 + [N ii]$\lambda\lambda$ 6548,6583 + [S ii] $\lambda\lambda$ 6718, 6732	6463-6800	Excluded
[Ar iii] λ7136	7015-7205	Excluded
Far Red Continuum	5500-5835 + 5935-6463 + 6800-7015 + 7205-9000	1
[S iii] $\lambda\lambda$ 9069,9531	> 9000	Excluded

Following preparation, the data were assigned weighted errors in the manner described previously. The weights are given in Table XIX. As before, column (1) is the name of the feature; column (2) is the rest wavelength range of the feature in Angstroms; and column (3) is the weight of the feature. Note in this instance, we exclude the features and keep the continuum, the opposite of the UV feature method. To set the weights we evaluated the continuum fit of the brightest knot in each galaxy (C1 in NGC 3395 and Q1

in NGC 3396). We explored several different permutations of the weights and evaluated

them empirically by demanding that they produce acceptable fits. We weight the UV

continuum the highest because it should be most sensitive to the presence of hot young

stars.
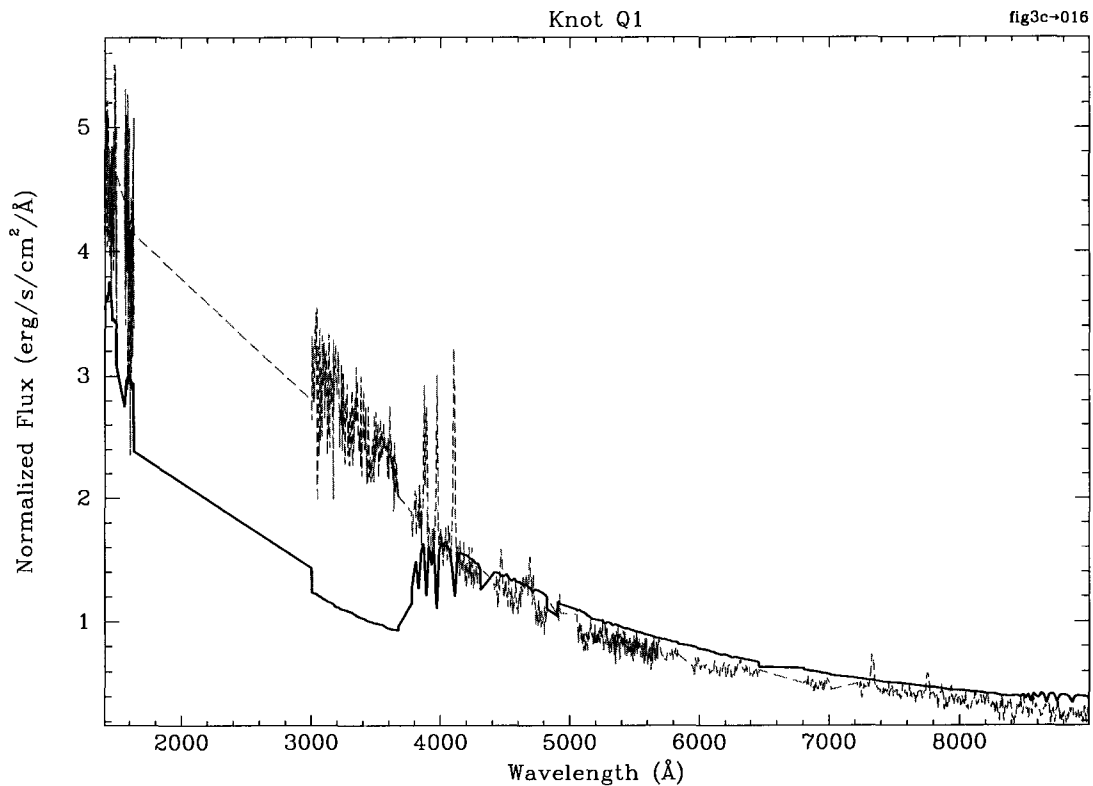
Figure 13. Best fit to NGC 3396 knot Q1 when Balmer region included

The heavy line is the 16 Myr old instantaneous starburst stellar + nebular model with 0.4 solar metallicity and an α=2.35 IMF with an upper mass limit of 100 $M_\odot$. The thin line is the observed data

The fits were performed with a simple one parameter model. We defined a

multiplicative flux scaling factor for each model, which effectively allows us to scale the

spectrum for the total number of stars present while keeping the relative stellar mass

proportions the same. We did not define an additional redshift parameter for two reasons.

First, the models are relatively smooth and featureless, as befits continua, therefore we

expect very small tweaks to the redshift not to be useful. Second, when the redshift is

allowed to vary, the models can converge to aphysically large redshifts since inconsequential feature may drive the convergence. We initially included the Balmer decrement region of the spectrum in our fits, but we ran into a problem while performing the fits. The underlying stellar population should have an <u>absorption</u> discontinuity (step up with increasing wavelength) at 3646 Å, for stellar types later than O; however we expect the nebular continuum to have an <u>emission</u> discontinuity (step down with increasing wavelength) at ~3646 Å (Osterbrock, 1989). The SB99 models have an absorption discontinuity (step up with increasing wavelength) at ~3646 Å implying the stellar continua dominate the nebular continuum emission in the Balmer region. The SB99 models do not take into account nebular emission lines, but in the stellar + nebular models, Leitherer, et al. (1999) do attempt to recycle the far UV photons short of 912 Å into continuum nebular photons. The wavelength distribution of these photons is undocumented, but regardless of the distribution that was used, the SB99 models are a very poor fit to the data near the Balmer discontinuity. For example, Figure 13 shows the best fit to the Q1 knot, the brightest knot in NGC 3396, if we include the Balmer region (for this fit, the weight of the Balmer region is 1.0).

The disagreement in the higher Balmer emission lines near 4000 Å is a known shortfall of the SB99 model (it doesn't include nebular emission lines), but neglecting this, notice the poor correlation between the model continuum and the data in the Balmer region between 3000-4000 Å. If we were to increase the weight of the Balmer region, we could force the fit to be acceptable in this region at the cost of completely missing the UV continuum as shown in Figure 14 (for this fit, the weight of the Balmer region is 10.0).

Now the fit is acceptable in the Balmer discontinuity region, but is totally unacceptable in the UV region. Both Figures 13 and 14 are fit by the same instantaneous

starburst model, only with a 12 Myr difference in age. Forcing the fit to be acceptable in the Balmer region drives us to a significantly bluer, younger solution.

One possible explanation for the disparity is reddening. If the UV continuum in our model data were insufficiently reddened relative to the visible and far red, then it could manifest itself in this way. The Calzetti (1994) reddening law used is greyer than the standard Seaton Milky Way reddening law, which agrees with the observed deficiency.
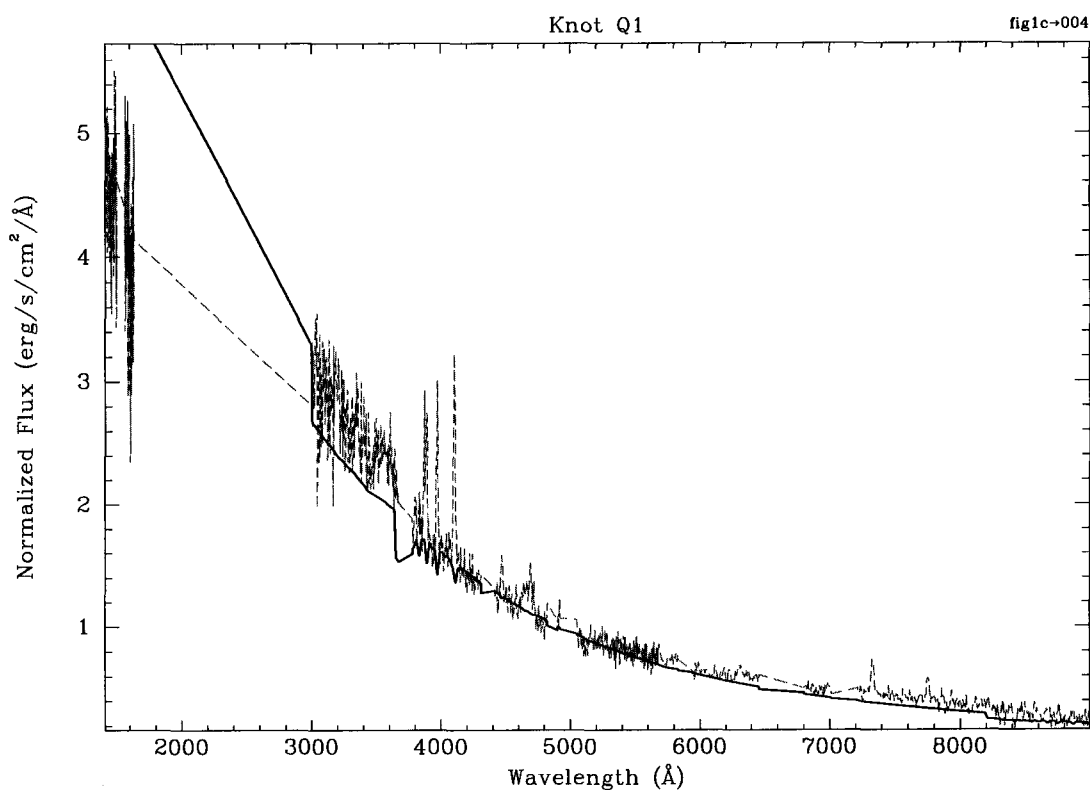
Figure 14. Best fit to NGC 3396 knot Q1 when forced to fit Balmer region

The heavy line is the 4 Myr old instantaneous starburst stellar + nebular model with 0.4 solar metallicity and an $\alpha=2.35$ IMF with an upper mass limit of 100 $M_\odot$. The thin line is the observed data.

In an attempt to resolve this disparity, we calculated the expected nebular Balmer discontinuity from the strength of the Balmer emission lines (Osterbrock 1989).

Assuming a reasonable value for the electron temperature of 10,000K, theory predicts the

ratio of the continuum emission coefficient at 3646 Å to the continuum emission

coefficient at Hβ, $j_v(3646)/j_{H\beta} = 1.89 \times 10^{-14}$ erg/s/cm²/Hz. We convert this to Å⁻¹ as

follows:

$$\frac{j_v(3646)}{j_{H\beta}}[\mathring{A}^{-1}] = \frac{j_v(3646)}{j_{H\beta}}[Hz^{-1}] * \frac{\partial v}{\partial \lambda} \qquad (9)$$

Using,

$$v = c/\lambda \qquad \qquad \partial v = \frac{-c}{\lambda^2}\partial \lambda \qquad (10)$$

We obtain

$$\frac{j_v(3646)}{j_{H\beta}}[\mathring{A}^{-1}] = \frac{j_v(3646)}{j_{H\beta}}[Hz^{-1}] * \frac{c}{\lambda^2} = 1.89x10^{-14} * \frac{3x10^{18}}{3646^2} = 4.26x10^{-3} \qquad (11)$$

In knot Q1 we measure, $j_{H\beta} = 3.16 \times 10^{-14}$ erg/s/cm² which implies our Balmer

discontinuity should be on the order of $4.26 \times 10^{-3} \mathring{A}^{-1} * 3.16 \times 10^{-14}$ erg/s/cm² $= 1.35 \times 10^{-16}$

erg/s/cm²/Å. In Figure 15 we show the an expanded view of the Balmer discontinuity

region for knot Q1. From the figure, the value of the continuum at 3646Å is ~5.0×10^{-17}

erg/s/cm²/Å and the discontinuity is only approximately 1×10^{-17} erg/s/cm²/Å . The

measured discontinuity is almost an order of magnitude less than the theoretical

prediction.

One possible cause of the observed disparity between the theoretical and actual

discontinuity is underlying stellar absorption. We predict 1.35×10^{-16} erg/sec/cm²/Å but

only observe 1×10^{-17} erg/sec/cm²/Å so we seek to determine if stellar absorption could

account for the $\sim 1.25 \times 10^{-16}$ erg/sec/cm²/Å deficit. In order to make an order of magnitude

estimate of the reasonableness of this assumption, we will estimate the number of stars

that would be required to produced the observed discontinuity deficit. For the basis of

this estimate, we will assume that all the deficit comes from A0 V stars. This spectral

class of stars has the most pronounced stellar absorption in the region of interest. We

will use Vega as a template for these stars.
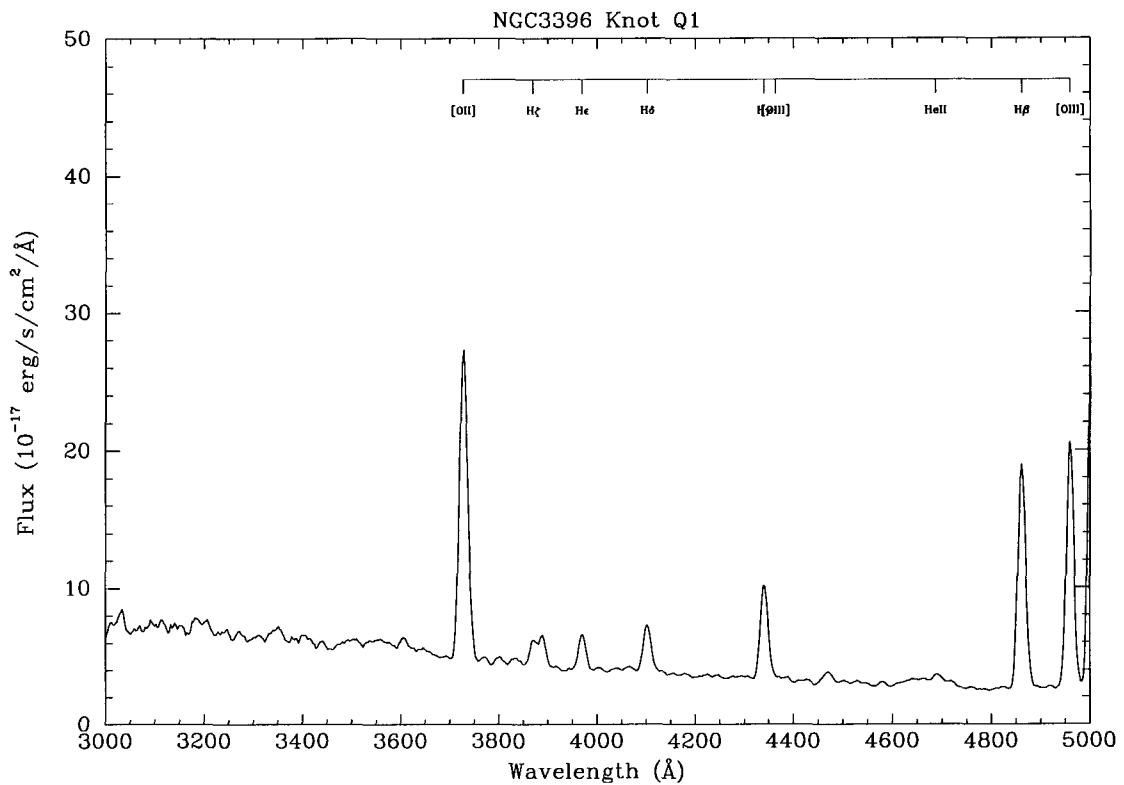
Figure 15. Expanded Balmer discontinuity region for knot Q1, NGC 3396

A spectrum of Vega is shown in Figure 16 from the HST calibration archive. From

the figure we estimate the stellar absorption to be 5.0×10^{-9} erg/sec/cm²/Å at the Balmer

discontinuity. Vega is 8.1 parsecs away from Earth (Zeilik, 1992), and NGC 3396 is

approximately 28.3 Mpc away (Hancock et al., 2003). Projecting to 28.3 Mpc, each A0

V star provides 4.09×10^{-22} erg/s/cm²/Å of absorption as observed from Earth. We redden

this value by using E(B-V) = 0.29 which is half the value from Table VI (half for the

continuum instead of emission lines) and obtain 2.56×10^{-22} erg/s/cm²/Å. Then to account

for the observed 1.25×10^{-16} erg/sec/cm²/Å absorption, we need ~488,300 A0 V stars.

While this is a lot of stars, we predict (see Wolf-Rayet section) that uncorrected for dust

absorption there are 1400 O stars in the Q1 knot.
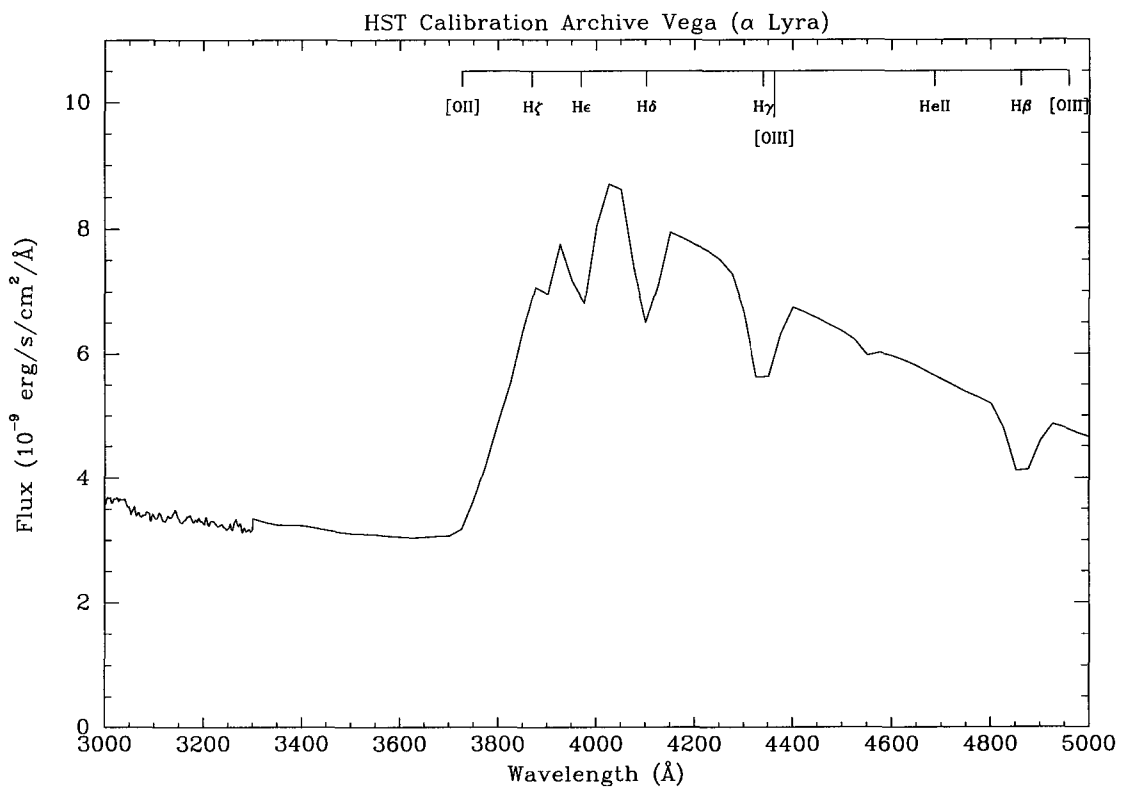
Figure 16. Vega spectrum

We estimate how many A0 V stars there are by using a Saltpeter IMF ($\alpha = -2.35$).

In Appendix A, with this IMF we calculate the average mass of an O star to be 30.2 $M_\odot$.

From Drilling and Landolt (1999), the average mass of a typical A0 V star is ~ 2.9 $M_\odot$.

Then with a Saltpeter IMF, the expected ratio of the number of O stars to A stars is

$\sim(30.2/2.9)^{2.35}$ = 246, so with 1400 O stars, we expect ~345,000 A0 stars. This is well within our order of magnitude estimate. Therefore our assumption that continuum emission overlying stellar absorption is the cause for the disparity between the data and the models is reasonable. The Balmer region values in our data are reasonable, but the UV continuum cannot be reconciled with the optical and far red continuum using the measured reddening. In an effort to gain insight into the stellar ages, we choose to ignore the visible continuum shortward of 4310 Å in our age fits to avoid these problems. The best fit to Q1 when we ignore the Balmer continuum is shown in Figure 17.
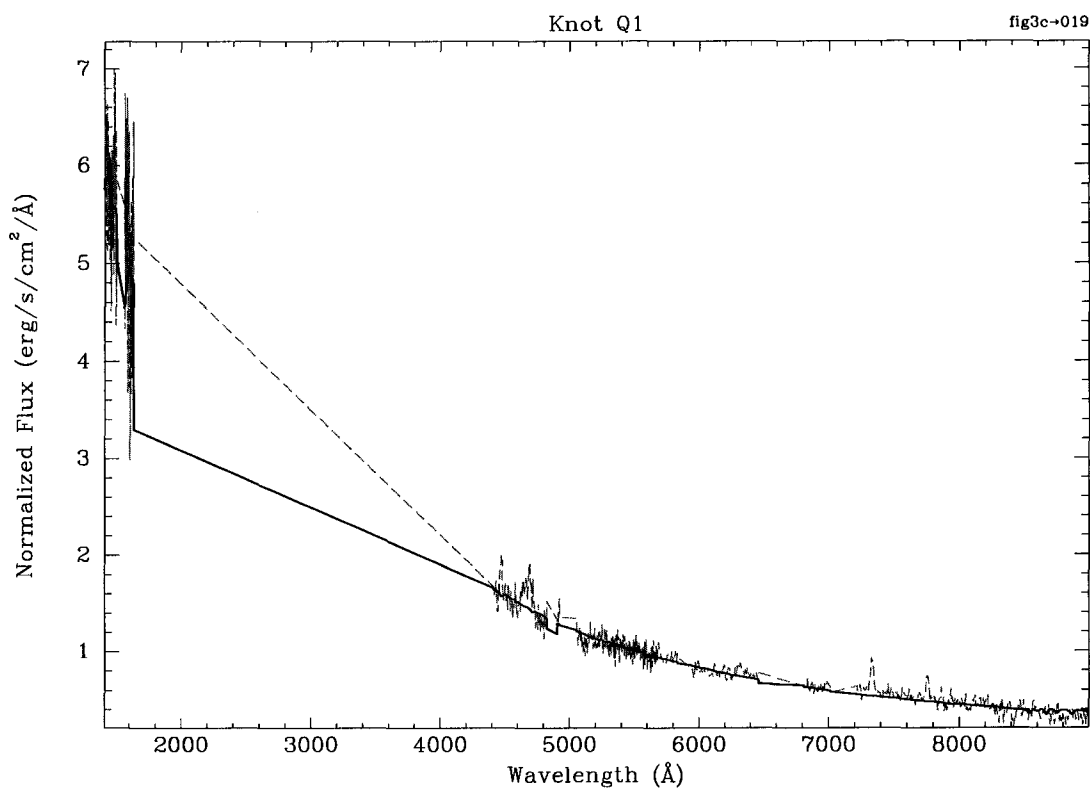
Figure 17 Best fit to NGC 3396 knot Q1 when Balmer region discarded

The heavy line is the 19 Myr old instantaneous starburst stellar + nebular model with 0.4 solar metallicity and an α=3.30 IMF with an upper mass limit of 100 $M_\odot$. The thin line is the observed data.

While the fit that ignores the Balmer region is a much better fit in the other regions

of interest, we must keep in mind the quality of the overall fit to the entire data set, shown

in Figure 18. In this figure we have also overplotted the Johnson UBVRI filters to

facilitate a later discussion in the age estimation section. As can be seen, the fit is very

poor in the Balmer region. We will return to this theme in the age estimation section. It

is because of the overall quality of the fit that we consider IMF's, starburst types and ages

derived via the continuum fitting method to be less reliable.
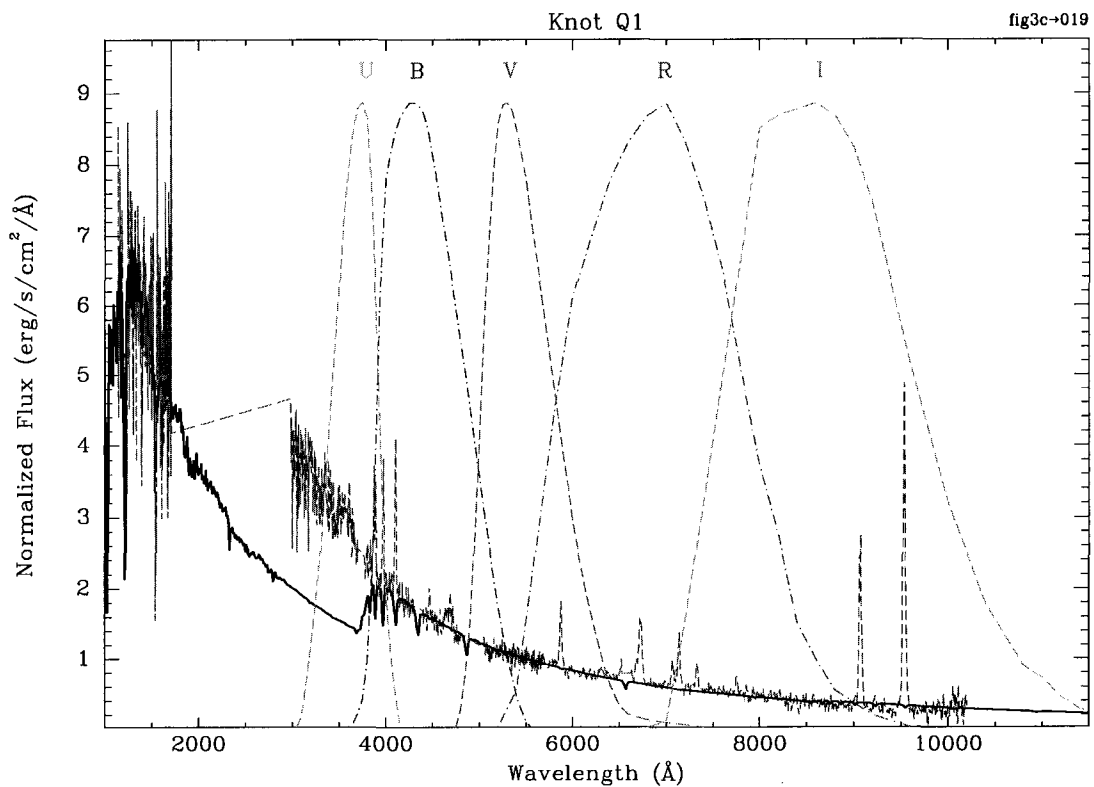
Figure 18 NGC 3396 Knot Q1 with Johnson UBVRI Filters

The best fit to the data when the Balmer decrement region is ignored is depicted by the heavy line. It is
the 19 Myr old instantaneous starburst stellar + nebular model with 0.4 solar metallicity and an α=3.30
IMF with an upper mass limit of 100 $M_\odot$. The thin line is the observed data. The Johnson UBVRI filters
are overplotted as dotted and dashed lines.

As mentioned in the section on the UV fitting technique, fitting data with large error

bars can result in poor fits, even though the χ^2 is small. To rectify this situation, we also

calculated the RMS between the model and the data and disregard any model which exceeds our RMS limit. Because of the difficulties with continuum fits just mentioned, even a "good" fit has a significantly larger RMS than the UV technique. Acknowledging this, we use a continuum RMS limit of 0.4 for the continuum fitting technique.

Initial Mass Function Analysis

One of the free parameters remaining in the models is the IMF. As was previously mentioned, we have already eliminated the low upper mass limit IMF from consideration, but there are still two remaining: one with $\alpha=2.35$ and one with $\alpha=3.30$. For our age analysis, we sought to determine the IMF which best characterized our data, and then to use that IMF for all further analysis and thus derive unique age estimates, rather than deriving two age estimates, one for each IMF. However, we were unable to select a characteristic IMF as is detailed below.

We expect to see a manifestation of the IMF, if any, at the massive end of the distribution i.e. by the relative abundance of massive stars. Since the most massive stars will, in general, be the UV-brightest we fit the UV-brightest knots (Q1 and C1) with both remaining IMF models.

In order to assess whether a particular IMF fits the data better than the others, we want examine the ratio of the most massive stars to the rest of the population. A proxy for this is to fit the spectra with the SB99 continuum models. We therefore fit the data to all the continuum models (SB99 models 1-4, and 7-10 with appropriate metallicity) in order to find the best IMF. Because the UV feature fits are normalized and because they

cover a much smaller wavelength range, we do not examine the UV feature fits in determining the best IMF.

We sought to characterize the IMF via the quality of the fits, but none of the fits were good enough to perform a meaningful hypothesis test using χ^2 statistics. Furthermore, since the data were fit equally well by several models with only small differences in the χ^2 we could not just select the IMF of the model with the minimum χ^2 as the characteristic IMF. Instead we defined the "top" models as all the models that yielded a χ^2 within a given percentage (typically 5-10%, depending on application) of the model with the minimum χ^2 and assumed that all the "top" models characterized the data equally well. For the remainder of this paper, when we discuss the "top" models, we mean "top" in this sense.

We evaluated how many of the "top" models were from a given IMF and defined the most common IMF as the characteristic IMF. We fit the data to 2 IMF's x 2 model type (stellar, or stellar + nebular) x 2 starburst type (instantaneous, or continuous) x 36 ages = 288 models. Table XX contains the results. Column (1) is the name of the knot with its galaxy number in parentheses; column (2) is the total number of models whose fit χ^2 is within 5% of the model with the minimum fit χ^2 out of 288 models; column (3) is the number of these models with an IMF of α=2.35 and M_{upper}= 100 $M_\odot$; column (4) is the number of these models with an IMF of α=3.30 and M_{upper}= 100 $M_\odot$. Columns (5, 6, 7) are the same as (2, 3, 4) except now we examine models whose fit χ^2 is within 10% of the model with the minimum fit χ^2. Columns (8, 9, 10) are the same as (2, 3, 4) except now we examine models whose fit χ^2 is within 15% of the model with the minimum fit χ^2.

Table XX. Initial Mass Function Analysis

Knot	5 %			10 %			15 %		
	#	2.35	3.30	#	2.35	3.30	#	2.35	3.30
Q1 (3396)	8	4	4	10	4	6	10	4	6
C1 (3395)	2	0	2	2	0	2	2	0	2

Examining the table, knot C1 is always consistent with the α=3.30 IMF. Knot Q1

is consistent with either a standard Saltpeter IMF (α=2.35) or the α=3.30 IMF at 5%, but

as one expands the search to 10 and 15%, the data are slightly better characterized by the

α=3.30 IMF. Table XXI presents the detailed fit statistics for the top fits in both knots.

Here for knot C1, column (1) is the rank of the fit from best to worst; column (2) is the fit

χ^2 for the model; column (3) is the percent difference between the fit χ^2 and the best

model's fit χ^2; column (4) is the RMS for the fit; column (5) is the IMF power law

coefficient for the model. Columns (6-8) are the same as (2-5) for knot Q1. Examining

the table, we see that for C1 there is a clean break in the data between the top two models

which have almost identical χ^2 and the next closest model whose χ^2 is 27% greater. The

data for Q1 are not as clear cut: there is small (~3%) breaks between the 4th and 5th

models and between the 8th and 9th models, but they are not nearly as pronounced as the

~25% break we see in C1.

Examining the table, the top two fits in knot C1 have χ^2 value of ~5500 while the

rest of the C1 fits and all of the Q1 fits are on the order of 7000-8000. One must be

cautious not to make a screening criterion based on the magnitude of the χ^2, even though

the data are suggestive. On fainter knots with larger relative error bars we will get

different values. Rather, the correct criterion to levy is to note that a large number of

"top" models (10 in this case of knot Q1) implies that none of the models fits are

particularly better than any others, whereas a small number (2 in the case of knot C1) implies a few models are clearly superior. This is a general observation: large numbers of "top" models imply an insensitivity of the data to the model parameters and therefore conclusions based on those models are weak. Conversely, when there are only a few "top" models it implies that the data are sensitive to the model parameters and there are a few clearly superior models. Conclusions based on those models are correspondingly stronger.

Table XXI Detailed IMF Fit Statistics For Top 10 Fits Knots C1 And Q1

Fit Rank	NGC 3395 Knot C1				NGC 3396 Knot Q1			
	χ^2	% from top χ^2	RMS	α[a]	χ^2	% from top χ^2	RMS	α[a]
1	5568	0.0	0.36	3.30	7017	0.0	0.33	3.30
2	5645	1.4	0.36	3.30	7021	0.1	0.33	3.30
3	7096	27.5	0.37	2.35	7028	0.1	0.33	2.35
4	7099	27.5	0.37	2.35	7028	0.2	0.33	2.35
5	7300	31.1	0.40	3.30	7258	3.4	0.33	2.35
6	7304	31.2	0.40	3.30	7260	3.5	0.33	2.35
7	7845	40.9	0.41	2.35	7282	3.8	0.35	3.30
8	7851	41.0	0.41	2.35	7285	3.8	0.35	3.30
9	8024	44.1	0.40	2.35	7443	6.1	0.36	3.30
10	8028	44.2	0.40	2.35	7444	6.1	0.36	3.30

[a] IMF power law exponent

Based on these results, we find that the data are best characterized by models with an α=3.30 IMF; however we temper this conclusion by the fact that its source, the continuum fitting technique, has serious deficiencies which were discussed previously in the continuum fitting technique description section. Even though we excluded the Balmer decrement region, which has the most severe deficiencies, the best fit to C1 still

has a reduced χ^2 of 4.3, i.e. the "typical" data point in C1 is 4.3 error bars away from the corresponding best fit model value. This undermines our confidence in this IMF estimate. In the age analysis section, we will show that the age estimates for the two IMF's are of comparable quality and therefore neither IMF is more consistent than the other with the age estimates.

Also mitigating against the $\alpha=3.30$ IMF are other SB99 models. SB99 predicts the equivalent width of He II $\lambda4686$ should be very sensitive to the assumed IMF—in fact, the equivalent width of He II $\lambda4686$ when $\alpha=2.35$ IMF should be 2-4 times that when the $\alpha=3.30$ IMF over most of the time when it is observable. SB99 also predicts that the equivalent width of He II $\lambda4686$ with the $\alpha=3.30$ IMF can only attain a maximum of 4.8 Å. Knots C4 in 3395 and Q1 in NGC 3396 have equivalent widths of He II $\lambda4686$ more than one sigma greater than 4.8Å, which suggests the $\alpha=2.35$ IMF is more appropriate. We will discuss this further in the combined age analysis section where we will combine the equivalent width with the starburst type to eliminate the $\alpha=3.30$ IMF from consideration. However, for the time being, we will not eliminate either IMF, but will continue to calculate ages for both IMF's separately.

Starburst Type Analysis

One remaining free parameter in the models is the type of starburst--instantaneous or continuous. We employed both the continuum and UV feature fit methods to assess the starburst type. In the interest of brevity and clarity, we will use the abbreviations CM for the continuum fitting method and UM for the UV feature fitting method. For each knot we examined the "top" 10% of the fits, where we define the "top" fits as in the IMF section, and defined the characteristic type as the type with a preponderance of the "top" models. The results are presented in Tables XXII and XXIII. Column (1) is the knot's name; columns (2,3) are calculated from the CM: column (2) is the knot's characteristic starburst type assuming the Saltpeter IMF (α=2.35): Cont=continuous starburst, Inst=instantaneous starburst, Neither=neither type , ---=no models gave acceptable solutions (recall for acceptable solutions the UM RMS < 0.2 or the CM RMS < 0.4); column (3) is the number of "top" instantaneous starburst models : the number of "top" continuous starburst models : the total number of Saltpeter IMF (α=2.35) CM models considered = 2 starburst types (inst. or cont.) X 2 model types (stellar or stellar+nebular) X 36 ages = 144 models; columns (4, 5) are the same as (2, 3) but using the UM where now we consider 2 starburst types X 20 ages = 40 models. Columns (6 – 9) are the same as columns (2-5) except assuming the IMF with α=3.30.

We expect not to be able to differentiate young (age < ~ 10Myr) instantaneous and continuous starbursts since there has not been enough time for the massive stars to die. For the more evolved starbursts, we expected the broader wavelength range provided by the CM to be more sensitive to whether the starburst is continuous or instantaneous because in the continuous starburst case we will have cooler stars as well as hot young stars, whereas the instantaneous case should have just older, cooler stars left. For the

sake of completeness, we calculated the results for both the UM and CM, although in general, we did not expect the UM to be a good discriminator.

Examining the CM results, the majority of the knots in both galaxies are not fit by either type--no models gave acceptable solutions (recall for acceptable solutions the UM RMS < 0.2 or the CM RMS < 0.4). This is typically the case in faint knots such as A, B, M, N, O, and P. The CM characterized the UV-brightest knots (C1 and Q1) in all cases as an instantaneous starburst. Furthermore, when the CM fits were acceptable, the overwhelming majority of the measurement knots were better characterized by an instantaneous starburst rather than a continuous starburst.

Table XXII. NGC 3395 Starburst Type Estimates

Knot	$\alpha=2.35$				$\alpha=3.30$			
	Cont Type	Cont Type #	UV Type	UV Type #	Cont Type	Cont Type #	UV Type	UV Type #
D	---	0:0:144	---	0:0:40	---	0:0:144	---	0:0:40
C80	---	0:0:144	---	0:0:40	---	0:0:144	---	0:0:40
C70	---	0:0:144	---	0:0:40	---	0:0:144	---	0:0:40
C60	---	0:0:144	---	0:0:40	---	0:0:144	---	0:0:40
C1	Inst	2:0:144	Inst	1:0:40	Inst	2:0:144	Inst	1:0:40
C2	---	0:0:144	Cont	0:13:40	---	0:0:144	Inst	2:0:40
C3	---	0:0:144	Cont	1:12:40	---	0:0:144	Inst	2:0:40
C4	---	0:0:144	---	0:0:40	---	0:0:144	---	0:0:40
C50	---	0:0:144	---	0:0:40	---	0:0:144	---	0:0:40
B	---	0:0:144	---	0:0:40	---	0:0:144	---	0:0:40
A	---	0:0:144	---	0:0:40	---	0:0:144	---	0:0:40
NGC 3395	Cont	0:4:144	Inst	2:0:40	Cont[a]	4:6:144	Cont	3:8:40

[a] Best model definition is weak because a large number of models fit for both starburst types

Table XXIII. NGC 3396 Starburst Type Estimates

Knot	α=2.35				α=3.30			
	Cont Type	Cont Type #	UV Type	UV Type #	Cont Type	Cont Type #	UV Type	UV Type #
S3[a]	---	0:0:144	---	0: 0:40	---	0:0:144	---	0:0:40
S1[a]	Inst	2:0:144	Cont	2:10:40	Inst	2:0:144	Cont	5:20:40
S2[a]	Inst	2:0:144	---	0:0:40	Inst	2:0:144	---	0:0:40
S10[a]	Inst	2:0:144	---	0:0:40	Inst	2:0:144	---	0:0:40
R[a]	Inst	4:0:144	---	0:0:40	Inst	2:0:144	---	0:0:40
R10	Cont[b]	4:5:144	---	0:0:40	Inst	6:3:144	---	0:0:40
R20	Inst	2:0:144	---	0:0:40	Neither	2:2:144	---	0:0:40
Q3	Neither	4:4:144	---	0:0:40	Neither	2:2:144	---	0:0:40
Q2	Inst	2:0:144	---	0:0:40	Neither	4:4:144	Inst	1:0:40
Q1	Inst	4:0:144	Cont	1:13:40	Inst	6:0:144	Inst	1:0:40
Q30	------	0:0:144	---	0:0:40	---	0:0:144	---	0:0:40
Q20	Inst	4:0:144	---	0:0:40	Neither[b]	6:6:144	---	0:0:40
Q10	---	0:0:144	---	0:0:40	---	0:0:144	---	0:0:40
P2[a]	---	0:0:144	---	0:0:40	---	0:0:144	---	0:0:40
P	---	0:0:144	---	0:0:40	---	0:0:144	---	0:0:40
O	---	0:0:144	---	0:0:40	---	0:0:144	---	0:0:40
N	---	0:0:144	---	0:0:40	---	0:0:144	---	0:0:40
M[e]	---	0:0:144	---	0:0:40	---	0:0:144	---	0:0:40
NGC 3396	Inst	2:0:144	Inst	3:0:40	Cont	0:2:144	Cont	1:12:40

[a] Models not reddened due to inability to measure $H\alpha$ or $H\beta$ in measurement knot.

[b] Best model definition is weak because a large number of models fit for both starburst types

Next we turn our attention to knots which the CM predicts should be best modeled by continuum starbursts. A continuous starburst needs a steady source of gas to form new stars in order to maintain itself. Standard models, including SB99 use a star formation rate of $1 M_\odot$/year. We perform an order of magnitude estimate in order to assess whether or not it is reasonable to have a measurement knot undergoing a continuous starburst.

We will model the starburst progenitor region as a giant molecular cloud. The typical giant molecular cloud is about 50 pc in size with an average density of 100 hydrogen atoms per cm^3 (Goldsmith 1987) which corresponds to a total mass of roughly $1.28 \times 10^6 M_\odot$. Our largest measurement knots are only ~ 15 CCD pixels long = 0.75". Projecting out to 28.3 Mpc (Hanckock, 2002) our knots have a radius of approximately 50 pc as well. Given this size and density, our largest measurement knots could sustain a continuous starburst for only about 1.3 million years, which is effectively instantaneous since our model age resolution is only 1 Myr. Therefore we conclude that it is unlikely that our measurement knots are continuous starbursts and we disregard these solutions. Our starburst type analysis is in excellent agreement with this order of magnitude calculation with the majority of the measurement knots that showed a preferred model type being better modeled by an instantaneous starburst.

The assumption that the measurement knots are better modeled by instantaneous starbursts is further reinforced by the equivalent width of He II $\lambda 4686$. SB99 predicts the equivalent width of He II $\lambda 4686$ should be very sensitive to the assumed starburst type—in fact, the equivalent width of He II $\lambda 4686$ for an instantaneous starburst should be 3-4 times that for a continuous starburst over most of the time when it is observable.

SB99 also predicts that the equivalent width of He II $\lambda 4686$ for a continuous starburst can only attain a maximum of ~ 3 Å. Knots C4 in 3395 and Q1, Q2, Q30, and R20 in NGC 3396 have equivalent widths of He II $\lambda 4686$ more than one sigma greater than 3Å, which suggests these particular knots are instantaneous starbursts

The unresolved knots are ~ 1.7 kpc in size; however, and are therefore large enough to support a continuous starburst. It is interesting to note that while the measurement knots show a strong tendency towards instantaneous starburst models, the NGC 3395 unresolved knot for both IMFs and the NGC 3396 unresolved knot for $\alpha=3.30$ are best modeled by continuous star formation. This is somewhat counter-intuitive since the brightest knots (which are best fit by instantaneous models) dominate the spectra of the unresolved knot as well. However the unresolved knots contain significant older, non-starburst populations that are not included in the measurement knots. These stars contribute to the older star flux and as a result we may have several distinct populations: a young starburst population intermingled with an older more evolved starburst population intermingled with a population that is older still (perhaps even predating the occurrence of significant interactions between the galaxies). The SB99 models that most closely model these multiple populations are the continuous starburst models. From this we conclude that while unresolved knot spectra may appear to favor continuous starburst models, and continuous starbursts may be theoretically possible for a region this large, they probably contain knots of more or less instantaneous star formation embedded in older populations.

It is also interesting to observe that the CM starburst type prediction appears to be largely insensitive to the IMF assumed. From the tables, both IMF's yield the same starburst type most of the time. Out of the 13 knots with acceptable solutions, there are

only five in which the CM starburst type determinations are in disagreement between the two IMFs. In three of the five, the type determination is inconclusive and in one of the two remaining (R10), the α=2.35 estimate is only weakly defined. Therefore there is only one knot (the NGC 3396 unresolved knot) out of 16 in which there is a clear starburst type conflict between the two IMFs. In the age analysis section we will show that the this knot is best represented by an continuous starburst as is the NGC 3395 unresolved knot. We will also show ages derived from the two IMF's are almost the same for the instantaneous case, but differ drastically for the continuous case. Therefore we conclude that the ages derived from instantaneous models are not sensitive to the assumed IMF while the continuous model ages are.

<div style="text-align:center">

UV Feature and Continuum Fitting

Age Estimates

</div>

The knots were fit to a range of ages via the CM (from 1Myr to 900Myr) and the UM (from 1Myr to 20Myr). They were fit to both instantaneous and continuous starbursts, and both α=2.35 and α=3.30 IMFs using the CM and UM techniques. As discussed in the IMF section, in general the data were equally well fit by several models with only small variations in the reduced χ^2. Therefore we again defined the "top" models as those models whose χ^2 is within 10% of the model with the minimum χ^2. For the sake of brevity, I will define the age calculated from the "top" UM fits as the UM age. Likewise, I will define the CM age as the age calculated from the "top" CM fits. The results of the age determination are presented in Tables XXIV-XXXI. In these tables column (1) is the name of the knot; column (2) is the UM age and error defined as the

mean and standard deviation of the "top" UM models; column (3) is the CM age and error defined as the mean and standard deviation of the "top" CM models. When we were unable to deredden a knot due to a lack of $H\alpha$ or $H\beta$, we still calcualted a CM age. This age is an upper limit and we denote this by ":" in the table. The other columns will be introduced later as they are discussed.

First we will examine the continuous starburst results. As was discussed in the starburst type analysis section, our measurement knots are too small to sustain a continuous starburst for any significant length of time, therefore we will not consider them as candidates for the continuous starburst models and will only consider the unresolved knots as continuous starburst candidates.

At steady state, we have a constant production of hot young stars, regardless of the how long the starburst has been going on. The biggest age discriminator is the lower mass tail which should increase with time as high mass stars die off, while low mass stars live on. Therefore a priori, one would expect the age estimates from continuous starburst models to be somewhat indiscriminate, in particular we expect UM predictions to be extremely indiscriminate, which in fact they are. For instance, the NGC 3395 unresolved knot was predicted to be best fit by a continuous starburst for both IMFs (α=2.35 and 3.30). The α=2.35 UM age for this knot is based on 8 models and is the average of all UM models with age $\geq$ 12 Myr. Similarly, the α=3.30 UM age is based on 10 models and is the average of all the models between 7 and 16 Myr. Thus the UM for continuous starbursts effectively amounts to a test of whether O stars are present or not.

Table XXIV. NGC 3395 Age Estimates (Continuous Starburst, IMF=2.35)

Knot	UV Age (Myr)	Cont Age (Myr)	β_{1550} (Myr)	Hα (Myr)	Hβ (Myr)	He IIλ4686 (Myr)	U-B (Myr)	B-V (Myr)	V-R (Myr)	V-I (Myr)
D[a]	n/a	n/a	n/a	Old[b]	n/a	n/a	n/a	n/a	n/a	n/a
C80	n/a	n/a	Young[b]	Old	Old	n/a	7.5	8.4	Old	Old
C70	n/a	n/a	Old	950.5 ±950.5	386.6 ±49.5	n/a	7.5	9.0	Old	14.2; 17.4; 53.6
C60	n/a	n/a	Old	Old	Old	Young	9.0	2.4; 6.7	1.5; 10.1	10.8
C1	14.0 ±3.9	82.2 ±13.9	2.8 ±18.0	Old	Old	Young	6.7	Young	Young	Young
C2	14.0 ±3.9	n/a	623.3 ±623.3	Old	Old	Young	6.5	Young	Young	Young
C3	14.0 ±3.9	n/a	95.8 ±159.7	Old	Old	Young	6.0	Young	2.7; 8.9	Young
C4	n/a	n/a	358.3 ±358.4	Old	280.8 ±28.6	Young	8.3	7.8	Old	12.0
C50	n/a	n/a	50.1 ±89.7	Old	Old	n/a	9.3	10.2	Old	Old
B	n/a	n/a	186.1 ±380.2	Old	Old	n/a	16.7	60.8	Old	Old
A	n/a	n/a	Old	Old	Old	n/a	10.1	0.6; 7.2	Old	Old
NGC 3395	16.5 ±2.4	250.0 ±57.7	Young	Old	Old	n/a	10.3	8.0	783.6	13.8; 19.2; 41.0

[a] Knot not dereddened because Hα or Hβ unavailable

[b] "Old" = Age estimate off calibration chart to the old extreme, "Young" = Age estimate off calibration chart to the young extreme

Table XXV. NGC 3395 Age Estimates (Instantaneous Starburst, IMF=2.35)

Knot	UV Age (Myr)	Cont Age (Myr)	β_{1550} (Myr)	Hα (Myr)	Hβ (Myr)	He IIλ4686 (Myr)	U-B (Myr)	B-V (Myr)	V-R (Myr)	V-I (Myr)
D[a]	n/a	n/a	n/a	6.2 ±0.2	n/a	n/a	n/a	n/a	n/a	n/a
C80	n/a	n/a	Young[b]	6.3 ±0.7	5.8 ±0.1	n/a	4.1	6.0; 16.5; 21.9	7.9; 14.8	7.7; 15.0; 756.7-936.9
C70	n/a	n/a	77.2 ±12.7	5.9 ±0.4	5.1 ±0.0	n/a	4.1	6.1; 16.3; 22.2; 25.4	7.3; 15.1; 618.0-720.2	7.1; 15.5; 23.8
C60	n/a	n/a	17.0 ±6.2	6.5 ±0.7	5.9 ±0.1	4.5 ±4.6	4.7	1.5; 4.9; 5.1; 18.8	0.9; 6.8; 15.7; 22.6	6.9; 15.9; 22.1
C1	5.0 ±n/a	19.0 ±n/a	1.5 ±1.7	10.2 ±1.4	9.8 ±0.1	4.0 ±0.5	4.0	Young	Young	Young
C2	4.5 ±0.7	n/a	17.8 ±9.3	6.9 ±0.9	6.3 ±0.0	3.1 ±n/a	3.9	3.1	2.7; 5.2	Young
C3	5.0 ±n/a	n/a	5.0 ±11.8	6.3 ±0.7	5.8 ±0.0	4.0 ±0.5	3.3	2.5-4.5	1.8; 6.7; 15.9; 22.0	2.7-4.6
C4	n/a	n/a	17.0 ±6.3	6.0 ±0.4	5.0 ±0.0	Young	4.6	5.7; 16.7; 21.6	7.2; 15.2; 90.5-594.6	7.0; 15.7; 22.7
C50	n/a	n/a	3.9 ±12.5	6.3 ±0.7	5.7 ±0.1	n/a	4.7	6.2; 16.2; 22.6-25.9	7.6; 15.0; 749.4-837.2	7.3; 15.3; 39.5; 49.9-61.4; 70.6-587.6
B	n/a	n/a	16.8 ±10.5	10.1 ±1.2	8.4 ±0.7	n/a	4.8	7.5; 8.5; 23.5	Old[b]	Old

Table XXV NGC 3395 Age Estimates (Instantaneous Starburst, IMF=2.35) (Continued)

Knot	UV Age (Myr)	Cont Age (Myr)	β_{1550} (Myr)	Hα (Myr)	Hβ (Myr)	He IIλ4686 (Myr)	U-B (Myr)	B-V (Myr)	V-R (Myr)	V-I (Myr)
A	n/a	n/a	24.7 ±7.4	6.7 ±0.8	6.2 ±0.1	n/a	4.7	0.4; 5.2; 17.3; 20.8	7.4; 15.1; 657.0-747.8	7.5; 15.1; 605.1-775.8
NGC 3395	5.5 ±0.7	15.3 ±10.1	Young	7.3 ±1.2	6.8 ±0.3	n/a	4.7	5.8; 16.6; 21.7	7.1; 15.3; 46.2; 72.1; 346.5-472.4	7.1; 15.5; 23.6

[a] Knot not dereddened because Hα or Hβ unavailable

[b] "Old" = Age estimate off calibration chart to the old extreme, "Young" = Age estimate off calibration chart to the young extreme

128

Table XXVI. NGC 3395 Age Estimates (Continuous Starburst, IMF=3.30)

Knot	UV Age (Myr)	Cont Age (Myr)	β_{1550} (Myr)	Hα (Myr)	Hβ (Myr)	He IIλ4686 (Myr)	U-B (Myr)	B-V (Myr)	V-R (Myr)	V-I (Myr)
D[a]	n/a	n/a	n/a	66.8 ±65.4	n/a	n/a	n/a	n/a	n/a	n/a
C80	n/a	n/a	Young[b]	67.0 ±62.0	38.9 ±4.5	n/a	5.2	9.7	Old[b]	Old
C70	n/a	n/a	650.1 ±315.1	37.4 ±35.1	20.6 ±1.1	n/a	5.3	12.2	Old	911.4
C60	n/a	n/a	57.1 ±29.6	85.7 ±80.4	46.3 ±3.7	Young	5.8	7.0	13.5; 17.8; 87.3	12.5
C1	8.0 ±2.7	30.0 ±n/a	Young	745.1 ±745.1	430.7 ±29.1	Young	0.2; 3.6	Young	Young	Young
C2	6.5 ±1.9	n/a	71.5 ±36.9	125.9 ±127.8	82.3 ±2.8	Young	Young	Young	3.1; 7.3	Young
C3	7. 5 ±2.4	n/a	29.2 ±19.4	70.8 ±65.5	41.7 ±1.2	Young	Young	Young	11.6	Young
C4	n/a	n/a	57.1 ±31.6	40.9 ±38.6	18.1 ±0.7	Young	5.6	8.6	Old	14.1; 16.4; 138.1
C50	n/a	n/a	20.2 ±15.7	66.3 ±61.3	35.7 ±2.0	n/a	5.9	14.7; 17.6; 54.9	Old	Old
B	n/a	n/a	46.7 ±35.9	283.2 ±303.7	151.9 ±39.8	n/a	7.5	51.7	Old	Old

Table XXVI. NGC 3395 Age Estimates (Continuous Starburst, IMF=3.30) (Continued)

Knot	UV Age (Myr)	Cont Age (Myr)	β_{1550} (Myr)	Hα (Myr)	Hβ (Myr)	He IIλ4686 (Myr)	U-B (Myr)	B-V (Myr)	V-R (Myr)	V-I (Myr)
A	n/a	n/a	96.9 ±47.1	103.9 ±101.5	76.0 ±17.7	n/a	6.0	7.7	Old	Old
NGC 3395	11.5 ±3.0	70.0 ±8.9	Young	176.8 ±191.4	121.4 ±7.0	n/a	6.1	8.8	Old	834.9

[a] Knot not dereddened because Hα or Hβ unavailable

[b] "Old" = Age estimate off calibration chart to the old extreme, "Young" = Age estimate off calibration chart to the young extreme

Table XXVII. NGC 3395 Age Estimates (Instantaneous Starburst, IMF=3.30)

Knot	UV Age (Myr)	Cont Age (Myr)	β_{1550} (Myr)	Hα (Myr)	Hβ (Myr)	He II λ4686 (Myr)	U-B (Myr)	B-V (Myr)	V-R (Myr)	V-I (Myr)
D[a]	n/a	n/a	n/a	6.1 ±0.3	n/a	n/a	n/a	n/a	n/a	n/a
C80	n/a	n/a	Young[b]	6.3 ±0.7	5.7 ±0.1	n/a	3.4	6.4; 16.2; 22.3; 25.4	12.7	8.8; 14.2
C70	n/a	n/a	68.2 ±10.1	5.9 ±0.5	5.0 ±0.0	n/a	3.4	6.5; 16.1; 23.0; 28.3	8.6-10.4; 14.3; 755.7-838.0	7.7; 15.0; 146.4-164.2; 246.3-551.0
C60	n/a	n/a	16.6 ±2.0	6.5 ±0.8	5.9 ±0.1	Young	3.9	5.2	7.1; 15.4; 39.2	7.1; 15.4; 26.8
C1	4.0 ±n/a	6.0 ±n/a	Young	9.9 ±1.3	8.8 ±0.0	Young	0.1; 3.1	Young	Young	Young
C2	3.5 ±0.7	n/a	17.0 ±6.0	7.0 ±0.9	6.3 ±0.0	4.6 ±0.1	1.0-2.5	Young	2.0; 6.1	Young
C3	3.5 ±0.7	n/a	14.4 ±1.9	6.3 ±0.7	5.7 ±0.0	Young	Young	Young	7.0; 15.6; 24.9	2.6; 4.8
C4	n/a	n/a	16.6 ±3.1	6.0 ±0.5	4.9 ±0.0	Young	3.5	6.1; 16.5; 21.7	8.2; 14.6; 617.7-686.9	7.3; 15.2; 42.2; 50.2-59.6
C50	n/a	n/a	4.9 ±10.7	6.3 ±0.7	5.6 ±0.1	n/a	3.9	6.6; 15.9; 33.1	9.1-11.0; 14.0; 929.6	8.1; 14.7; 584.1-699.1
B	n/a	n/a	14.9 ±4.2	9.8 ±1.2	8.2 ±0.8	n/a	4.7	24.2	Old[b]	Old

131

Table XXVII NGC 3395 Age Estimates (Instantaneous Starburst, IMF=3.30) (Continued)

Knot	UV Age (Myr)	Cont Age (Myr)	β_{1550} (Myr)	Hα (Myr)	Hβ (Myr)	He IIλ4686 (Myr)	U-B (Myr)	B-V (Myr)	V-R (Myr)	V-I (Myr)
A	n/a	n/a	20.8 ±6.3	6.8 ±0.8	6.2 ±0.2	n/a	4.0	5.8; 17.3; 20.6	8.7-10.7; 14.2; 855.6	8.5; 14.4; 821.1-931.8
NGC 3395	5.0 ±1.0	11.0 ±4.6	Young	7.5 ±1.1	6.8 ±0.1	n/a	4.0	6.2; 16.4; 21.9	7.8; 14.8; 505.5-595.3	7.7; 15.0; 143.6; 148.8-178.1; 225.3-531.6

a Knot not dereddened because Hα or Hβ unavailable

b "Old" = Age estimate off calibration chart to the old extreme, "Young" = Age estimate off calibration chart to the young extreme

132

Table XXVIII. NGC 3396 Age Estimates (Continuous Starburst, IMF=2.35)

Knot	UV Age (Myr)	Cont Age (Myr)	β_{1550} (Myr)	Hα (Myr)	Hβ (Myr)	He IIλ4686 (Myr)	U-B (Myr)	B-V (Myr)	V-R (Myr)	V-I (Myr)
S3[a]	n/a	n/a	n/a	Old[b]	n/a	n/a	n/a	n/a	n/a	n/a
S1[a]	15.5 ±3.0	n/a	n/a	Old	n/a	n/a	n/a	n/a	n/a	n/a
S2[a]	n/a	n/a	n/a	Old	n/a	n/a	n/a	n/a	n/a	n/a
S10[a]	n/a	n/a	n/a	Old	n/a	n/a	n/a	n/a	n/a	n/a
R[a]	n/a	n/a	n/a	Old	n/a	n/a	n/a	n/a	n/a	n/a
R10	n/a	820.0 ±83.7	5.4 ±23.0	Old	Old	n/a	248.2	2.6; 12.5	2.9; 61.5	31.2
R20	n/a	n/a	6.3 ±47.1	Old	Old	n/a	Old	794.8	Old	Old
Q3	n/a	850.0 ±57.7	3.6 ±26.3	Old	Old	n/a	35.4	8.7	Old	14.2; 17.3; 53.7
Q2	n/a	400.0 ±89.4	Young[b]	Old	903.2 ±49.0	Young	7.5	Young	11.2	8.3
Q1	11.0 ±3.9	92.0 ±8.4	Old	404.7 ±404.7	232.1 ±5.3	Young	5.7	Young	2.1; 9.5	4.9

Table XXVIII. NGC 3396 Age Estimates (Continuous Starburst, IMF=2.35) (Continued)

Knot	UV Age (Myr)	Cont Age (Myr)	β_{1550} (Myr)	Hα (Myr)	Hβ (Myr)	He IIλ4686 (Myr)	U-B (Myr)	B-V (Myr)	V-R (Myr)	V-I (Myr)
Q30	n/a	n/a	Young	613.4 ±613.4	437.2 ±41.6	Young	6.7	3.7; 5.3	Old	9.6
Q20	n/a	250.0 ±57.7	Young	Old	Old	n/a	39.3	Young	3.5; 7.8	8.0
Q10	n/a	n/a	Young	Old	Old	n/a	197.3	8.2	3.1; 7.3	9.5
P2[a]	n/a	n/a	n/a	Old	n/a	n/a	n/a	n/a	n/a	n/a
P	n/a	n/a	Young	Old	Old	n/a	41.7	8.2	Old	Old
O	n/a	n/a	Old	Old	Old	n/a	32.1	8.5	Old	Old
N	n/a	n/a	Old	Old	Old	n/a	525.3	Old	Old	Old
M[a]	n/a	n/a	n/a	n/a	n/a	n/a	n/a	n/a	n/a	n/a
NGC 3396	16.5 ±2.4	900.0 ±n/a	139.8 ±238.5	Old	Old	4.6 ±0.6	90.4	9.0	14.3; 16.8; 106.0	12.1

[a] Knot not dereddened because Hα or Hβ unavailable

[b] "Old" = Age estimate off calibration chart to the old extreme, "Young" = Age estimate off calibration chart to the young extreme

134

Table XXIX. NGC 3396 Age Estimates (Instantaneous Starburst, IMF=2.35)

Knot	UV Age (Myr)	Cont Age (Myr)	β_{1550} (Myr)	Hα (Myr)	Hβ (Myr)	He IIλ4686 (Myr)	U-B (Myr)	B-V (Myr)	V-R (Myr)	V-I (Myr)
S3[a]	n/a	n/a	n/a	11.3 ±2.3	n/a	n/a	n/a	n/a	n/a	n/a
S1[a]	5.5 ±0.7	500.0:	n/a	22.6 ±3.6	n/a	n/a	n/a	n/a	n/a	n/a
S2[a]	n/a	300.0:	n/a	13.1 ±2.0	n/a	n/a	n/a	n/a	n/a	n/a
S10[a]	n/a	400.0:	n/a	13.5 ±1.1	n/a	n/a	n/a	n/a	n/a	n/a
R[a]	n/a	300.0:	n/a	12.2 ±0.5	n/a	n/a	n/a	n/a	n/a	n/a
R10	n/a	45.0 ±5.8	2.9 ±0.1	11.1 ±1.2	10.1 ±0.2	n/a	6.6; 8.0; 12.5; 17.7; 21.0	1.8; 6.8; 19.1	2.0; 14.0; 14.2; 24.4	7.6; 8.9-10.8; 15.7; 19.4
R20	n/a	200.0 ±n/a	3.2 ±0.7	7.5 ±1.1	6.3 ±0.0	n/a	6.7 16.0; 62.7	6.9; 15.5; 84.3	8.5; 14.4	7.9; 14.8
Q3	n/a	45.0 ±5.8	3.0 ±0.4	6.3 ±0.7	5.7 ±0.0	n/a	5.0	6.0; 16.4; 22.1	7.3; 15.1; 601.2-672.8	7.1; 15.5; 23.8
Q2	n/a	16.0 ±n/a	Young[b]	6.0 ±0.4	5.5 ±0.0	4.5 ±n/a	4.1	2.4; 4.1	6.9; 15.6; 23.0	6.4
Q1	4.0 ±n/a	19.0 ±1.2	45.1 ±11.7	5.5 ±0.6	5.0 ±0.0	4.5 ±n/a	3.2	Young	1.4; 6.8; 15.8; 22.4	2.4; 5.0
Q30	n/a	n/a	Young	5.7 ±0.5	5.1 ±0.0	4.6 ±4.6	4.0	2.2; 4.8	7.2; 15.2; 90.5 -117.2; 175.9; 244.5-588.6	6.7; 16.5; 20.9

Table XXIX. NGC 3396 Age Estimates (Instantaneous Starburst, IMF=2.35) (Continued)

Knot	UV Age (Myr)	Cont Age (Myr)	β_{1550} (Myr)	Hα (Myr)	Hβ (Myr)	He ɪɪλ4686 (Myr)	U-B (Myr)	B-V (Myr)	V-R (Myr)	V-I (Myr)
Q20	n/a	11.5 ±6.4	Young	7.0 ±1.1	6.8 ±0.2	n/a	5.1	2.3; 4.7	2.2; 6.6; 16.5; 21.2	6.2
Q10	n/a	n/a	Young	6.6 ±0.8	6.3 ±0.1	n/a	6.3; 8.1; 13.5	6.3; 9.5; 12.3; 16.0; 20.5	1.8; 6.5	6.6
P2[a]	n/a	n/a	n/a	10.5 ±1.5	n/a	n/a	n/a	n/a	n/a	n/a
P	n/a	n/a	Young	6.7 ±0.8	6.2 ±0.1	n/a	5.1; 13.1	5.9; 16.5; 21.8	7.2; 15.2; 123.9-143.2; 167.1; 170.5; 254.0-616.9	7.8; 14.9; 837.7-981.4
O	n/a	n/a	146.7 ±15.3	6.8 ±0.8	6.2 ±0.1	n/a	5.0	6.0; 16.4; 22.0	7.4; 15.1; 657.0-747.8	7.9; 14.8
N	n/a	n/a	490.3 ±126.2	13.0 ±1.7	9.9 ±0.4	n/a	36.7	500.5-584.8	Old[b]	Old
M[a]	n/a	n/a	n/a	n/a	n/a	n/a	n/a	n/a	n/a	n/a
NGC 3396	6.0 ±1.0	50.0 ±n/a	16.4 ±0.6	7.3 ±1.2	6.5 ±0.0	3.1 ±n/a	5.2; 10.8; 13.9; 19.0	6.1; 16.3; 22.2; 25.4	7.0; 15.4; 36.8	7.0; 15.7; 22.7

[a] Knot not dereddened because Hα or Hβ unavailable. ":" denotoes CM age shown is upper limits on the age since not dereddened.

[b] "Old" = Age estimate off calibration chart to the old extreme, "Young" = Age estimate off calibration chart to the young extreme

136

Table XXX. NGC 3396 Age Estimates (Continuous Starburst, IMF=3.30)

Knot	UV Age (Myr)	Cont Age (Myr)	β_{1550} (Myr)	Hα (Myr)	Hβ (Myr)	He IIλ4686 (Myr)	U-B (Myr)	B-V (Myr)	V-R (Myr)	V-I (Myr)
S3[a]	n/a	n/a	n/a	Old[b]	n/a	n/a	n/a	n/a	n/a	n/a
S1[a]	10.5 ±5.9	n/a	n/a	Old	n/a	n/a	n/a	n/a	n/a	n/a
S2[a]	n/a	n/a	n/a	Old	n/a	n/a	n/a	n/a	n/a	n/a
S10[a]	n/a	n/a	n/a	Old	n/a	n/a	n/a	n/a	n/a	n/a
R[a]	n/a	n/a	n/a	Old	n/a	n/a	n/a	n/a	n/a	n/a
R10	n/a	266.7 ±57.7	5.0 ±10.3	525.0 ±525.0	399.8 ±48.5	n/a	47.4	21.5	73.6	35.6
R20	n/a	850.0 ±57.7	4.6 ±16.1	202.7 ±223.7	79.5 ±5.4	n/a	256.3	583.7	Old	Old
Q3	n/a	200.0 ±n/a	Young[b]	64.3 ±59.5	36.9 ±1.0	n/a	8.6	11.3	Old	911.4
Q2	n/a	95.0 ±5.8	Young	43.4 ±41.0	28.8 ±0.6	Young	5.3	Young	150.1	9.3
Q1	5.5 ±1.3	45.0 ±5.8	245.8 ±108.5	25.4 ±24.2	16.9 ±0.1	Young	Young	Young	12.7; 20.2; 56.0	7.1
Q30	n/a	n/a	Young	30.6 ±29.0	21.6 ±0.8	Young	0.7; 3.5	3.5; 5.5	Old	11.1

Table XXX. NGC 3396 Age Estimates (Continuous Starburst, IMF=3.30) (Continued)

Knot	UV Age (Myr)	Cont Age (Myr)	β_{1550} (Myr)	Hα (Myr)	Hβ (Myr)	He IIλ4686 (Myr)	U-B (Myr)	B-V (Myr)	V-R (Myr)	V-I (Myr)
Q20	n/a	75.0 ±12.0	Young	142.1 ±148.9	121.7 ±6.2	n/a	9.2	Young	9.4	8.9
Q10	n/a	n/a	Young	236.8 ±267.2	132.8 ±25.8	n/a	36.8	13.9	8.4	11.0
P2[a]	n/a	n/a	n/a	824.0 ±824.1	n/a	n/a	n/a	n/a	n/a	n/a
P	n/a	n/a	Young	104.1 ±101.8	65.9 ±12.5	n/a	9.7	9.3	Old	Old
O	n/a	n/a	Old	113.4 ±112.4	63.8 ±10.3	n/a	8.1	10.7	Old	Old
N	n/a	n/a	Old	456.3 ±477.7	93.5 ±12.4	n/a	109.1	Old	Old	Old
M[a]	n/a	n/a	n/a	n/a	n/a	n/a	n/a	n/a	n/a	n/a
NGC 3396	11.5 ±3.6	200.0 ±n/a	35.9 ±22.5	180.3 ±196.7	112.2 ±1.8	Young	20.9	12.2	802.4	14.3; 16.0; 147.2

[a] Knot not dereddened because Hα or Hβ unavailable

[b] "Old" = Age estimate off calibration chart to the old extreme, "Young" = Age estimate off calibration chart to the young extreme

138

Table XXXI. NGC 3396 Age Estimates (Instantaneous Starburst, IMF=3.30)

Knot	UV Age (Myr)	Cont Age (Myr)	β_{1550} (Myr)	Hα (Myr)	Hβ (Myr)	He IIλ4686 (Myr)	U-B (Myr)	B-V (Myr)	V-R (Myr)	V-I (Myr)
S3[a]	n/a	n/a	n/a	11.2 ±1.8	n/a	n/a	n/a	n/a	n/a	n/a
S1[a]	3.6 ±2.1	500.0:	n/a	21.9 ±3.4	n/a	n/a	n/a	n/a	n/a	n/a
S2[a]	n/a	300.0:	n/a	13.0 ±1.7	n/a	n/a	n/a	n/a	n/a	n/a
S10[a]	n/a	400.0:	n/a	12.9 ±1.6	n/a	n/a	n/a	n/a	n/a	n/a
R[a]	n/a	300.0:	n/a	11.1 ±1.3	n/a	n/a	n/a	n/a	n/a	n/a
R10	n/a	55.0 ±12.0	2.9 ±2.2	10.8 ±1.2	9.7 ±0.4	n/a	7.5; 12.5; 19.1	7.1; 10.4; 19.0	25.8	13.1; 14.5; 23.0
R20	n/a	200.0 ±n/a	3.2 ±1.8	7.6 ±1.1	6.3 ±0.0	n/a	58.5	7.3; 9.0; 14.5; 127.4	Old[b]	9.2; 14.0
Q3	n/a	40.0 ±n/a	Young[b]	6.3 ±0.7	5.6 ±0.0	n/a	5.0	6.4; 16.1; 22.7-25.9	9.7; 14.4; 713.0-806.0	7.7; 15.0; 146.4-164.2; 246.3-551.0
Q2	4.0 ±n/a	23.0 ±8.1	Young	6.0 ±0.5	5.4 ±n/a	Young	3.4	3.0-4.4	7.2; 15.3; 46.8; 67.2	6.7; 16.5; 21.2
Q1	3.0 ±n/a	19.0 ±0.9	37.9 ±8.6	5.5 ±0.7	4.9 ±n/a	Young	Young	Young	7.0; 15.5; 35.5	5.6
Q30	n/a	n/a	Young	5.7 ±0.6	5.1 ±n/a	Young	0.4; 2.9	2.1; 4.8	8.2; 14.6; 605.1-672.8	7.0; 15.7; 22.8

Table XXXI. NGC 3396 Age Estimates (Instantaneous Starburst, IMF=3.30) (Continued)

Knot	UV Age (Myr)	Cont Age (Myr)	β_{1550} (Myr)	Hα (Myr)	Hβ (Myr)	He II λ4686 (Myr)	U-B (Myr)	B-V (Myr)	V-R (Myr)	V-I (Myr)
Q20	n/a	13.3 ±4.9	Young	7.1 ±1.1	6.8 ±0.1	n/a	5.1	2.6; 4.7	6.8; 15.9; 22.4	6.7; 16.8; 20.2
Q10	n/a	n/a	Young	6.7 ±0.8	6.3 ±0.1	n/a	6.3; 8.0; 13.0	6.4; 9.0; 12.3; 15.8; 20.7	6.6; 15.9; 20.1	6.8; 15.2; 22.0
P2[a]	n/a	n/a	n/a	10.1 ±1.3	n/a	n/a	n/a	n/a	n/a	n/a
P	n/a	n/a	Young	6.8 ±0.8	6.2 ±0.2	n/a	5.1	6.3; 16.3; 22.1	8.3; 14.6; 628.4-713.4	8.9; 14.2
O	n/a	n/a	133.9 ±13.2	6.9 ±0.8	6.1 ±0.2	n/a	5.0	6.4; 16.2; 22.5-25.9	8.7; 9.6; 10.6; 14.2; 855.6	9.2; 14.1
N	n/a	n/a	423.7 ±66.7	12.6 ±1.3	9.2 ±0.2	n/a	32.7	704.0-798.2	Old	Old
M[a]	n/a	n/a	n/a	n/a	n/a	n/a	n/a	n/a	n/a	n/a
NGC 3396	5.0 ±1.0	50.0 ±n/a	15.6 ±1.0	7.5 ±1.1	6.6 ±0.1	4.6 ±n/a	5.4	6.5; 16.1; 23.0; 24.2; 28.4	7.4; 15.0; 133.0; 136.7; 173.9; 179.2; 211.0-472.4	7.3; 15.2; 42.6; 51.0; 58.7-66.5

[a] Knot not dereddened because Hα or Hβ unavailable. ":" denotoes CM age shown is upper limits on the age since not dereddened.

[b] "Old" = Age estimate off calibration chart to the old extreme, "Young" = Age estimate off calibration chart to the young extreme

The CM ages show dramatic differences between the IMF's for the unresolved knots. For instance, the NGC 3396 unresolved knot CM age goes from 900 Myr at α=2.35 to 200 Myr at α=3.30. In both unresolved knots, the α=3.30 age is younger than the α=2.35 age which makes sense. For a given mass of star formation at constant metallicity, more hot young stars relative to older stars means a younger burst. Since the α=3.30 IMF makes more low mass stars for a given high mass star than the α=2.35 IMF, it appears to age "faster" (i.e. The ratio of high/low mass stars decreases faster). This results in a younger age for a given ratio. This difference gets magnified in the continuous starburst case by the constant production of new stars. Therefore theory predicts, and the data confirm, that ages derived from the continuous starburst case are sensitive to the assumed IMF.

In closing we note that while the unresolved knots are predicted to be best fit by continuous starburst models, the ages derived may not be representative of the underlying physical situation. We know from the measurement knots that the unresolved knots seem to actually be made up of several instantaneous starburst knots of different ages which are perhaps mixed with older preexisting populations. The continuous starburst model derived age is significantly older than the age of the instantaneous starbursts that make it up. This is a natural consequence of the fact that our continuous models are not superpositions of multiple instantaneous models and older populations and are thus a poor surrogate for the physical phenomena we are attempting to model. Therefore we caution the reader to exercise caution in interpreting age estimates from continuous starburst models of unresolved knots.

We now turn our attention to the instantaneous starburst models. When the UM fits are acceptable (have an RMS < 0.2), the UM age estimates yield very young knots.

These ages are consistent with the observed WR bump in the spectra, the strong UV continuum flux and the strong P Cygni line profiles in the UV. All of these are hallmarks of hot young stars: a strong UV continuum is indicative of O stars, which only live ~10 Myr, WR stars are 3-5 Myr old evolved O stars, and P Cygni profiles are signatures of massive O stars with intense stellar winds. In the rest of this paper, when we say an age is reasonable, we mean that the derived age is consistent with the presence or absence of some or all of these spectral features.

The CM ages are almost always 2-10 times older than the UM ages when we are able to calculate both for the same knot. (The only exception is knot C1 with $\alpha=3.30$ where the CM and UM age are approximately equal.) To a certain extent this is to be expected. The UM age estimate is sampling only the starburst population, and only the youngest part of that population. The continuum fit method is sensitive to all populations present, including older stars that are not part of the starburst, but are physically colocated along the same line of sight. Therefore this age disparity is somewhat to be expected. However the CM ages are inconsistent with the Wolf-Rayet and O star features. Since the UM ages are consistent with these features, we conclude that the UM ages are more representative of the active star forming regions of the knot.

We have mentioned the limitations of the CM technique previously. It appears that the net result of these limitations is an overestimation of the age, at least when the UV is strong enough to calculate a UM age. It may be that when the UM ages cannot be calculated due to a weak and/or featureless UV spectrum, that the CM ages would be reasonable; however we have no data to that effect. Rather, for the instantaneous starburst case we conclude from these data that when the UM age is available, it should

be used instead of the CM age. When the UM age is unavailable, the CM age is all that is available, but may be off by as much as an order of magnitude.

Finally, we note that for the measurement knots with instantaneous starburst models the UM and CM ages derived from the $\alpha=2.35$ IMF are almost always within an error bar of the corresponding UM and CM ages derived with the $\alpha=3.30$ IMF. (The only exception is NGC 3396 knot C1 CM age, which we will discuss in the combined age analysis section) This makes sense because in the instantaneous case, unlike the continuous case, without the constant supply of new stars the differences between the two IMFs do not magnify, and thus the ages derived are largely insensitive to the IMF in the instantaneous starburst case.

UV Power Law Exponent Age Estimates

In addition to the synthetic spectra, SB99 provides the expected age as a function of several other parameters. We attempt to use these parameters to estimate the ages as well. Where required, we employ previous results from the CM and UM age estimates to resolve ambiguities.

In SB99 a calibration is defined between the spectral index β and the age, where β is defined as $F_\lambda \propto \lambda^\beta$. Specifically, they defined the slope at 1550 Å, β_{1550}, as the two point linear fit to the continuum at 1280-1320 Å and 1780-1820 Å.

Unfortunately, the G140L grating used provides data up to only approximately 1700

Å. We used the IRAF task CONTINUUM to measure the continuum power law and fit

the log/log plot to a line and excluded regions with absorption from our calculation. The

regions used in our calculation were λ=1265-1285 Å, 1340-1370 Å, 1410-1500 Å,

1560-1630 Å, and 1645-1690 Å.

We attempted to employ the SB99 β_{1550} age calibration, but the β_{1550} we measured

was frequently much steeper than the calibration allowed for. Since we were not

measuring the spectral slope in precisely the same manner as SB99 we sought to assess

the sensitivity of the measured slope to the measuring technique. For each SB99

"Stellar+Nebular" model we calculated the spectral index using the SB99 wavelength

regions, β_{1550}(SB99), and using our wavelength regions, β_{1550}(Measured). We found that

the calculation of the slope is <u>extremely</u> sensitive to the exact spectral regions used and

the exact method of calculation.

We plot β_{1550}(SB99) against β_{1550}(Measured) in Figure 19, along with a least squares

fit line, given by the equation

$$\beta_{1550}(SB99) = \beta_{1550}(Measured) * (1.054 \pm 0.028) + (0.397 \pm 0.070) \quad (12)$$

where β_{1550}(SB99) is the slope as calculated in SB99 and β_{1550}(Measured) is the slope as

we have calculated it.

The RMS = 0.126 between the data and the fit is a good match to the data over the

typical regions of interest from our data ($\sim$-3.0 $\leq \beta_{1550} \leq$ -2.0). For $\beta_{1550} > \sim$ -2.0, the trend

is correct, but the scatter is larger. We applied this correction to the data to translate the

slope as measured into the equivalent slope in the SB99 convention and present the results in Tables XXXII and XXXIII. In the tables, column (1) is the knot name; and column (2) is the measured spectral index corrected by equation . We will define the other columns later, as they are discussed.
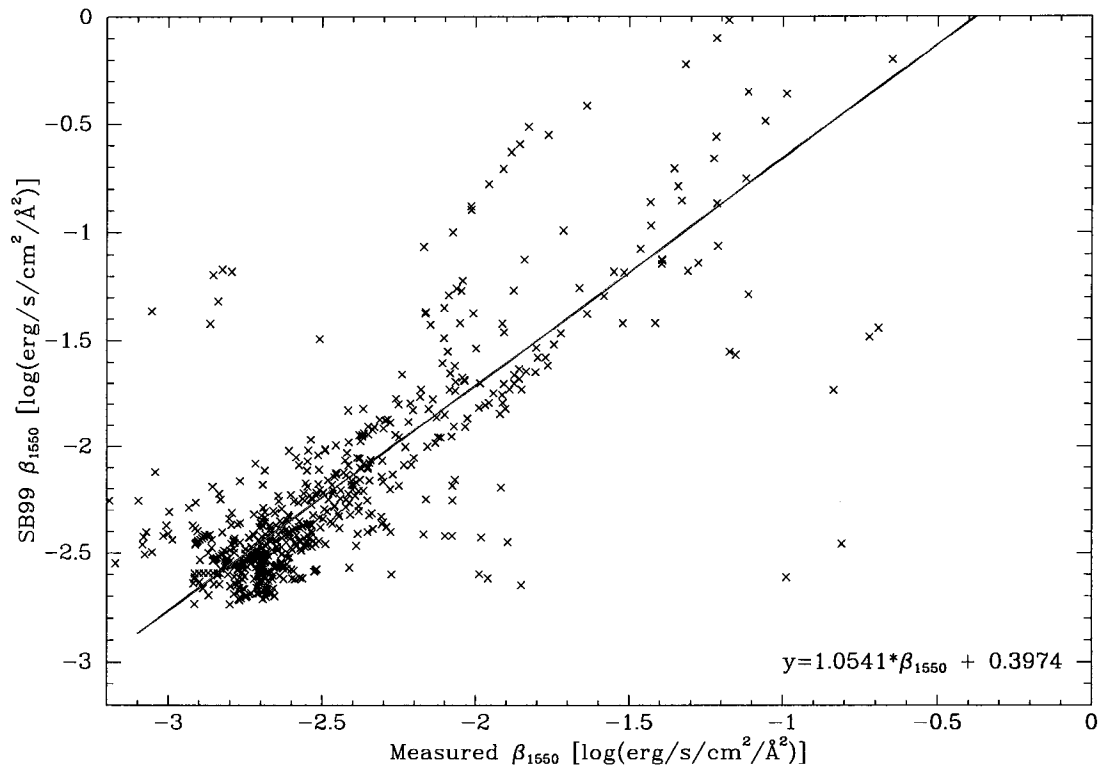
Figure 19 UV Spectral Slope Correlation

The results of the age determination are presented in Myr in Tables XXIV-XXXI column (4) where the error value is the error associated with the value $\pm$ 0.126 (the RMS of the fit given by equation). It was frequently the case that the spectral index calculated from our observed spectra and corrected by equation was beyond the SB99 spectral index calibration chart maxima/minima and we were unable to calculate an age estimate. When this was the case, we entered "Old" in the tables for knots whose β_{1550}

age is beyond the calibration chart to the old age extreme or "Young" in the for knots whose β_{1550} age is beyond the calibration chart to the young age extreme.

Table XXXII. NGC 3395 Calculated Colors and Spectral Slope

Knot	β_{1550}[a]	U-B	B-V	V-R	V-I
D[b]	---	---	---	---	---
C80	-2.76	-0.92	-0.01	0.37	0.66
C70	-1.40	-0.91	0.00	0.30	0.48
C60	-2.23	-0.88	-0.08	0.17	0.35
C1	-2.69	-0.96	-0.20	-0.07	-0.27
C2	-2.16	-0.98	-0.16	0.04	-0.12
C3	-2.39	-1.03	-0.14	0.14	-0.05
C4	-2.23	-0.89	-0.03	0.27	0.41
C50	-2.47	-0.88	0.02	0.32	0.54
B	-2.34	-0.82	0.00	0.41	0.72
A	-2.07	-0.87	-0.05	0.31	0.62
NGC 3395	-2.89	-0.87	-0.02	0.25	0.47

[a] Corrected to SB99 value using equation

[b] Knot not dereddened because Hα or Hβ unavailable. "---"denotes value not calculated for this reason.

Table XXXIII. NGC 3396 Calculated Colors and Spectral Slope

Knot	β_{1550}[a]	U-B	B-V	V-R	V-I
S3[b]	---	---	---	---	---
S1[b]	---	---	---	---	---
S2[b]	---	---	---	---	---
S10[a]	---	---	---	---	---
R[b]	---	---	---	---	---
R10	-2.64	-0.57	-0.07	0.15	0.19
R20	-2.59	-0.35	0.15	0.43	0.72
Q3	-2.66	-0.76	-0.00	0.29	0.48
Q2	-2.78	-0.91	-0.13	0.18	0.19
Q1	-1.76	-1.06	-0.17	0.16	0.03
Q30	-3.84	-0.97	-0.11	0.27	0.29
Q20	-2.98	-0.75	-0.12	0.10	0.17
Q10	-3.49	-0.61	-0.03	0.09	0.35
P2[b]	---	---	---	---	---
P	-3.40	-0.75	-0.02	0.28	0.68
O	-0.81	-0.77	-0.01	0.31	0.72
N	-0.81	-0.52	0.22	0.54	1.17
M[b]	---	---	---	---	---
NGC3396	-2.35	-0.67	0.00	0.22	0.41

[a] Corrected to SB99 value using equation

[b] Knot not dereddened because $H\alpha$ or $H\beta$ unavailable. "---"denotes value not calculated for this reason.

Equivalent Width Age Estimates

We also attempted to assess the starburst age using the SB99 $H\alpha$, $H\beta$ and He II

$\lambda4686$ Å equivalent width (EW) age estimates. We have already presented the measured

EWs in Angstroms for $H\alpha$, $H\beta$ and He II $\lambda4686$ Å in Tables IX and XI. The

corresponding $H\alpha$, $H\beta$ and He II $\lambda4686$ Å ages estimates in Myr are presented in Tables

XXIV-XXXI columns (5-7) respectively. The error values presented are the ages

evaluated from the EW ± the EW measurement errors. We entered "n/a" when we were unable to calculate the estimate due to a lack of emission in the line of interest. It was frequently the case that the EW measured from our observed spectra was beyond the SB99 corresponding EW calibration chart maxima/minima and we were unable to calculate an age estimate. When this was the case, we again entered "Old" or "Young" as appropriate for the age estimate in the tables.

The He II λ4686 emission is generated by Wolf-Rayet stars. These stars are evolved Of stars, and typically develop ~ 3Myr into the Of star's evolution. They are so massive and have such great stellar wind that they only survive for another ~ 2 Myr, so their mere presence places very tight constraints on the age of the starburst—approximately 3-5 Myr. A difficulty we encountered was that SB99 uses the EW of He II λ4686 alone as the input to the age estimation, while we measured the WR λ4686 bump which has the line blended with several other lines. Even though we are unable to deblend the line, we used this calibration for two reasons. First, as has been mentioned, the WR bump is indicative of WR stars which are very short lived. Second, the He II λ4686 age calibrations are effectively delta functions, particularly in the instantaneous case. Therefore the mere presence of the line effectively indicates the age, not the magnitude of the equivalent width, particularly in the instantaneous starburst case. We will use this as a constraint on the other methods. Knowing that we have WR stars the age must be very young, or the starburst must be continuous. We note that our inability to deblend the lines may account for the prevalence of knots for which the He II λ4686 age is off the scale to the young extreme.

Just as we did in the WR section, since we always attempted to measure the WR bump, regardless of whether it was obvious in the spectrum, we demanded that the equivalent width be at least greater than its associated error in order to use it for an age estimate. By observing this restriction we eliminate spurious results that are inconsistent with the other observed spectral features (P Cygni profiles, strong UV continuum, etc.)

Our $H\alpha$ $\lambda 6563$ measurements are extremely contaminated by the [N II] $\lambda\lambda 6548,6583$ emission lines. We were unable to deblend the lines which can result in as much as a 40% overestimate in the flux value of $H\alpha$. Despite this, we calculated the age using the blended $H\alpha$ + [N II] equivalent width. It will be shown that our $H\alpha$ and $H\beta$ age estimates are in good agreement, implying that the amount of contamination, while potentially significant, did not unduly bias our age estimates.

SB99 Color Age Estimates

In SB99, Leitherer et al. have convolved their synthetic spectra with several filters to create synthetic color indices. We have done the same by using the STSDAS package SYNPHOT to calculate the synthetic color indices (U-B), (B-V), (V-R) and (V-I) from our spectra. We blueshifted our observed spectrum back to the rest frame, dereddened it and convolved it with the associated Johnson filter pass bands to calculate the color index at the source. When we were unable to perform the dereddening due to a lack of $H\alpha$ or $H\beta$, we did not perform this analysis. Leitherer et al. (1999) caution that the (V-R) color index calculated from their synthetic spectra includes continuous nebular emission, but excludes nebular emission lines. In order to take this into account, we replace the strongest emission lines, $H\alpha$ $\lambda 6563$, $H\beta$ $\lambda 4861$, $H\gamma$ $\lambda 4340$, [N II] $\lambda\lambda 6548,6583$, [O II]

$\lambda3727$, [O III] $\lambda\lambda4959,5007$, and [S III] $\lambda\lambda9069,9531$ with the average flux calculated by linear interpolation of the continuum shortward and longward of the lines.

We had some trouble using the published calibrations. In an effort to calculate these synthetic colors for our measured spectra, we researched the exact color calculation method employed by SB99. We present the following for the interested reader who may attempt to use the SB99 color index calibrations.

According to SB99, the "filters are in the Johnson (1966) system. The zero point is defined by a star with $Z = 0.020$, $T_{eff} = 9400$ K and log g $= 3.95$, which has zero colors in all passbands." We examined Johnson's 1966 paper, but in it he does not publish passbands. Buser & Kurucz (1978) have published synthetic passbands (which are the ones that SYNPHOT uses) that were calibrated against Johnson's 1966 paper. We assume these bands are the correct ones.

Next we sought to examine the zero point reference. We determined that the zero point reference is the model of Vega by Kurucz (1979a). This model is distributed with SYNPHOT, and resides in the file "crgridbk$bk_s0004.fits." We compared the color indices generated by this model and by the standard SYNPHOT "vegamag" calibration, which uses real Vega data, not a model. There is a maximum difference between the two calibrations of only ~0.014 mag so using "vegamag" should be sufficient.

The next step we took was to calculate the SYNPHOT U-B, B-V, V-R and V-I color indices for the SB99 synthetic spectra and evaluate them against the corresponding published SB99 color age calibrations. While the color-age relationships don't differentiate between "Stellar Only" and "Stellar+Nebular" models, our calculated colors indicate that the published color-age relationships are actually for the "Stellar+Nebular" models and "Stellar Only" models can have significant errors for ages < ~10 Myr. For

example, in Figure 20 the dotted line is the published color-age relationship (in this case

V-I, continuous starburst, SB99 metallicity "b" or Z= 0.020), the triangles are the color

indices we calculated from the "Stellar Only" models at the various model ages and the

squares are the color indices we calculated from the "Stellar+Nebular" models at the

various model ages.
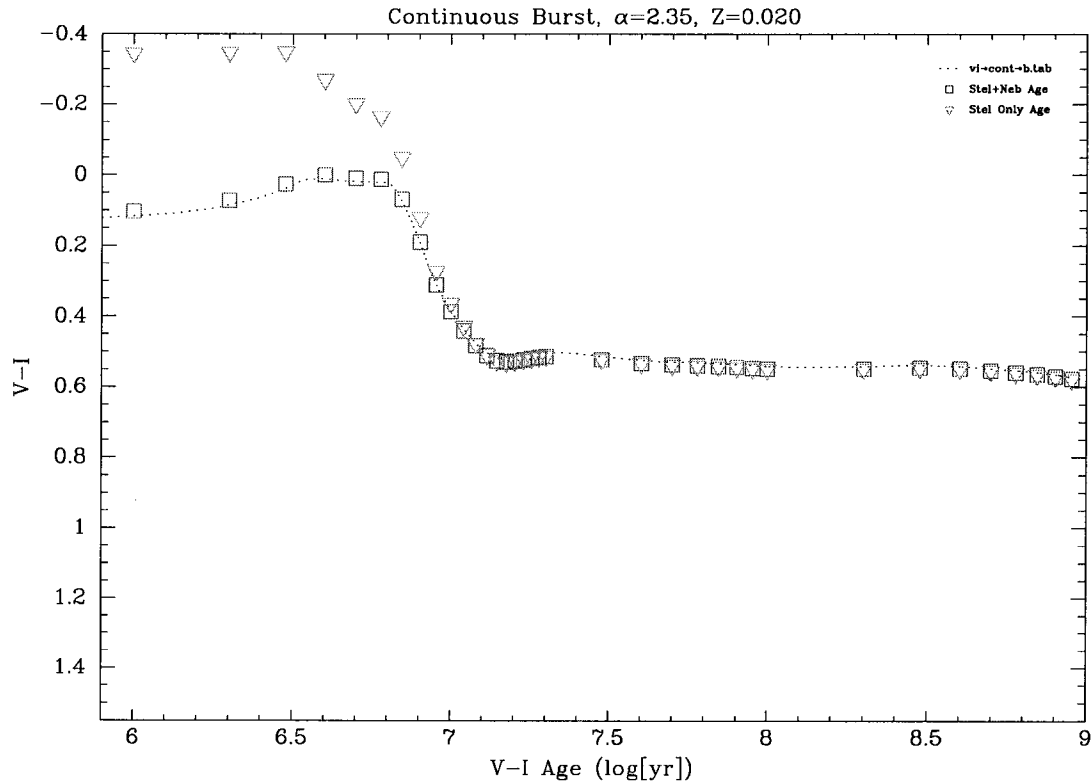
Figure 20. Sample Color Diagnostic

The calculated color indices are presented in Tables XXXII and XXXIII. Columns

(3 - 6) are the calculated U-B, B-V, V-R, and V-I colors. One difficulty in using the

SB99 color indices is that most of them are multiple valued—for a given color, there are

several possible ages. The plots in the published SB99 use a log scale on the time axis

which conceals a rapid color index oscillation early in the galaxies development (age < 6

Myr) in addition to the oscillations at age ~ 15 Myr which are visible. Therefore we can

present only the range of ages that a given color value is consistent with and then see if

one of these ages is consistent with the age derived from one of the other methods. This severely limits the predictive power of these estimation techniques. The results of the age determination are presented in Myr in Tables XXIV-XXXI in columns (8-11). It was frequently the case that the color index calculated from our observed spectra was beyond the SB99 color index calibration chart maxima/minima and we were unable to calculate an age estimate. When this was the case, we entered "Old" or "Young" as appropriate for the age estimate in the tables.

Age Estimation Technique Comparisons

In the previous sections we have described the methods we used to estimate the ages of the starburst knots and the results of those estimates. Now we will compare the various methods against each other to look for corroboration of the estimates with each other. The primary tool we will use will be the age estimate comparison plots of Figure 21a-j. In a manner very similar to that which we performed on the metallicity estimates, we will examine the ages. For brevity, we will denote the age derived from a particular technique that technique's age. For instance, rather than writing "the age derived from the $H\alpha$ equivalent width age estimation technique," we will just refer to the "$H\alpha$ age."

In what follows, we use the results we have derived up to this point. As was shown in the starburst type section, we will assume that all measurement knots are undergoing an instantaneous starburst, rather than a continuous starburst. We will further assume that both unresolved knots are undergoing continuous starbursts, rather than instantaneous starbursts, even though we know that they are actually made up of several smaller instantaneous bursts and preexisting populations which are older and co-located or in the same line of sight.

As we have previously discussed, the UM age estimate is expected to be the most representative of the young starburst population. In what follows we will assume that the UM age estimate is the most representative of the age of the hot young stars.

β_{1550} Age Comparison

Examining figure 21a, the spectral slope age estimate is in poor agreement with all of the other estimates. Despite our attempts to correct for the difference in calculation method, we were unable to obtain results that were credible in relation to the other techniques, in particular the UM or CM ages. This technique is also extremely sensitive to the reddening law assumed, and any perturbation of the reddening law will directly manifest itself in the spectral slope. We assumed the Calzetti (1994) reddening law, which was the best choice available, but it almost certainly did not provide the exact reddening we were actually observing. We conclude that our attempt to compensate for our inability to calculate the spectral index in exactly the same manner as SB99 was unsuccessful and we recommend against attempting to use this age estimate when unable to calculate the spectral slope exactly as SB99 did.
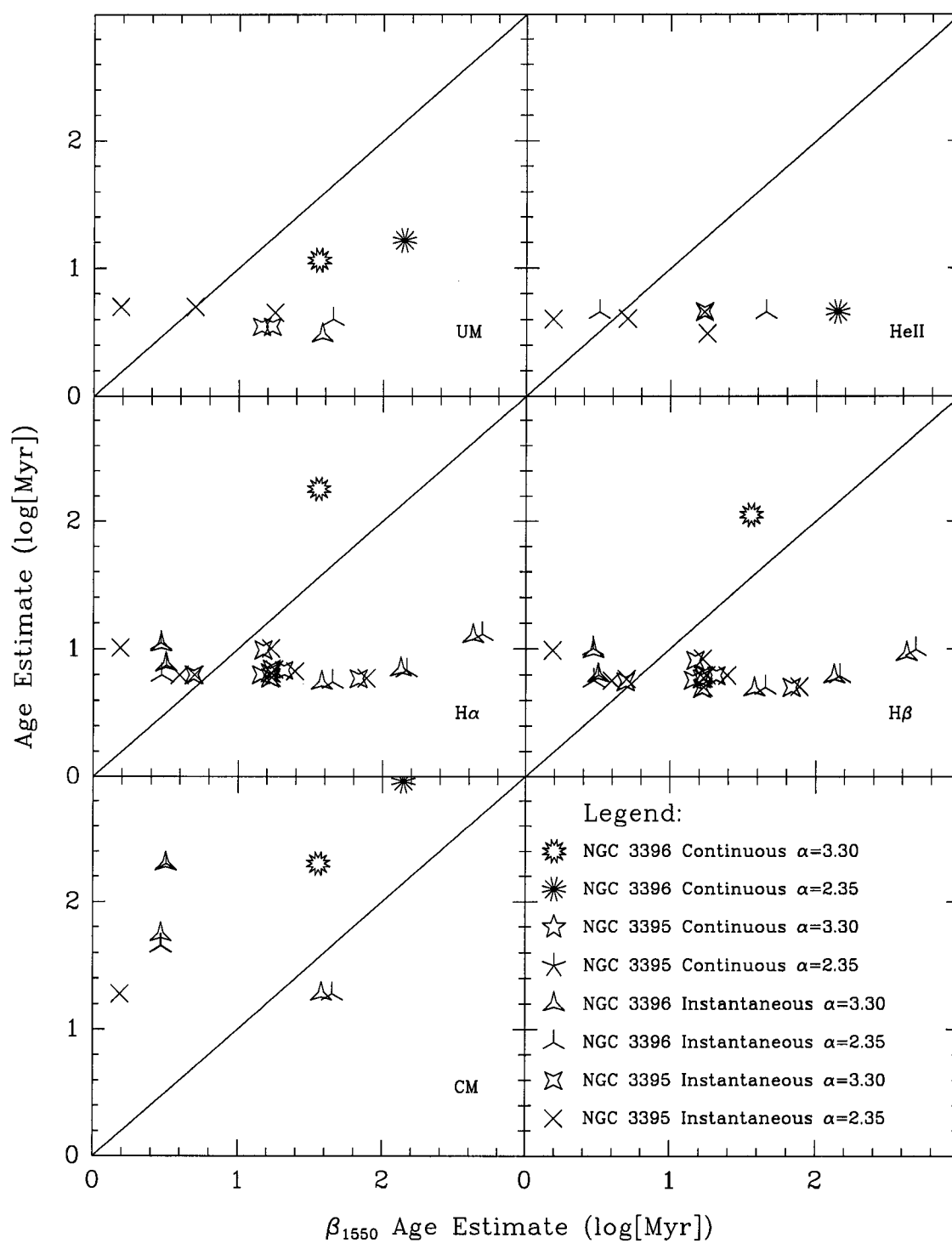
Age Estimate (log[Myr])

2

1

0

UM

HeII

2

1

0

Hα

Hβ

2

1

0

CM

Legend:

NGC 3396 Continuous $\alpha=3.30$

NGC 3396 Continuous $\alpha=2.35$

NGC 3395 Continuous $\alpha=3.30$

NGC 3395 Continuous $\alpha=2.35$

NGC 3396 Instantaneous $\alpha=3.30$

NGC 3396 Instantaneous $\alpha=2.35$

NGC 3395 Instantaneous $\alpha=3.30$

NGC 3395 Instantaneous $\alpha=2.35$

0   1   2   0   1   2

β_{1550} Age Estimate (log[Myr])

Figure 21a. β_{1550} Age Comparison

Figure 21a-f. Age comparisons. Symbols are described in the legend. We have assumed measurement knots are instantaneous bursts and unresolved knots are continuous bursts. Each pane has the same x-axis but the y-axis is the age estimate labeled in the pane. The diagonal line represents x-axis = y-axis.
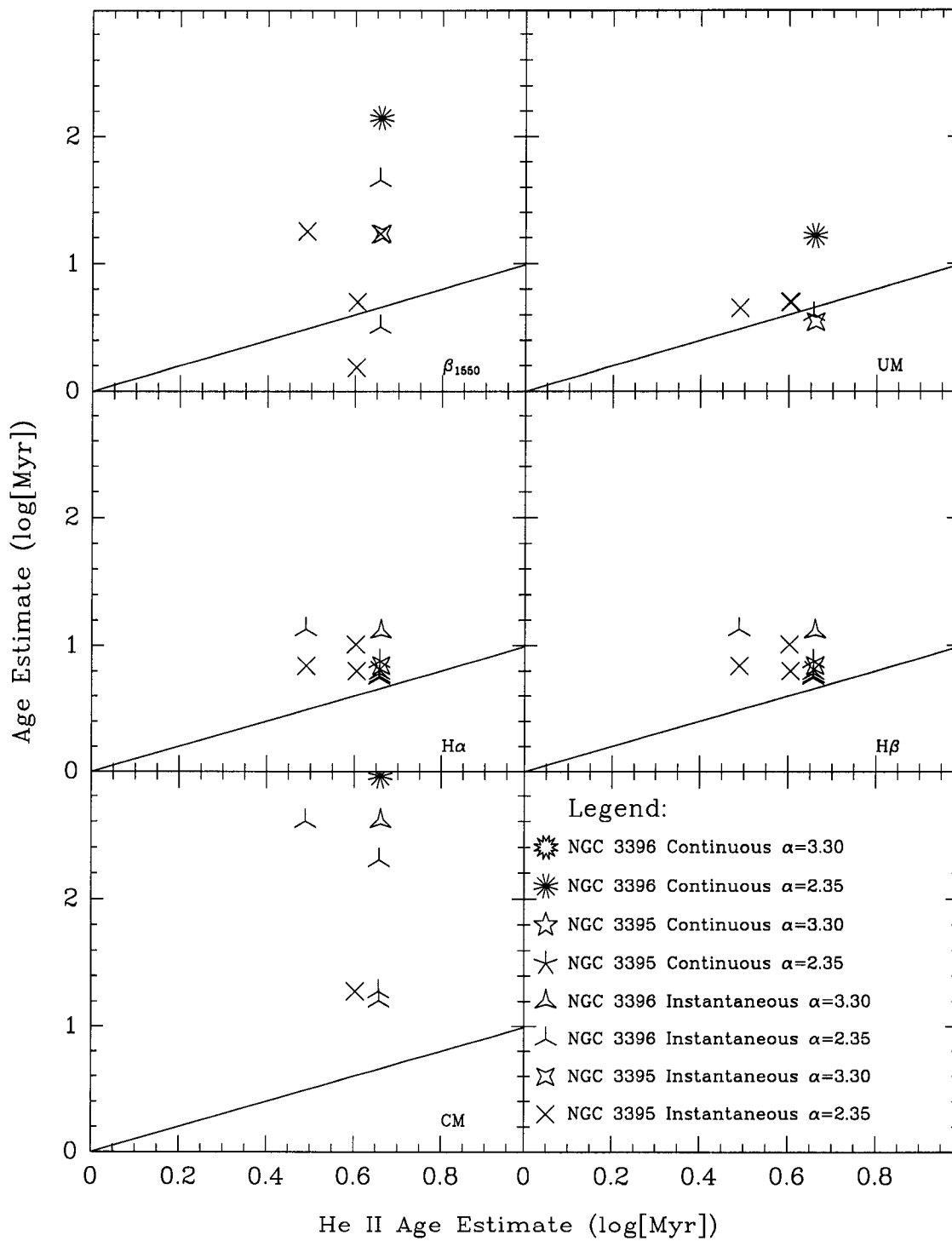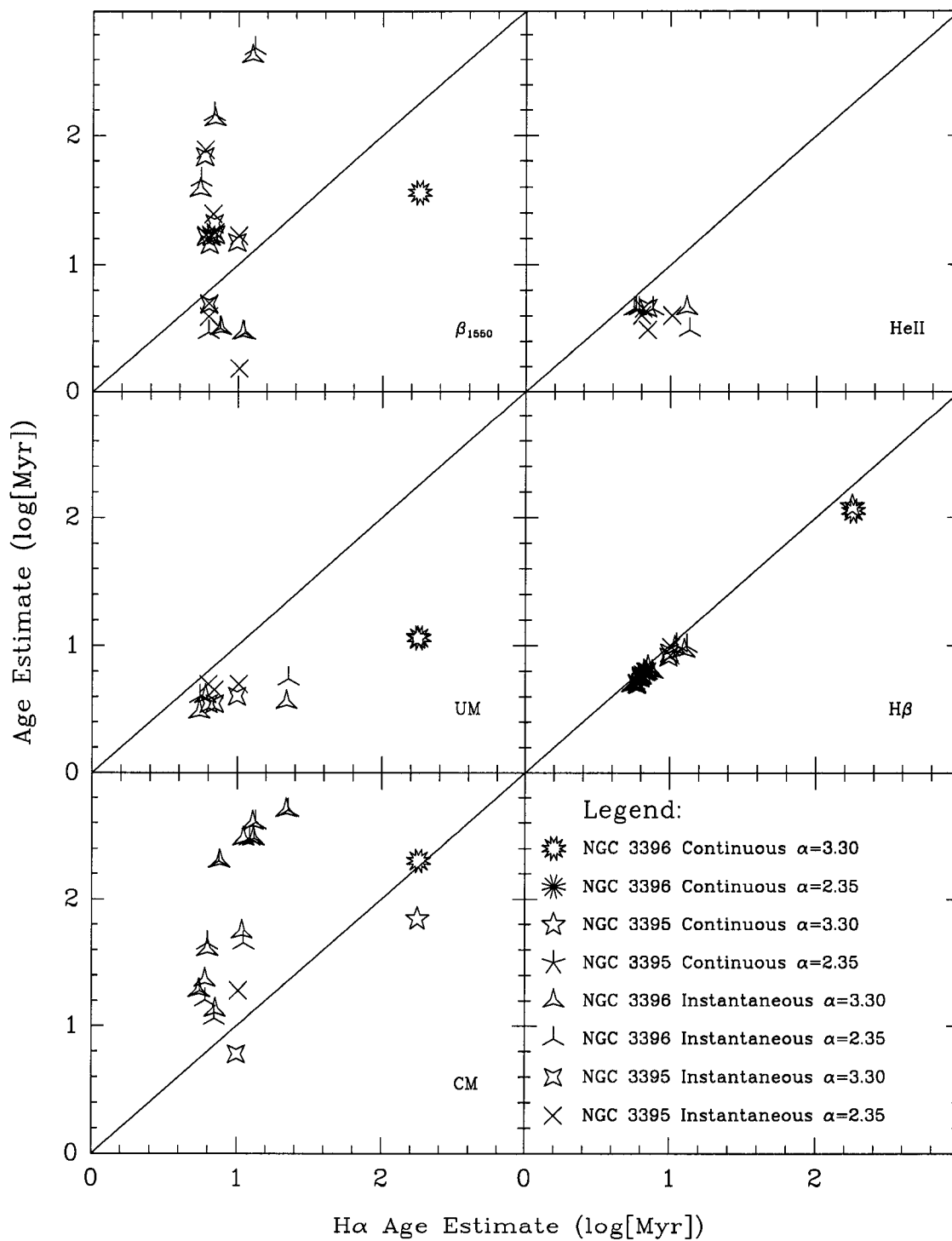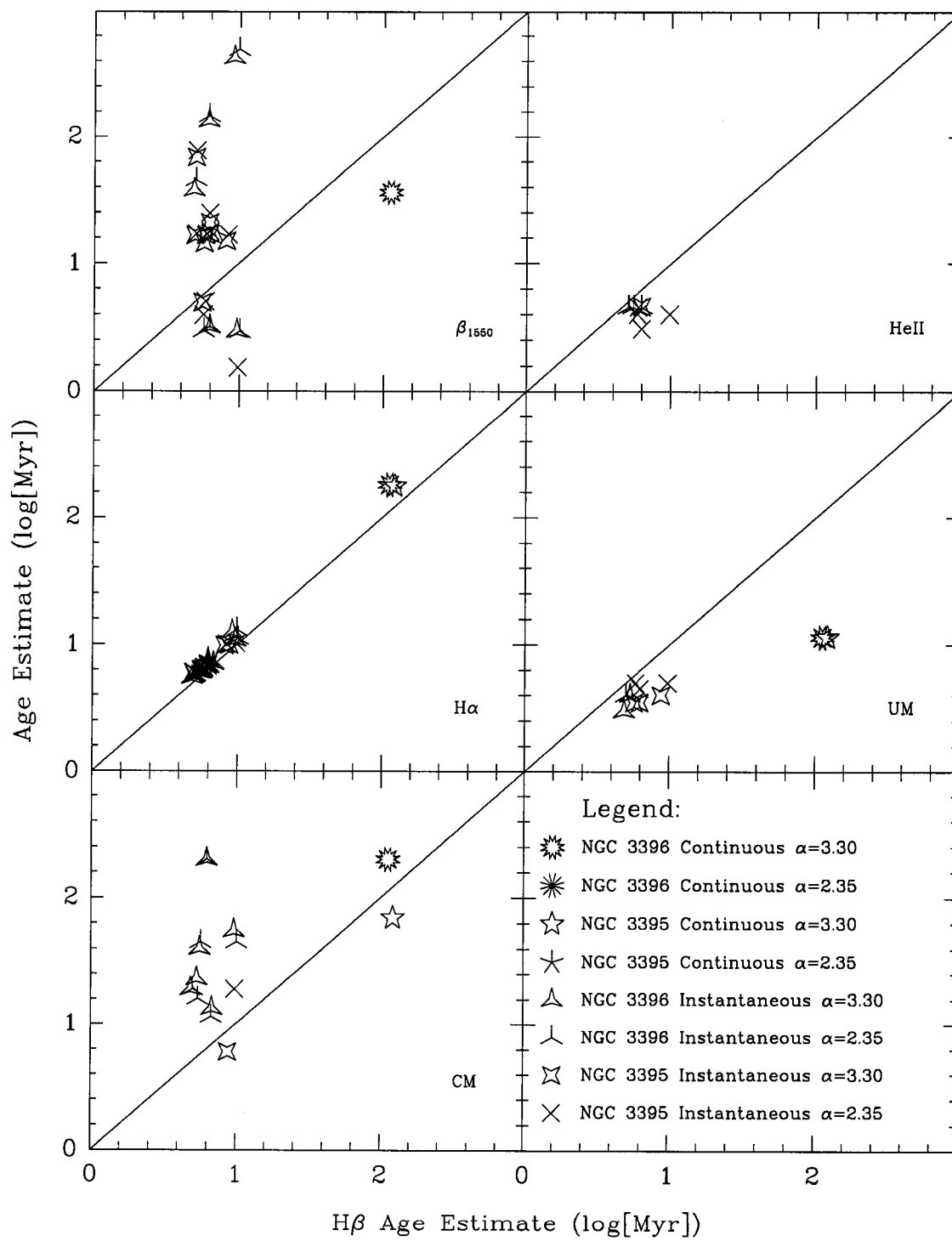
Figure 21b. He II λ4686 Age Comparison

(Note: the x-axis scale has changed for this figure due to the limited range of He II λ4686 age estimates)

Figure 21c. Hα Age Comparison
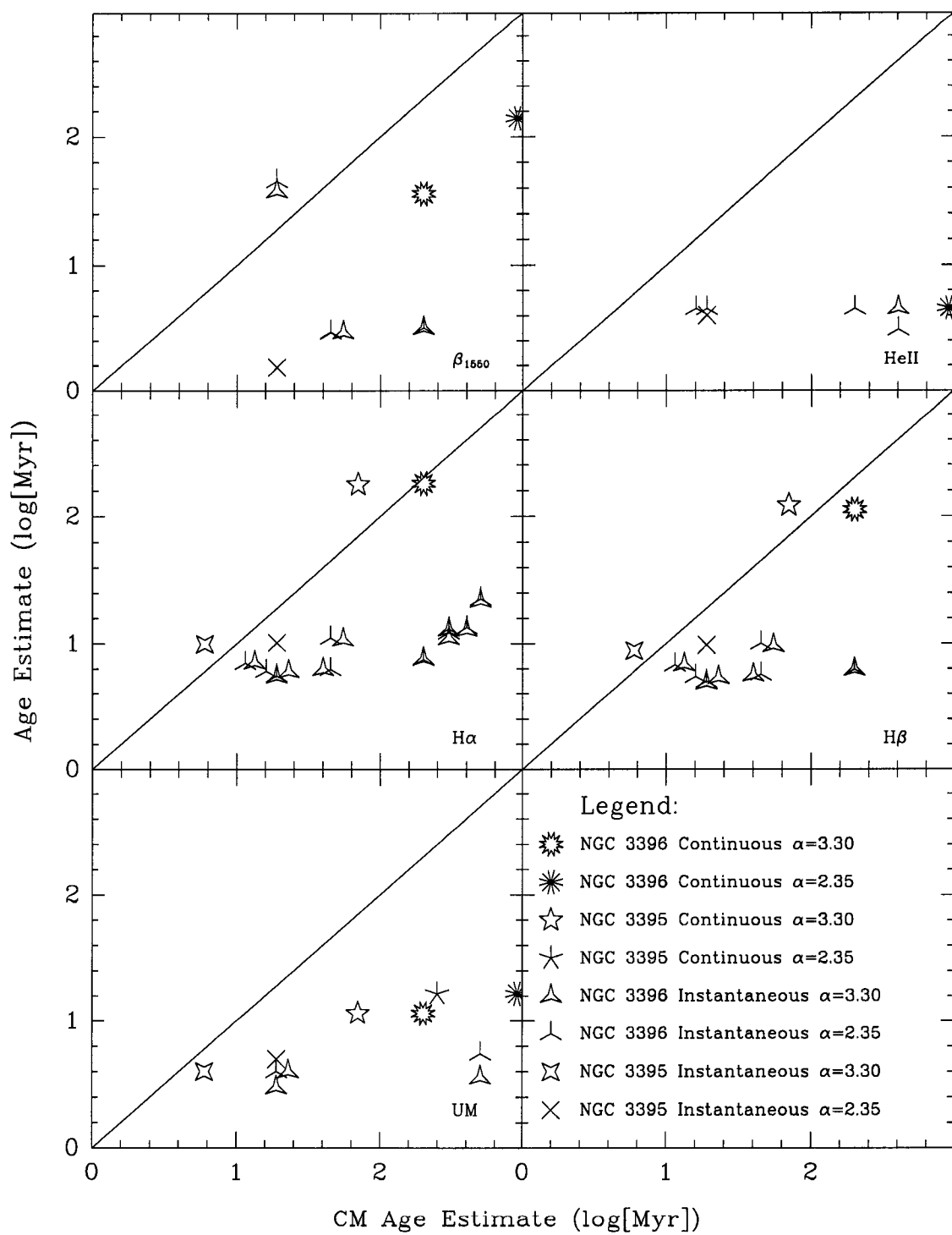
Figure 21d. Hβ Age Comparison
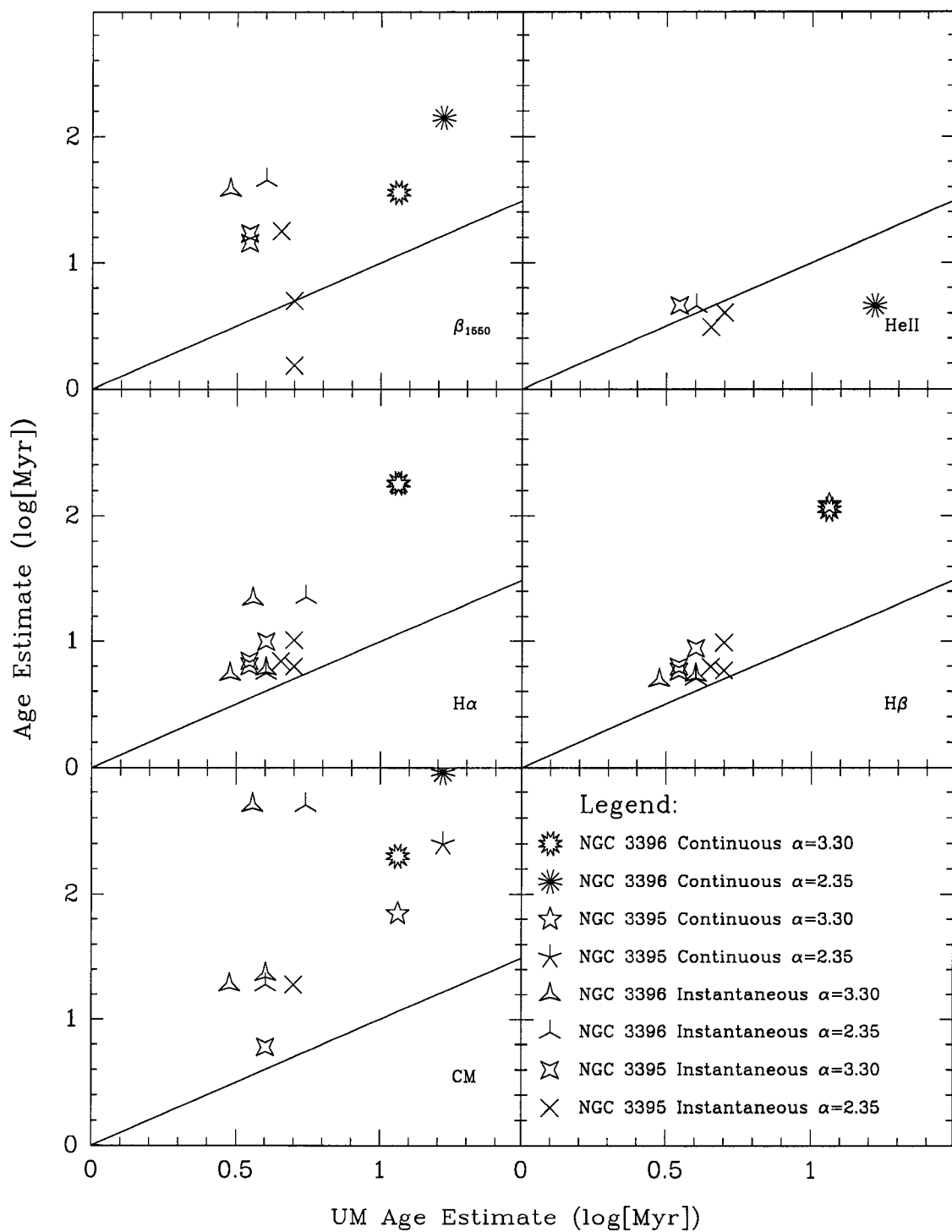
Figure 21e. CM Age Comparison

Figure 21f. UM Age Comparison

(Note: the scale has changed for this figure due to the limited range of UM age estimates)

He II λ4686 Equivalent Width Age

Comparison

Figure 21b shows the He II λ4686 equivalent width age comparisons. Conspicuous in this diagram are the poor correlation between this technique and all the other techniques for the continuous starburst models (shown as stars and asterisks). Despite the limitation previously mentioned about our inability to deblend the WR bump, the He II λ4686 age estimate is in excellent agreement with the UM age estimate. As we suspected, for instantaneous starburst models when the He II λ4686 equivalent width yields an age, most of the other methods will also yield a young age. Hα, Hβ and the UM age estimates are always $< \sim 10$ Myr when the He II λ4686 method yields an age. There is no apparent correlation between it and the β_{1550}, or CM age estimates.

Based on these data we conclude that the He II λ4686 age estimation technique works well for knots that can be modeled by instantaneous starbursts. This technique is not appropriate for continuous starbursts. We also find that when the He II λ4686 bump is present, the Hα, Hβ, and UM age estimates are consistent with ages $< \sim 10$Myr.

Hα and Hβ Equivalent Width Age

Comparison

The middle right panel in Figure 21c depicts the variation of the Hβ age estimate with Hα. As can be seen, they are in excellent agreement. This is somewhat surprising because as was discussed previously, our Hα measurements are extremely contaminated by the [N II] λλ6548,6583 emission lines which can cause as much as a 40% overestimate in the flux value of Hα. Nevertheless, our Hα and Hβ are strongly correlated, producing

nearly identical results. This implies that the [N II] contamination, while potentially severe, does not unduly bias the Hα age estimate and we conclude that one can employ the Hα age estimation technique even if one is unable to deblend the [N II] line contamination. This is of particular utility in extragalactic observations where one is frequently driven to lower spectral resolution due to sensitivity and signal to noise constraints. We also note that the Hα and Hβ data were independently collected on different observations, with different gratings. The fact that they are in such good agreement gives us confidence in the quality of the calculations and data reduction that we have performed.

There is no correlation of Hα or Hβ with the β_{1550} age. They diverge from the UM age almost immediately and are always older than the UM and He II ages. They are typically younger than the CM age and show no correlation with the CM age for instantaneous starbursts. The CM age for both unresolved knots modeled by continuous starbursts with α=3.30 correlate well with the corresponding Hα and Hβ ages, but as this is only based on two data points, the conclusion is weak.

A priori we expect the Hα, Hβ and UM ages to be well correlated. The strength of the UV flux which drives the UM age also generates the Balmer photons that drive the Hα and Hβ ages. The fact that they aren't well correlated with the UM age is troubling. Upon further analysis, there are actually two areas of concern.

First, when the UM age exists, the Hα and Hβ ages are older than the UM age. This may be explained if the equivalent width of Hα or Hβ that we measure is actually lower than the SB99 models would have predicted for a given age (smaller equivalent width

implies older age). If so, the reduced equivalent width could be a result of either or both of the following:

1. The SB99 models take into account only stars with masses greater than 1 $M_\odot$; however stars with masses below 1 $M_\odot$ still contribute to the visible continuum at 6563 Å, potentially biasing the EW down.

2. If the knot were not radiation bound, then the assumptions break down in the models. We already know that this is happening on a massive scale in knot C1, the super bubble, and it may be happening on a smaller scale elsewhere. If ionizing photons are escaping then they will not be recycled into Balmer line flux, and the flux in the Balmer lines will be reduced, reducing the equivalent width as well.

Either of these explanations could be sufficient to explain the observed fact that the $H\alpha$ ages are greater than the UM ages.

The second are of concern is that when the UM age for a knot is not available, the $H\alpha$ and $H\beta$ age estimates still give very young ages. Since there is no UM age we must be dealing with either a very weak starburst, or an older population not undergoing a starburst with some young stars superimposed along the line of sight. The presence of $H\alpha$ and $H\beta$ identify that there are some hot young stars present, but the age estimation technique is unable to discriminate between a starburst and standard galactic evolution/star formation. This shows up in the data as a disagreement between age estimates where the $H\alpha$ and $H\beta$ estimates are very young, but there is no corroborating estimate from one of the other techniques and the spectra do not show characteristics of hot young stars such as P Cygni profiles, or a strong UV continuum. For instance knot N

in Table XXIX or knot B in Table XXVII have very young Hα and Hβ ages, but all the rest of the estimates are much older.

For instantaneous starbursts, the assumption is that there is only one population of stars, all with the same age, and the Hα and Hβ age estimation techniques are calibrated against models built upon this assumption. SB99 uses the equivalent width as the input to the age calculation, but the equivalent width of Hα or Hβ is a function not only of the ionizing flux generating the emission, but also the optical continuum as well. While the ionizing flux is generated almost exclusively in the hot young stars which are the object of our attention, the continuum is generated by these stars, the nebular emission, and any other stellar population that may be colocated or along the same line of sight. These other stellar populations, particularly if they are older, preexisting populations or the older remnants of previous starbursts will contribute strongly to the optical continuum, lowering the equivalent width. For a given instantaneous starburst population, the age estimate in isolation without any other populations superimposed will be younger than the age estimate with any older populations superimposed. This may account for the observed disparity between the UM and Hα and Hβ ages.

A further shortfall of the Hα and Hβ age estimates is that they are always very young for instantaneous starbursts, which while sensible, can generate very young ages for predominantly older populations that have some hot young stars colocated or along the same line of sight. Therefore the Hα and Hβ age estimates may not be discriminative enough. They can be used as a weak constraint on the age of an instantaneous starburst, but they lack the power to discriminate between predominantly young populations and predominantly old populations with some young stars present along the same line of

sight. We do; however, recommend the use of the Hα and Hβ age estimates in conjunction with the He II λ4686 bump when the He II λ4686 age estimate is beyond the calibration. The He II λ4686 bump tells us that the population is predominately young and so the Hα or Hβ age is thus deemed more representative of the population.

<u>CM Age Comparison</u>

The CM age estimates are shown in Figure 21e. As can be seen the CM age correlates poorly with all of the other age estimation techniques. The CM age estimates are typically older than the corresponding UM, Hα, Hβ, or He II age estimates. We partially explain this by noting that the CM ages should be more sensitive to the presence of older populations (if any) than the other techniques that we have discussed thus far. In particular, if an older instantaneous starburst or non-starburst population is near the same line of sight as a starburst knot the CM age will be sensitive to this population and it will bias the CM age older. In the combined age analysis section we will discuss this further.

We suspect the CM age estimates are somewhat more uncertain than the other age estimates due to the shortfalls of the CM models which we have already discussed. Recall that we were forced to limit the wavelength regions of the model spectra that we considered in order to allow the fits to converge. Furthermore, the continuum models that we fit extend all the way into the IR, while we use only the portion short of 9000 Å since we have no longer wavelength data. While these limitations allowed us to get age estimates, we note that the veracity of those estimates is unknown, since we are not fitting the entire model, only a large portion of it.

UM Age Comparison

Figure 21f depicts the UM age comparison with the other techniques. It is immediately apparent from the figure that the UM age is always younger than the corresponding age estimate for the other techniques with the exception of the He II age estimate. The younger estimate with respect to the CM, Hα and Hβ age estimates is reasonable since, as we have discussed, the UM age is sensitive only to the hot young star population while the other techniques can be influenced by older populations which may be colocated with the starburst or along the same line of sight. The correlation with the He II age is excellent.

Color Index Age Comparison

As was mentioned previously, the color index age calibrations are multiple valued for most values of the color index. Acknowledging this, we reported all the possible intercept values in Tables XXIV-XXXI. Unfortunately, since we have no way to select the "best" value to use, we were unable to make age comparison charts for each of the color index ages as we did with the other techniques. We will make some general observations however about the applicability of the color index ages.

Of all the color methods, we expect the U-B index to be most sensitive to the hot starburst region since it is the bluest of the color indices. Indeed we find for the instantaneous starburst case that the U-B age estimates are almost always very young—even when a young age is inconsistent with the other age estimates, UV continuum strength, presence of P Cygni lines, etc. For those knots where the U-B age is single valued and the UM age is available, the U-B and UM age seem reasonably well correlated. This is a selection effect however; the U-B age is almost always young, as is

the UM age, but while the UM age is only available in knots that appear to be predominately young, the U-B age is always available.

We attribute the problems with the U-B age to the aforementioned continuum emission problems with SB99 continuum models. For example, in Figure 18, we can see the overlay of the Johnson UBVRI filters on our standard example spectrum, NGC 3396 knot Q1. Also plotted is the best fit to Q1 as a thick solid line. Notice that the Balmer decrement region, where we have the most disagreement between the models and the data, is basically centered in the Johnson U filter. We can see that the U-B color index calculated from the real spectrum is obviously going to be incompatible with the color index calculated from the SB99 model. The associated U-B age for Q1 from Table XXXI is so negative that it is off of the SB99 calibration (more negative = younger in this case). As a matter of fact, almost all the instantaneous starburst knots have a very young U-B age. The mismatch in the Balmer decrement region is the culprit. Almost all the observed spectra show little to no Balmer decrement in comparison to the SB99 model spectra. This extra flux in the observed spectra enhances the U filter magnitude resulting in younger age estimates, regardless of the other spectral features. Because the U-B calibration is based on these flawed models, we find that the U-B age is unreliable and should not be used.

The Johnson B filter is on the edge of the region of disagreement between the models and the data and may also be slightly biased for the same reason. Furthermore, recall that we replaced the lower order Balmer lines with the linear fit to the continuum shortward and longward of the line, but the higher order Balmer lines were too close together to treat in the same fashion. Even though the higher order Balmer lines were not removed they are much weaker than the lower order lines, so we expect the degree of age

bias to be fairly minimal. On the other end of the spectrum, the V-I color has a region longward of 10,000 Å where the Johnson I filter extends past the end of the data collection. While this region is outside the filter's FWHM, it still is a potential source of error. However, from a cursory examination of Figure 18, the B-V, V-R, and perhaps the V-I color indices calculated from the observed spectra should be very close to the corresponding SB99 model values. In knot Q1,while the B-V age is too young to calculate, there are values available in the V-R and V-I age column which are consistent with the UM burst age of 3 Myr. We can say only that they are consistent however, since there are several values to choose from. The multiple valued nature of the calibration can best be seen in Figure 22.

The calibration is double valued over almost its entire dynamic range. Furthermore, it is extremely flat for ages greater than ~15 Myr. This flatness means that a small difference in the color can result in a large age difference. The B-V and V-I calibrations suffer from similar deficiencies. Because of these reasons, the color index age calibrations can give extremely variable results and are thus impractical for our application. Therefore we advise against using any of the color index age estimation techniques as anything other than a consistency check for the other age estimates.
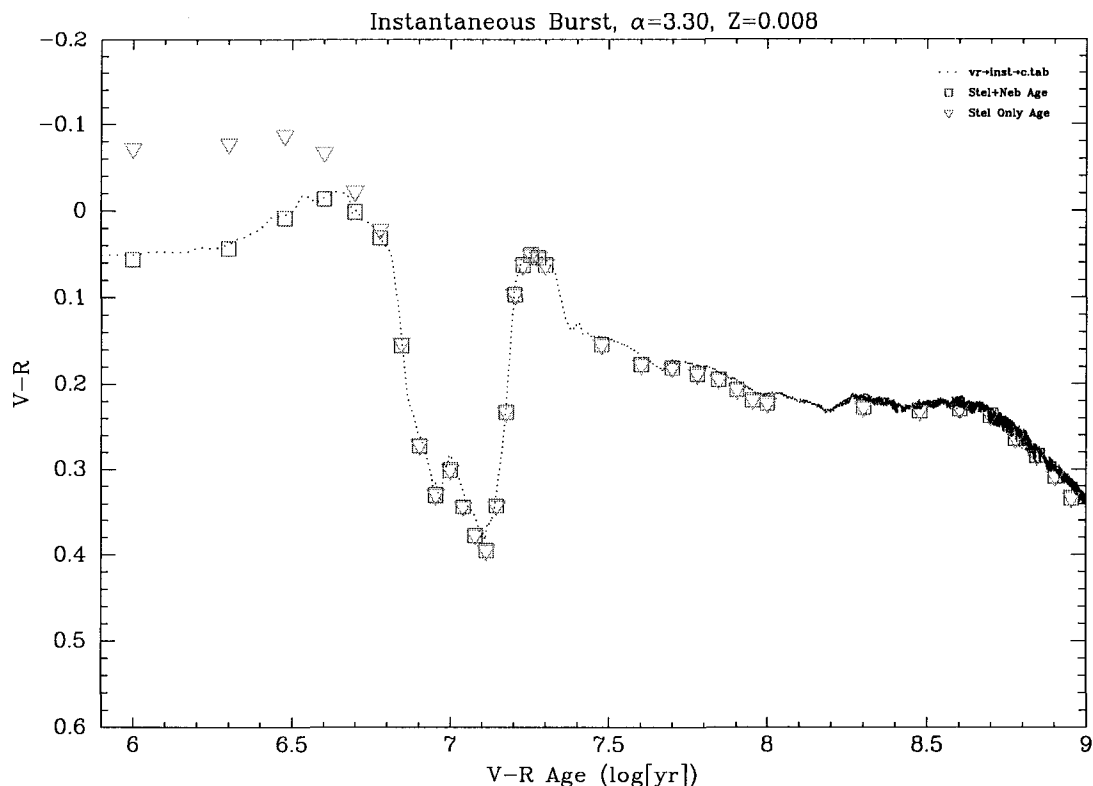
Figure 22 V-R Color Calibration for NGC 3396 Knot Q1

In this figure the triangles are the V-R color indices calculated for Stellar Only SB99 models at various ages, the squares are the V-R color indices calculated for Stellar+Nebular SB99 models at various ages, and the dotted line is the SB99 V-R color index calibration for an instantaneous starburst at SB99 metallicity "c" or Z=0.008.

Combined Age Analysis

In the previous sections we have discussed the reasonableness of all of the age estimation techniques we employed. In summary, we found that the UV feature fit age is superior when it is available, followed by the He II λ4686 age estimate (when available), followed by the Hα and Hβ age estimates when combined with the presence of He II λ4686, followed by the Hα and Hβ age estimates alone. The CM age estimate is frequently older than the other estimates and we suspect it has more error. We use it to characterize the older stellar population, particularly if there is a mixed population along

the line of sight of young starburst regions with older instantaneous, or non-starburst regions. We found that the B-V, V-R and V-I color index ages could be used as a consistency check on the other methods, but the U-B color index and the β_{1550} age estimates are not appropriate for our application.

Starburst Type

We will treat all of the resolved measurement knots as instantaneous starbursts based on our fitting analysis and the order of magnitude estimate we calculated that predicted these knots are too small to have enough mass of gas to support a continuous starburst for more than ~1-2 Myr. We will treat the unresolved knots as continuous starbursts because our fitting analysis showed that the unresolved knots are typically better fit by continuous models and they are large enough that they could contain enough gas to support a continuous starburst. For the remainder of this paper we will no longer explicitly state which type of starburst we are considering--we will discuss measurement knots only in the context of instantaneous starbursts and unresolved knots only in the context of continuous starbursts.

IMF Selection

As was already discussed in the WR section, the WR bump equivalent widths are more consistent with the Saltpeter IMF. However the fitting results showed a weak preference for the $\alpha=3.30$ IMF in NGC 3396 and a strong preference in NGC 3395. We seek to select only one IMF for the remainder of the analysis. Figure 23 shows the knot ages calculated with $\alpha=2.35$ plotted against the same knot ages plotted with $\alpha=3.30$ for each age estimation technique.

As can be seen, the ages are almost always approximately equal regardless of the

IMF assumed for all of the age estimation techniques. The Hα and Hβ ages are in

excellent agreement between the IMFs. The α=3.30 UM age estimates are always a little

younger than their α=2.35 counterpart, but the differences are very small, typically < 1
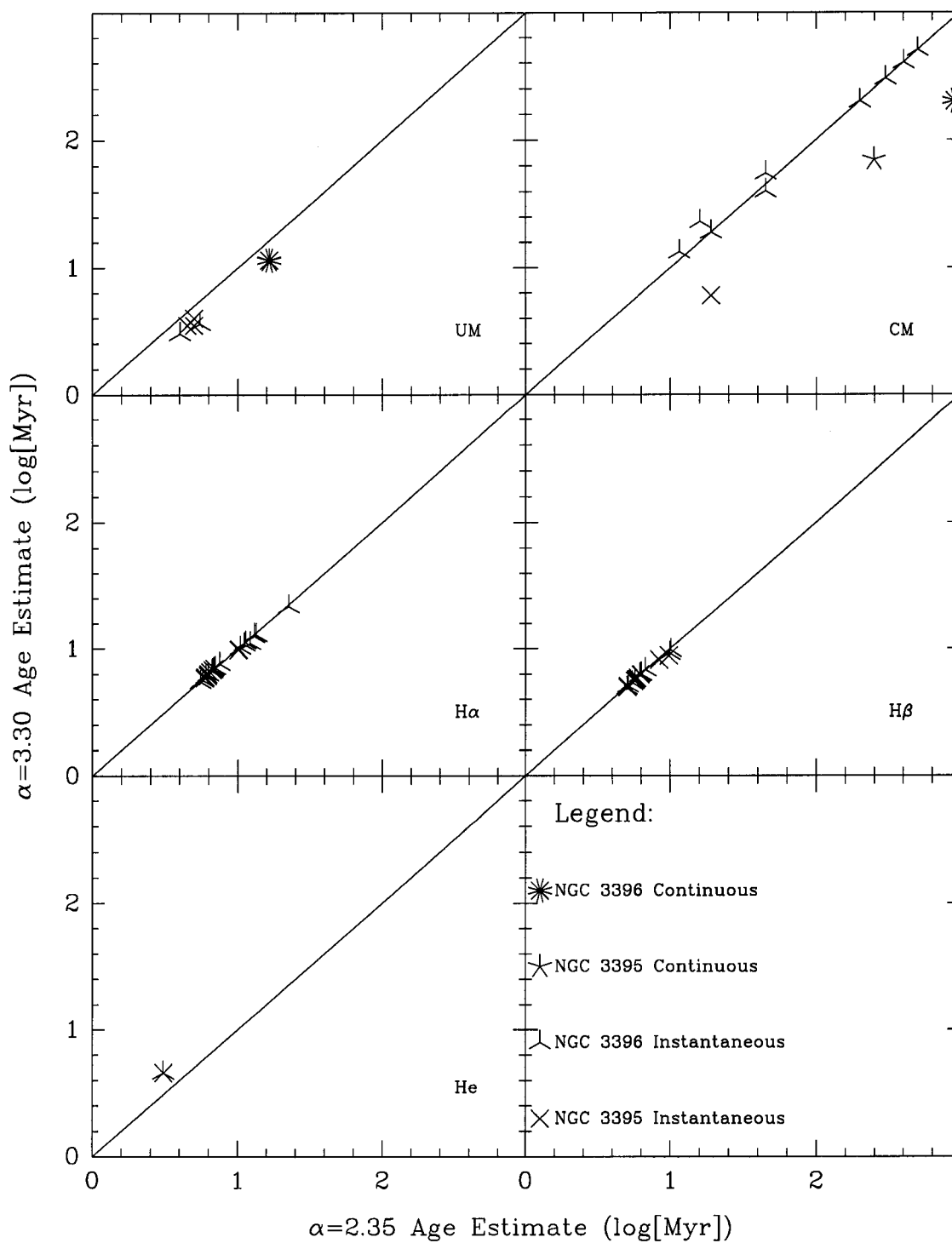
Myr, and so are no cause for concern.

Figure 23. IMF Age Comparisons

We have assumed measurement knots are instantaneous bursts and unresolved knots are continuous bursts. Each pane contains the labeled age estimate plotted with the α=2.35 estimate on the x-axis and the α=3.30 estimate on the y-axis. The diagonal line represents x-axis = y-axis.

The only technique that shows any significant disagreement at all is the CM age estimates. Both continuous starbursts (the unresolved knots, shown as a star and an asterisk) are off of the line. As was already discussed in the starburst type analysis section, for a given mass of star formation at constant metallicity, more hot young stars relative to older stars means a younger burst. Since the α=3.30 IMF makes more low mass stars for a given high mass star than the α=2.35 IMF, it appears to age "faster" (i.e. The ratio of high/low mass stars decreases faster). The continuous case magnifies any difference in IMF by virtue of the continuous star production. The hot massive stars die and are continuously replaced while the cooler stars are more long lived and thus the relative number of cool stars is enhanced as a function of time. Since the CM is sensitive to these older stars we expect to see their effect in this this technique and in fact we do. Our data show that for continuous star formation a given UV continuum strength relative to visible continuum strength gives a younger age in the α=3.30 case than in the α=2.35 case.

The other outlier in the CM plot is knot C1, the super bubble. The CM age when α=2.35 is 19.0 Myr and when α=3.30 the CM age is 6 Myr. Interestingly, the UM age when α=3.30 is 4.0 Myr and this is the only case in both galaxies where the UM and CM ages are at all close to being in agreement, which would seem to argue in favor of the α=3.30 IMF.

We can rationalize the α=2.35 answer by noting that if knot C1 actually has an older population along the same line of sight as the starburst population, then that older population would cause us to observe a mixed population with very young UV, Hα, Hβ, and He II ages and an older CM age. This is exactly what we observe. Furthermore, the

superposition of a starburst with an older population could masquerade as a softer IMF since the ratio of older stars relative to younger stars would be enhanced. Therefore a superposition of populations can explain the data regardless of the IMF we assume and we cannot eliminate the α=2.35 IMF based on the CM age.

Since we cannot eliminate α=2.35 we attempt to eliminate the α=3.30 IMF. The strongest argument against the α=3.30 IMF is the equivalent width of He II λ4686. As was previously mentioned, after taking into account the nature of the starburst (instantaneous or continuous) there are several knots which have an equivalent width more than 1 σ above the maximum equivalent width of He II λ4686 for an instantaneous starburst with α=3.30. When $Z = Z_\odot$ the maximum equivalent width is 4.8 Å, when Z=0.4$Z_\odot$ the maximum equivalent width is 2.5 Å, when Z=0.2$Z_\odot$ the maximum equivalent width is 1.5 Å. Rounding our measured metallicities to the nearest SB99 value, when α=3.30, knots C60, C1, C3, C4, Q2, Q1, and Q30 are all off the scale and knots C4, Q2, Q1 and Q30 are all more than 1 σ above the maximum. In the corresponding case for α=2.35, only C4 is off the scale, and by less than 1σ. Therefore based on these results, we reject the α=3.30 IMF for the rest of this analysis.

Knot Ages

Using the above results, we present what we deem to be the most representative ages for each knot we measured. We attempted to define a metric to denote our confidence in our estimates. Some knots have overwhelming evidence in favor of a given age and therefore we are very confident in our estimates. Other knots have very tenuous evidence for a given age and we have correspondingly less confidence in our

estimates. We defined our confidence on a 10-point scale with 0 denoting no confidence

and 10 denoting high confidence. We assigned points shown in Table XXXIV. These

points are in keeping with the previous discussion about our relative confidence in the

various techniques. The confidence metric is provided as a quick reference tool and

should not be considered a rigorous scientific calculation.

Table XXXIV. Confidence Calculation Matrix

Item	Code	Points	Comments
UM Age	U	+5	
He II Age (alone)	H	+3	
Hα Age	A	+1	
Hβ Age	B	+1	
He II Age in conjunction with Hα Age and or Hβ Age	ABH	+3.5	Can only have one value for the combination of H, A and B
CM Age	C	+1	
Color Index Age	I	+0.5, max 1.0	Each corroborating index adds 0.5 up to a maximum of 1.0
P Cygni profiles present	P	+1	
Strong UV Continuum	S	+1	UV > Visible continuum
Balmer Decrement	D	+1	Only counts toward NSB ages

In Tables XXXV and XXXVI we present the age, or ages for mixed populations, of

the knots. Column (1) is the knot name, column (2) is the age of the population, or when

we have a mixed population, the age of the starburst (SB) and older (NSB) populations;

column (3) is our confidence in the estimates as described in the previous paragraph;

column (4) is the contributors to the age estimate (see Table XXXIV); and column (5) is

for notes.

Table XXXV. NGC 3395 Combined Age Estimates

Knot	Age (Myr)	Confidence[a]	Basis[a]	Notes
D	6.2	1.0	A	Based solely on Hα. Could not deredden so no color indices
C80	6.0	4.0	ABIS	Very noisy weak UV continuum but > optical continuum
C70	5.5	5.0	ABISP	Weak P Cygni profiles, UV continuum ~ optical continuum
C60	6.2	6.5	ABHISP	
C1	SB:5.0	10.0	UCABHISP	Super bubble. Very young, very strong P Cygni, very blue continuum
	NSB: 19.0	1.0		
C2	4.5	10.0	UABHISP	
C3	5.0	10.0	UABHISP	
C4	5.5	6.5	ABHISP	
C50	6.0	5.0	ABISP	Weaker P Cygni profiles
B	SB:9.3	4.0	ABIS	NSB age based on V-R, V-I = "Old" Noisy but strong UV continuum.
	NSB: Old	0.5		
A	6.5	5.0	ABISP	
NGC 3395	SB 11.5	7.0	UCSP	Hα, Hβ, Color indices unreliable for continuous starburst so not used
	NSB 70.0	1.0		

[a] See Table XXXIV for details

Table XXXVI. NGC 3396 Combined Age Estimates

Knot	Age (Myr)	Confidence[a]	Basis[a]	Notes
S3	11.3	1.0	AD	Extremely weak. Could not deredden so no color indices, Age based on Hα only
S1	SB: 5.5 NSB: 500	5.0 1.0	UCADP	Very weak P Cygni profiles. Could not deredden so no color indices and CM age is upper limit. Hα disagrees with UM somewhat
S2	SB: 13.1 NSB: 300	1.0 1.0	CAD	Could not deredden so no color indices and CM age is upper limit.
S10	SB: 13.5 NSB: 400	1.0 1.0	CAD	Could not deredden so no color indices and CM age is upper limit.
R	SB: 12.2 NSB: 300	1.5 1.0	CAD	Could not deredden so no color indices and CM age is upper limit. Slight hints of P Cygni profiles in very high noise
R10	10.6	3.5	CABIDP	Very weak P Cygni. Continuum age disagrees with color indices. Fairly strong Balmer decrement. Probably a mixed population, but no age estimates to quantify.
R20	6.9	3.0	CABID	Continuum age disagrees with color indices Fairly flat spectrum with emission lines. Probably a mixed population, but no age estimates to quantify.
Q3	6.0	5.0	CABISP	Continuum age disagrees with color indices
Q2	SB: 5.8 NSB:16.0	6.5 2.0	CABHISP	Color indices consistent with both ages
Q1	SB: 4.0 NSB:19.0	10 1.5	UCABHISP	Color indices consistent with both ages
Q30	5.4	6.5	ABHISP	
Q20	SB: 6.9 NSB:11.5	5.0 1.5	CABISP	Color indices consistent with both ages

Table XXXVI. NGC 3396 Combined Age Estimates (continued)

Knot	Age (Myr)	Confidence[a]	Basis[a]	Notes
Q10	6.4	3.0	ABIS	
P2	10.5	2.0	ADS	Could not deredden so no color indices. Age based on Hα only. Probably a mixed population, but no age estimates to quantify.
P	6.5	5.0	ABISP	
O	6.5	4.5	ABISP	Very weak P Cygni in high noise
N	11.5	3.0	ABISP	Color indices not consistent with age
M	n/a	0.0	P	Could not deredden so no color indices. No age estimates available
NGC 3396	SB: 11.5 NSB: 200	7.0 1.0	UCDSP	Hα, Hβ, Color indices unreliable for continuous starburst so not used

a See Table XXXIV for details

It is interesting to note that there are many more NSB populations in NGC 3396 than in NGC 3395. This may be explained by the orientation of the galaxies. We observed NGC 3395 more or less perpendicular to the plane of the galaxy, while for NGC 3396 the orientation was almost parallel to the plane of the galaxy. Since we are looking more or less in the plane of NGC 3396 the probability of observing multiple populations along the same line of sight is increased in comparison to NGC 3395. The data seem to confirm this hypothesis.

There is no age gradient in the galaxies apparent in our data. For the regions we observed in both galaxies, all the star forming regions for which we have some confidence in our age estimate have roughly the same age of ~ 5 Myr. This implies that starbursts are global phenomena and do not propagate across a galaxy. The data are also consistent with the interpretation that the starburst is not only happening more or less simultaneously within each galaxy, it is also occuring simultaneously in both galaxies. If true, the fact that it is occurring simultaneously in both galaxies gives credence to the interaction being the source of the star formation in line with current theory.

Finally, we find that the age derived for the unresolved knots via the UM technique can be ~ twice the UM age of the subknots that make it up. Similarly the age derived for the unresolved knot for the CM technique can be ~ 2-3 times the CM age of the subknots that make it up. Therefore we speculate that ages derived for unresolved knots are representative of the underlying resolved knot ages to ~ a factor of 2-3. This is of use in high-redshift work where one cannot resolve the individual starburst knots.

CHAPTER 6

CONCLUSIONS

In the preceding work we have defined 31 star forming knots in the interacting

galaxies NGC 3395 and NGC 3396. The knots are possible super star clusters on the

order of ~ 100 pc in diameter and display a wide variety of spectra—some knots have a

very blue spectrum with strong P Cygni wind profiles in the UV, strong Balmer emission

lines, and characteristics of Wolf-Rayet stars while other knots have none of these

features and exhibit a pronounced Balmer decrement with little to no Balmer emission.

We calculated the metallicity for each knot via a variety of emission line, equivalent

width and color index techniques and found that the metallicities range from $Z = 0.1$-1.7

$Z_\odot$ with typical values of 0.5-0.6 $Z_\odot$. We examined the various metallicity estimation

techniques for consistency with each other and found that the emission line methods were

consistent with each other, but the SCK equivalent width and color methods exhibited

large scatter and frequently were not consistent with the other estimates. We found that

we could obtain consistent results by placing reasonable restrictions on the parameter

space over which these techniques were valid. Specifically, we found that in order to

give consistent results one can consider only:

- Si IV method metallicity estimates ≥ 8.0

- C IV method metallicity estimates ≤ 9.0

- C(14-35) method metallicity estimates ≤ 9.0

179

By honoring these limits, results which are consistent with the each other and with the emission line methods can be obtained. No metallicity gradient was found in the subject galaxies. Finally, we compared the metallicites of the spatially resolved knots to the unresolved spectrum of the portion of the galaxies that we observed. We found that the metallicity of the unresolved spectrum was representative of the metallicity of the resolved knots. This has implications at high redshift where, because of the distances involved, it is not possible to resolve separate knots.

We measured the flux in the broad He II $\lambda4686$ emission line characteristic of Wolf-Rayet (WR) stars. We found 5 knots in NGC 3395 and 7 knots in NGC 3396 which exhibited the emission in addition to the unresolved knots. Uncorrected for reddening, we estimated ~ 250 WR stars in NGC 3395 and ~ 400 WR stars in NGC 3396. We related the number of WR stars to the number of O stars using the ratio of He II $\lambda4686$/Hβ and observed ~1100 O stars in NGC 3395 and ~ 2500 O stars in NGC 3396 uncorrected for reddening. We were unable to sub-categorize the WR stars, although the spectra are consistent with WN stars. We found that there are few WR stars in the background regions of the unresolved galaxy spectra outside of our resolved knots, as expected.

During our WR analysis we discovered a super bubble in NGC 3395. The region in question has a radius of approximately 24 pc and contains ~80 WR stars uncorrected for reddening. We calculate that it also contains ~25 O stars although we suspect that we have severely underestimated this value and a more representative value may be as many as 420 O stars uncorrected for reddening.

We attempted to use the Leitherer et al. (1999) Starburst 99 (SB99) spectral synthesis models to determine the best fit model for each knot as a function of IMF, starburst type, and age. We found the SB99 continuum fitting models (CM) have

significant problems simultaneously fitting the UV, visible and far red continua and the Balmer decrement. These problems are severe, and lower our confidence in estimates based on the CM. We found the SB99 UV feature models (UM) fit our data much better but still underestimated the magnitude of absorption and emission in P Cygni profiles in comparison to our data.

The resolved measurement knots' spectra were better fit by instantaneous starburst models and we found that the knots were too small to reasonably be modeled by continuous starbursts for more than 1-2 Myr. We found that the unresolved knots were large enough to support a continuous starburst for ~ 1Gyr and their spectra were best fit as continuous starbursts, even though they are in fact made up of smaller instantaneous starbursting knots and older preexisting populations at different ages.

We considered several SB99 initial mass functions (IMFs) in our age analysis. Based on the presence of WR stars, we eliminated the IMF with an upper mass of 30 $M_\odot$. The CM predicted a slight preference in the data for an IMF with a power law exponent of α=3.30 and an upper mass of 100 $M_\odot$; however the Wolf-Rayet He II λ4686 bump equivalent widths in our resolved knots are frequently too large for the α=3.30 IMF and are more consistent with the α=2.35 IMF. We also found that within a given starburst type (instantaneous or continuous) the ages calculated from models with the different IMFs are very similar. We therefore adopted the α=2.35 IMF for our age analysis.

The ages for our knots were estimated using both the UM and CM models. We found the UV technique gave ages that were the most representative of the hot young population. By avoiding the Balmer decrement region, we were able to calculate fits to the CM as well but we found that these age estimates were older than the UM estimates

and were more sensitive to other older starburst populations or preexisting stellar populations along the same line of sight (if any).

We attempted to use the β_{1550} spectral slope age estimation technique, but we found that it was very sensitive to the exact method used to measure the slope. Due to our limited wavelength coverage, we were unable to measure the spectral slope at 1550 Å in exactly the same way that SB99 did and we were unable to correct for the differences.

We also attempted to use the Hα, Hβ, and He II λ4686 equivalent width age estimation techniques. We found that the Hα and Hβ age estimates were in excellent agreement with each other despite the fact that we were unable to deblend Hα λ6563 and [N II] $\lambda\lambda$6548,6583. We also found that the Hα and Hβ age estimates were vulnerable to being biased older by other older stellar populations colocated or along the same line of sight as the young hot stars generating the Balmer emission. The He II λ4686 equivalent width age was found to be in excellent agreement with the UM age and was very representative of the hot young star population.

Finally, we attempted to use the U-B, B-V, V-I, and V-R color index age estimation techniques. The problems we found with the SB99 continuum nebular emission modeling cause the U-B color index age estimate to be completely unusable. The other color indices are multiple valued and are extremely flat rendering them of limited practical utility other than as a reasonableness check for other estimates.

We combined all of the age estimation techniques and developed our best estimate of the age of each of our measurement knots. We found no age gradient in the galaxies implying the starburst does not propagate across the galaxy but rather occurs simultaneously everywhere. The data are also consistent with the interpretation that the

starburst is not only happening more or less simultaneously within each galaxy, it is also occuring more or less simultaneously in both galaxies. If true, the fact that it is occurring simultaneously in both galaxies gives credence to the interaction being the source of the star formation in line with current theory.

We found the ages we derived for the unresolved knots are representative of the underlying resolved knot ages to within a factor of 2-3. This is of use in high-redshift work where one cannot resolve the individual starburst knots.

APPENDIX

O Star Average Mass Calculation

We calculate the average mass of an O star. The table below has the calculation

using data from Drillling and Landolt (1999). Column (1) is the spectral type; column (2)

is the typical mass of that type; column (3) is the abundance relative to 1 $M_\odot$ where

$N \propto (M/M_\odot)^{-2.35}$; column (4) is M* N; the last row is the sum of the column values.

Table XXXVII. O Star Mass Supporting Calculations

Spectral Type	Mass ($M_\odot$)[a]	N	M * N ($M_\odot$)
O3 V	120	1.30E-05	1.56E-03
O5 V	60	6.63E-05	3.98E-03
O6 V	37	2.06E-04	7.64E-03
O8 V	23	6.31E-04	1.45E-02
Sum	240	9.17E-04	2.77E-02

[a] Mass from Drillling and Landolt (1999)

We form the mass weighted average according to the formula

$$\overline{M}(O) = \frac{\Sigma M_i * N_i}{\Sigma N_i} = \frac{2.77x10^{-2}}{9.17x10^{-4}} = 30.$$

and we obtain the mass weighted average mass of an O star is 30.2 $M_\odot$.

REFERENCES

Arp H., 1966, ApJS, 14, 1

Ashman, K. M.; Zepf, S. E., 1992, ApJ, 384, 50

Bachilla R., 2003, The Journal of Young Investigators (jyi.org)

Balzano V. A., 1983, ApJ, 268, 602

Bransford M. A.; Thilker D. A.; Walterbos R. A. M. and King, N. L. 1999, ApJ 118,
1635

Campbell A.; Terlevich R; Melnick J, 1986, MNRAS, 223, 811

Carpenter E. F., 1957, PASP 69, 386

Calzetti D.; Kinney A. L.; Storchi-Bergmann T., 1994, ApJ 429, 582

Clemens, M. S., Baxter, K. M., Alexander, P, & Green D. A. 1999, MNRAS, 308, 364

Conti P. S.; Leitherer C.; Vacca, W. D., 1996, ApJL 461, 87

Dreyer J. L. E., 1888, MmRAS, 49, 1

Drillling, J. S., and Landolt, A. U., 1999 in Allen's Astrophysical Quantities, Fourth
edition, edited by Arthur N. Cox, published by Springer-Verlag, New York, p.
389.

D'Odorico S., 1970, ApJ, 160, 3

Dopita, M. A. & Evans L. N., 1986 ApJ 307, 431

Edmunds, M. G.; Pagel, B. E. J, 1984, MNRAS, 211, 507

Foellmi, C.; Moffat, A. F.; Guerrero M. A., 2003 MNRAS, 338, 360

185

Goldsmith, P. F., 1987 in Allen's Astrophysical Quantities, Fourth edition, edited by

    Arthur N. Cox, published by Springer-Verlag, New York, p. 51

Hancock et al., 2003, AJ, in press.

Holmberg, E., 1958, Lund Medd. Astron. Obs. Ser. II, 136, 1

Huang Z. P., Yin Q. F., Saslaw W. C., Heeschen P. S., 1994, ApJ 423, 614

Huchra J. P., Geller M. J., Corwin H. G., 1995, ApJS 99, 391

Ibata, R. A.; Gilmore, G.; Irwin, M. J., 1995, MNRAS, 277, 781

Keyes T., 1997, Hubble Space Telescope Data Handbook, 1997, STScI, Baltimore MD

Kennicutt, R. C.; Schweizer F.; Barnes J. E., Galaxies: Interactions and Induced Star
    Formation, 1996, Springer, Berlin

Kewley L. J. & Dopita M. A. 2002 (KD), ApJS, 142, 35

Kinney, A. L., Bohlin, R. C., & Calzetti, D. 1993 ApJS, 86, 5

Kudritzki, R. P., Pauldrach, A., Puls, J., & Abbott, D. C. 1989, A& A, 219, 205

Kunith, D. & Joubert, M. 1985, A&A 142, 411

Kurucz, R. L., 1979a ApJS, 40, 1

Kurucz, R. L., 1979b, in Problems of Calibration of Multicolor Photometric Systems,
    Dudley Obs. Rep. No 14, A.G. Davis Philiped., p 363

Larson, R. B.; Tinsley, B. M., 1978, ApJ, 219, 46

Leitherer, C.; Schaerer, D.; Goldader, J. D.; Delgado, R. M. G.; Robert, C.; Kune, D. F.;
    de Mello, D. F.; Devost, D.; Heckman T. M., 1999 ApJS, 123, 3

Lowenthal, J. D.; Koo, D. C.; Guzman, R.; Gallego, J.; Phillips, A. C.; Faber, S. M.;
    Vogt, N. P.; Illingworth, G. D.; Gronwall, C., 1997 ApJ, 481, 673

NASA/IPAC Extragalactic Database

Mas-Hesse, J. M. & Kunith, D. 1991,A&AS, 88, 399

Maeder, A. 1998, IAU Symp. 189: Fundamental Stellar Properties, 189, 313

McCall, M. L. , 1984, MNRAS, 208, 253

McCall, M. L.; Rybski, P. M.; Shields, G. A., 1985, ApJS, 57, 1

McGaugh S. S., 1991, ApJ, 380, 140

Miller, G. J., & Chu, Y.-H. 1993, ApJS, 85, 137

Nilson, P., Uppsala General Catalog of Galaxies, 1973, Acta Universitatis Upsalienis, Nova Regiae Societatis Upsaliensis, Series V: A, Vol. 1

Osterbrock, D. E. Astrophysics of Gaseous Nebulae, 1974, University Science Books, Sausalito, CA

Osterbrock, D. E. Astrophysics of Gaseous Nebulae and Active Galactic Nuclei, 1989, University Science Books, Sausalito, CA

Pagel B. E. J.; Edmunds M. G.; Blackwell D. E.; Chun, M. S.; Smith, G, 1979 MNRAS, 189, 95

Read A.M., & Ponman T. J., 1998, MNRAS, 297, 143

Rizzo J. R.; Martin-Pintado J., 2001, phso conference, 487

Schaerer, D., Contini, T., & Pindao, M. 1999, A&AS, 136, 35

Scharer, D., & Vacca W. D. 1998 (S&V), ApJ 497, 618

Shields, G. A.; Searle, L., 1978, Ap. J., 222, 821

Soifer B. T., Sanders D. B., Madore B. F., Neugebauer G., Danielson G. E., Elias J. H. Lonsdale C. J., Rice W. L., 1987, ApJ 320, 238

Storchi-Bergmann T.; Calzetti D.; Kinney A. L., 1994, ApJ 429, 572

Strickland D. K.; Stevens I. R., 1999, MNRAS, 306, 43

Vacca, W. D., & Conti, P. S., 1992, Ap. J., 401, 543

van Zee, L.; Salzer, J. J.; Haynes, M. P.; O'Donoghue, A. A.; Balonek, T. J.; AJ, 116,2805

Walsh, J. R.; Baum S. A.; Malamath E. M. & Goudfrooij, P., 1997, STIS ISR 97-16

Zaritsky, D.; Kennicutt, R. C.; Huchra J. R., 1994, Ap. J., 420, 87

Zeilik M., Gregory, S. A. & Smith E. v. P., Introductory Astronomy and Astrophysics, 1992, Harcourt Brace Jovanovich College Publisher, Fort Worth

Zepf, S. E., 1997, Nature, 390, 377

VITA

Graduate College
University of Nevada, Las Vegas

Kenneth Plaks

Home Address:
      488 First Light Street
      Henderson, NV 89052

Degrees:
      Bachelor of Science, Physics, 1989
      United States Air Force Academy

      Bachelor of Science, Mathematics, 1989
      United States Air Force Academy

      Master of Science, Physics, 1991
      Massachusetts Institute of Technology

Dissertation Title: A Spectroscopic Analysis of the Starburst Galaxies NGC 3395 and
NGC 3396

Dissertation Examination Committee:
      Chairperson, Dr. Donna E. Weistrop, Ph. D.
      Committee Member Dr. Lon Spight, Ph. D.
      Committee Member Dr. Stephen Lepp, Ph. D.
      Committee Member Dr. Boyd Earl, Ph. D.